A DEVELOPMENTAL ALGORITHM FOR SYNAPSE-SPECIFIC WIRING OF THE *DROSOPHILA* VISUAL MAP

APPROVED BY SUPERVISORY COMMITTEE

Peter Robin Hiesinger, Ph.D. (Mentor) _____

Jonathan Terman, Ph.D. (Chair) _____

Helmut Krämer, Ph.D. _____

Kimberly Huber, Ph.D. _____

DEDICATION

Dedicated to my mom, dad and sister

For their unconditional love and support

A DEVELOPMENTAL ALGORITHM FOR SYNAPSE-SPECIFIC WIRING OF THE *DROSOPHILA* VISUAL MAP

by

Egemen Agi

DISSERTATION

Presented to the Faculty of the Graduate School of Biomedical Sciences

The University of Texas Southwestern Medical Center at Dallas

In Partial Fulfillment of the Requirements

For the Degree of

DOCTOR OF PHILOSOPHY

The University of Texas Southwestern Medical Center at Dallas

Dallas, Texas

August, 2017

ACKNOWLEDGEMENTS

I would like to thank my mentor Peter Robin Hiesinger for giving me the opportunity to go after an exciting question and providing me with all the tools that helped me in my pursuit. I am especially grateful to him for his infinite patience in trying to make me aim for higher during my studies.

I would also like to thank my past and present thesis committee members, Jonathan Terman, Helmut Kramer, Steven Altschuler, Ege Kavalali and Kimberly Huber for their time and guidance.

I learnt a lot from every single lab mate of mine and I cannot appreciate enough their contribution in my development as a scientist. I'd like to thank Marion Langen for her collaboration; Chih-Chiang Chan and Dong Wang for their mentoring in my early days in the lab; Jennifer Jin, Daniel Epstein, Neset Ozel, Charlotte Wit and others for being there and making it bearable when things were not going well.

I am very lucky to get to know some amazing people in Dallas. I am especially indebted to Kacey Rajkovich, Vural Tagal, Didem Agac, Basar Cenik, Bercin Cenik, Keun Ryu, Carlos Gil del Alcazar and Pavlina Todorova for their unconditional help and support and friendship.

I am blessed to have the love and support of my mom, dad and sister throughout my life. Without them I wouldn't be able to come this far.

Last but not the least, I'd like to thank Anatoli Ender for bringing joy to my life every single second.

A DEVELOPMENTAL ALGORITHM FOR SYNAPSE-SPECIFIC WIRING OF THE *DROSOPHILA* VISUAL MAP

EGEMEN AGI, Ph.D.

The University of Texas Southwestern Medical Center at Dallas, 2017

PETER ROBIN HIESINGER, Ph.D.

During brain development, genetic information and environmental input drive neural circuit assembly that requires matching of correct pre- and post-synaptic partners. In cases when environmental input has no instructive role in synaptic partner selection, genetic information alone must suffice to specify synapses in neural circuits. However, how a limited amount of genetic information is translated into developmental algorithms for synapse specification is unclear. A major thrust of the field has been the quest to identify guidance cues and molecular matchmaking codes underlying brain wiring. In this work, I present a complementary approach, in which the characterization of the developmental algorithm based on simple rules is the primary focus, and the molecules executing these rules secondary. I propose that simple rules

underlying developmental algorithms can be sufficient to establish seemingly complex wiring diagrams without an elaborate matchmaking code between synaptic partners.

I used *Drosophila* visual map, which is a genetically encoded neural circuit, as a model system to test my hypothesis. During visual map formation, around 4800 photoreceptors simultaneously project to their correct target layer 'lamina' in the brain to find their correct synaptic partners. I developed a 2-photon microscopy-based, intravital imaging technique with which I could observe the development of individual photoreceptor growth cones at the spatiotemporal resolution of filopodial dynamics over 24 hours during visual map formation. Based on these imaging data, I spearheaded a group effort to formulate and computationally test simple rules that are sufficient for photoreceptors to sort to their correct partners without a requirement for precise matchmaking codes. A key prediction of the model was that the post-synaptic partners may not act as target cues for the pre-synaptic photoreceptors. In the second part of my thesis, I tested this hypothesis by ablating and blocking membrane dynamics of post-synaptic partners. My findings indicate that indeed post-synaptic partners of photoreceptors do not act as target cues for photoreceptors, but are necessary during a preceding step in the developmental algorithm to ensure correct wiring.

In brief, results I presented in this work support the idea that correct synaptic partner selection can be achieved through a developmental algorithm based on simple rules that sorts correct cells together prior to synapse formation.

TABLE OF CONTENTS

PUBLICATIONS

Langen, M.*, **Agi, E**.*, Altschuler, D.J., Wu, L.F., Altschuler, S.J., and Hiesinger, P.R. (2015). The Developmental Rules of Neural Superposition in Drosophila. Cell *162*, 120-133. * equal contribution.

Agi, E.*, Langen, M.*, Altschuler, S.J., Wu, L.F., Zimmermann, T., and Hiesinger, P.R. (2014). The evolution and development of neural superposition. J Neurogenet *28*, 216-232. * equal contribution.

Cherry, S., Jin, E.J., Ozel, M.N., Lu, Z., **Agi, E.**, Wang, D., Jung, W.H., Epstein, D., Meinertzhagen, I.A., Chan, C.C., *et al.* (2013). Charcot-Marie-Tooth 2B mutations in rab7 cause dosage-dependent neurodegeneration due to partial loss of function. Elife *2*, e01064.

Jin, E.J., Chan, C.C., **Agi, E.**, Cherry, S., Hanacik, E., Buszczak, M., and Hiesinger, P.R. (2012). Similarities of Drosophila rab GTPases based on expression profiling: completion and analysis of the rab-Gal4 kit. PLoS One *7*, e40912.

LIST OF FIGURES

CHAPTER ONE FIGURES

CHAPTER TWO FIGURES

CHAPTER TWO SUPPLEMENTAL FIGURES

CHAPTER THREE FIGURES

CHAPTER THREE SUPPLEMENTAL FIGURES

CHAPTER FOUR FIGURES

LIST OF DEFINITIONS

R1-6 - Photoreceptor subtypes 1 to 6

R7-8 – Photoreceptor subtypes 7 and 8

hAPF – Hours after puparium formation

L-cells – Lamina monopolar cells

L1-5 – Lamina monopolar cell subtypes 1 to 5

PTP69D – Protein tyrosine phosphatase 69D

CadN, NCad – N-Cadherin

P +20% - 20% of pupal development

UAS – Upstream activation sequence

Jeb – Jelly Belly

alk – anaplastic lymphoma kinase

shi – shibire

shi^{ts} – Temperature sensitive shibire

HS – Heat shock

PBS – Phosphate-buffered saline

HL3 – hemolymph-like saline

CHAPTER ONE

Introduction

Acknowledgement

Parts of this chapter, including figures, were published in my following work:

Agi, E.*, Langen, M.*, Altschuler, S.J., Wu, L.F., Zimmermann, T., and Hiesinger, P.R. (2014). The evolution and development of neural superposition. J Neurogenet *28*, 216-232. * equal contribution

1.1 RATIONALE AND OVERVIEW

Neural circuit architecture is determined by genetic information and environmental input, such as sensory-driven neural activity (Penn and Shatz, 1999). There are examples where neural circuits are assembled before the animal has any sensory experience (Hiesinger et al., 2006), suggesting that in some cases environment does not have an instructive role for circuit assembly. In hard-wired circuits synapses are specified only by genetic information alone (Hassan and Hiesinger, 2015; Hiesinger et al., 2006). How a limited amount of genetic information is translated into specification of a functioning neural circuit is an intriguing problem. In 1940, Roger Sperry formulated the chemoaffinity theory to answer this problem (Meyer, 1998; Sperry, 1963). The idea that molecules can function as attractive and repulsive cues and direct axon pathfinding by determining axon targets has been hugely influential. Over many years, the idea

has developed to include the concept of a molecular code: any given set of distinct attractive or repulsive molecular cues may define where exactly a specific axon will target and form synaptic connection. Indeed, many guidance cues and cell adhesion molecules have been characterized throughout the years and have been proposed to function as molecular codes for synaptic partner selection (Kolodkin and Tessier-Lavigne, 2011). Although molecular matchmaking codes seem to provide an answer to the problem of specificity, they only do so by introducing another question as difficult as the previous: how are the molecular matchmaking codes are expressed at the right time at the right place specifically between partners? Furthermore, many recent studies showed target independent wiring mechanisms in both vertebrates and invertebrates which suggest that at least some level of specificity can be achieved without matchmaking codes (Petrovic and Schmucker, 2015). But how?

Biological structures are encoded by developmental algorithms where output of one process is the input of the succeeding one. For example, during neural circuit assembly, correct partners should be brought together before they start forming synapses with each other. This sorting step greatly facilitates synaptic partner selection as it limits the possible partner choices: if the right partners are already together, a very simple rule such as cell type recognition is enough to achieve synaptic partner specificity without needing an elaborate matchmaking code. This kind of rule makes sense only if the right partners are brought together in the preceding step. This idea is conceptually similar to a simple synapse formation rule where neurons make exuberant number of synapses with many other neurons without a precise matchmaking code and prune the wrong contacts and sculpt the circuit only later, often in an activity-dependent manner.

In both cases, synapse formation may occur rather promiscuously and specificity is introduced through pre-sorting or post-pruning (Kolodkin and Hiesinger, 2017). I posit that, in a genetically encoded system, pre-sorting of correct partners before synapse formation can ensure specificity without a precise matchmaking code. How can pre-sorting of right partners achieved?

In this work, I presented results that support the idea that pre-sorting of partners can be achieved through simple developmental pattern formation rules. I used *Drosophila* visual map formation as my model since it is a genetically hard-wired circuit. My approach was to observe the temporal succession of developmental events in live and determine the constraints that each step imposed on the next. Based on these, in collaboration with mathematicians, I defined the developmental rules of the underlying developmental algorithm for visual map formation in *Drosophila*.

1.2 CONNECTING THE *DROSOPHILA* EYE TO THE BRAIN: NEURAL SUPERPOSITION AND THE VISUAL MAP

Both the camera eye of vertebrates and the compound eye of insects capture a picture of the outside world. The spatial organization of this picture is mapped through axonal projections from the eye into optic ganglia in the brain, a concept called retinotopy. Retinotopic axonal projections thereby map neighboring points in the picture of the world to neighboring synaptic units in the brain. Both vertebrates and insects form such synaptic visual maps of the world in the brain (Figure 1.1A–D). Neural superposition is a particular case of visual mapping (Braitenberg,

1967; Kirschfeld, 1967; Vigier, 1907a, b, 1909) found in the visual systems of some insects of the order Diptera, which includes *Drosophila Melanogaster* (Hennig, 1973).

The architectures of insect visual systems can be categorized into three types: apposition, optic superposition, and neural superposition (Braitenberg, 1967; Greiner, 2006; Kirschfeld, 1967; Land and Nilsson, 2002; Land, 2005; Shaw, 1969) (Figure 1B–D). In all three architectures, the light-sensing elements are the rhabdomeres (marked blue in Figure 1.1B–D), morphological specializations of the photoreceptor neurons (retinula cells) under the lens (facet) of a single unit eye (ommatidium) of the compound eye. Most insects have apposition or optic superposition eyes and a basic understanding of these types is needed to appreciate neural superposition. Both apposition and optic superposition eyes have a so-called fused rhabdom, i.e., the rhabdomeres of the contributing retinula cells are in direct contact with each other and function as a single, central light guide under the lens. Hence, all retinula cells in an ommatidium with a fused rhabdom receive input from the same field of view (Figure 1.1B, C).

The size of the rhabdom and the lens aperture together define the retinula cell's acceptor angle and field of view (dotted lines in Figure 1.2). The apposition eye maximizes its spatial resolution when the acceptor angle matches the angle between the individual ommatidia, because then the field of view of each ommatidium directly abuts (apposes) the field of view of the neighboring ommatidium (black dotted lines in Figure 1.2). The ommatidia in most diurnal (active during daylight) insects have a small fused rhabdom and a small lens aperture because they do not need high sensitivity and profit from a high spatial resolution. In contrast,

optical superposition eyes exhibit an increase of the lens aperture and/or the rhabdom size that leads to overlapping (superimposed) fields of view and a loss in spatial resolution (green dotted lines in Figure 1.2). Optic superposition increases sensitivity at the cost of spatial resolution and is an adaptation to nocturnal life and dim light conditions (Land and Nilsson, 2002; Land, 2005; Warrant, 1999). In both apposition and optic superposition eyes, retinula cells form fused rhabdoms and their axons project as a bundle into the brain where they make connections in the same synaptic unit (Figure 1.1B, C) (Meinertzhagen, 1976). These synaptic units are called cartridges (Cajal and Sánchez, 1915). The apposition and optical superposition eyes are classic examples of retinotopy and simple axonal wiring diagrams.

In neural superposition eyes, simple retinotopy of ommatidial axon bundles is replaced by a more complicated wiring diagram that combines individual axon terminals in the brain from retinula cells with the same visual axis in the eye (Figure 1.1D). Remarkably, neural superposition preserves the high resolution of an apposition eye with the same optics, but significantly increases sensitivity (Braitenberg, 1967; Kirschfeld, 1967; Vigier, 1908). How is that possible? A key to an understanding of neural superposition lies in the optics of the apposition eye (Figure 1.2). As described above, the size of a fused rhabdom in an apposition eye with optimal spatial resolution is limited to a small area that ensures an ommatidial field of view that has little or no overlap with the fields of view of neighboring ommatidia (central black disc/rhabdom in Figure 1.2). The small rhabdom size limits photon catch and thus sensitivity. For a given eye size an increase in the rhabdom diameter increases sensitivity at the cost of spatial resolution (green disc/rhabdom in Figure 1.2). Neural superposition eyes with the same

small aperture utilize this additional space marked by the green disc in Figure 1.2 to increase their sensitivity. To avoid a loss of spatial resolution, the neural superposition eye separates different areas within the area marked by the green disc with separate rhabdomeres (Figure 1.3A). Separated rhabdomeres are also referred to as an open rhabdom and partially or fully open rhabdoms are found in all true flies (Diptera) (Dietrich, 1909; Osorio, 2007; Tuurala, 1963) (Figure 1.1D; Figure 1.3A, C). Since each of the separated rhabdomeres receive input via a different visual axis (a different point in the environment), neural superposition requires a dramatic rewiring of all axons carrying input from the same visual axis from different ommatidia into the same lamina cartridge (Figure 1.3C).

The most common neural superposition eye is found in all advanced flies (suborder *Brachycera*; includes *Drosophila melanogaster*). Here, retinula cells R1–R6 contribute larger, outer rhabdomeres, while R7 and R8 reside in the center and are stacked on top of each other (i.e., they see the same point in space). Since the outer and inner retinula cell rhabdomeres are arranged underneath a single lens, they receive light from seven different points in space (Figure 1.4). In *Drosophila*, R1–R6 are the primary motion detectors, whereas R7 and R8 may contribute to motion detection, but primarily transmit color information into the brain (Gao et al., 2008; Morante and Desplan, 2004; Wardill et al., 2012; Yamaguchi et al., 2008). Hence, R1–R6 axons form a primary visual map.

The first fascinating aspect of the neural superposition eye is the crystalline precision with which facets and rhabdomeres are arranged to ensure proper function. In the *Drosophila* type of neural superposition, the angle between the visual axes of neighboring R1–R6

rhabdomeres is closely matched by the angle between the facets (Braitenberg, 1967; Kirschfeld, 1967; Kirschfeld and Franceschini, 1968). Consequently, if an R1 photoreceptor sees a point “A” in the environment, there must be an R2 in exactly one neighboring ommatidium that sees the same point “A” in the environment (Figures 1.1D and 1.4A). In total, there is exactly one R1, R2, R3, R4, R5, and R6 (in six different ommatidia) that sees the same point in space. In all advanced flies R1–R6 are arranged in a trapezoidal pattern (Figure 1.4A). The summation of independent, parallel input channels with the same visual axis significantly increases sensitivity for the signal from that field of view as described above. Because the number of visual axes as well as the number of cartridges (i.e., pixels of the visual map) are the same in a neural superposition eye and apposition eye of the same size, it seems the interpretation that neural superposition increases resolution (Moses, 2006) is less likely to be the case. Instead, the increased sensitivity afforded by neural superposition is considered to be advantageous under low light conditions (Land and Nilsson, 2002) and provides additional parallel input for efficient visual processing of the day-active, fast-flying flies.

How does the precision of the angular arrangement of light-sensitive elements and single eyes in the neural superposition eye translate to the wiring in the brain? Notably, already Vigier and Cajal (Cajal and Sánchez, 1915; Vigier, 1907b) observed that the axons from one ommatidium participate in the formation of different optical cartridges. As in the case of the apposition eye, the photoreceptor neurons residing in the same ommatidium form a bundle of their axons that together projects to the brain. In contrast to the apposition eye, these bundles consist of eight input lines that receive input via seven different visual axes (Figure

1.4B). In order for neural superposition to work, the bundle needs to untangle in such a way that precisely those R1–R6 axons from six different ommatidia that receive input through the same visual axis converge upon the same synaptic cartridge (while R7 and R8 project straight through the lamina into a deeper brain area, medulla) (Figure 1.4A). In the case of the well-studied genetic model organism *Drosophila melanogaster*, this means that R1–R6 axons from approximately 800 ommatidia (Ready et al., 1976) must unscramble the eye's input by engaging in an enigmatic sorting process that forms a functional visual map. How this sorting process occurs developmentally is the second, and maybe most fascinating aspect of neural superposition. This wiring principle is not strictly retinotopic, since axons from different ommatidia intermingle to innervate synaptic cartridges that represent neighboring points in the visual environment. However, at the level of the visual map, it is beautifully simple: from the perspective of the postsynaptic neurons that receive input from R1–R6 that see the same point "A", it does not matter how the complicated optics and wiring are developmentally resolved. This then is the challenge and the source of the fascination with neural superposition: how is such a complicated wiring pattern developmentally realized?

1.3 THE DEVELOPMENT OF NEURAL SUPERPOSITION

The fly eye has served for decades as a powerful model for the study of cell specification, organ development, and pattern formation (Baker, 2007; Carthew, 2007; Chan et al., 2011; Roignant and Treisman, 2009; Tsachaki and Sprecher, 2012; Wolff and Ready, 1993; Wolff and

Ready, 1991). Here, I will focus on the basic principles that set the stage for neural superposition wiring as it is found in *Drosophila melanogaster*.

1.3.1 Axon Pathfinding from the Eye to the Lamina

The morphogenesis of the developing eye disc orchestrates the initial timing of axonal connections between the eye and lamina. Retinula cells differentiate and pattern the fly eye in a temporal wave. A morphogenetic furrow sweeps across the developing eye disc during larval stages, patterning the hexagonal array of the compound eye in its wake. The photoreceptor neuron R8 differentiates first, followed sequentially by the pairs R2/R5, R3/R4, R1/R6, and eventually R7. The differentiation process of all cells from the posterior to the anterior margin takes around 2 days (Roignant and Treisman, 2009; Tomlinson and Ready, 1987; Wolff and Ready, 1991).

Retinula cells send out axonal processes shortly after differentiation beginning with R8 and followed by all other subtypes (Tomlinson and Ready, 1987). The axons are subsequently ensheathed by glia cells that divide the axons in ommatidial bundles (Meinertzhagen and Hanson, 1993). Each retinula cell axon bundle twists 180° between the retina and lamina plexus such that the axon terminals are 180° degrees rotated relative to their arrangement when leaving the ommatidium. This bundle rotation is very precise and clockwise for the right eye from the dorsal retina, counterclockwise from the ventral retina, and vice versa for the left eye (Braitenberg, 1967; Meinertzhagen and Hanson, 1993; Trujillo-Cenoz and Melamed, 1966). The axons terminate between two layers of glia cells where their growth cones form the lamina

plexus (Clandinin and Zipursky, 2002; Fischbach and Hiesinger, 2008; Poeck et al., 2001). The lamina plexus will give rise to the lamina neuropil, where R1–R6 establish the visual map through synaptic connections with lamina neurons (Cajal, 1909; Vigier, 1908). R7 and R8 axons project through the lamina into the deeper medulla neuropil, where they terminate in the layers that in the adult will become M6 and M3, respectively (Fischbach and Dittrich, 1989).

Several molecules have been identified that are required for the correct targeting of R1–R6 in the lamina and R7/R8 in the medulla. For example, the ubiquitin-specific protease Nonstop is required for the development of the glial cells that provide the initial R1– R6 target (Martin et al., 1995; Poeck et al., 2001). On R1–R6 growth cones, the receptor tyrosine phosphatase PTP69D is required for correct targeting (Garrity et al., 1999). The nuclear protein Brakeless functions in all retinula cells and represses the function of the transcription factor Runt in R2 and R5. Interestingly, loss of this repression in only these two retinula cells is sufficient to mistarget all R1–R6 to the medulla (Edwards and Meinertzhagen, 2009; Kaminker et al., 2002; Rao et al., 2000; Senti et al., 2000; Tayler and Garrity, 2003). Together, these studies reveal a hierarchical dependence of retinula cell–glia and retinula cell–retinula cell interactions that determine the initial axon targeting to the lamina.

Rows of retinula cell axons arrive sequentially in the optic lobe, in the wake of the developmental wave of retinula cell differentiation in the eye disc. The axon bundles thereby establish a grid that represents a prerequisite for subsequent visual map formation. It is not entirely clear how each row of retinula cell bundles defasciculates from the optic stalk in an evenly spaced manner to form a precisely patterned rhomboidal grid (Figure 1.4). It might be

thought that this grid is established by the photoreceptors themselves and not the lamina neurons, since the arriving bundles induce the initiation of differentiation of lamina neurons through the secretion of Hedgehog (Huang and Kunes, 1996). However, it has been shown that if lamina neurons cannot differentiate and interact with photoreceptors at this early stage of visual map formation, lamina area innervated by photoreceptors drastically shrinks (Sugie et al., 2010; Umetsu et al., 2006) suggesting that lamina cells also play a role in this grid formation. In addition, glia plays a critical role in the targeting of the bundles and probably in the establishment of the grid (Hadjieconomou et al., 2011). In the lamina plexus, R1–R6 axons defasciculate and extend into lamina cartridges where they find their synaptic partners, the lamina neurons (Figure 1.5). The rhomboidal grid is a prerequisite for this sorting process of R1–R6 growth cones to establish neural superposition (Chapter 2&3).

1.3.2 R1-R6 Growth Cone Sorting in the Lamina Plexus

The arrival of ommatidial axon bundles in the lamina plexus marks the end of photoreceptor target finding in the case of the apposition eye. In contrast, in the neural superposition eye, the most important and least understood developmental process is about to begin: How do thousands of R1–R6 growth cones leave their origination bundle to identify new targets in other cartridges, thereby exchanging growth cones with neighboring cartridges? This enigmatic shuffling process has fascinated scientists for decades (Clandinin and Zipursky, 2000;

Fischbach and Hiesinger, 2008; Hiesinger et al., 2006; Horridge and Meinertzhagen, 1970; Meinertzhagen and Hanson, 1993; Trujillo-Cenoz and Melamed, 1973).

As described above, rows of axons arrive in a temporal wave in the lamina plexus throughout larval development and into the first day of pupal development. However, it is unclear how long the developmental wave persists in the lamina plexus. Cross-sectional images of growth cones in the lamina plexus after 20% of pupal development (P + 20% or P20: from puparium formation to adulthood, it takes around 100 hours at 25°C) reveal no morphological differences between growth cones from axons that arrived earlier or later during development (Hiesinger et al., 2006; Schwabe et al., 2013). Based on this observation, it has been argued that the growth cone sorting process that establishes neural superposition in the lamina plexus occurs synchronously for all retinula cells (Schwabe et.al., 2013, also Chapter 2 of this study). This important notion implies a break of the asymmetry of the temporal wave after axon arrival and a transition to synchronous morphogenesis of the growth cone sorting process. The precise time point or mechanism of this asymmetry break has not been determined and it is unclear whether it applies equally to all photoreceptors and lamina neurons involved in the establishment of neural superposition.

R1–R6 growth cone shapes have first been described for different developmental stages using transmission electron microscopy (Meinertzhagen and Hanson, 1993). According to ultrastructural analyses, only few morphological changes are apparent between P + 12.5% and P + 24.5%. Between P + 25% and P + 32% filopodial extensions become more pronounced and especially R3 elongates rather suddenly in the direction of its distinct trajectory. At P + 50%

distinct cartridges are apparent in the ultrastructure (Meinertzhagen and Hanson, 1993). A more recent analysis of R1–R6 growth cone shapes at distinct time points in fixed preparations by Schwabe et.al. (2013) revealed a clear, subtype-specific polarization of the growth cones starting at P + 20%. According to this study, growth cones first polarize and subsequently begin to extend to their targets around P + 32%.

Mutant analyses in *Drosophila* have provided key insights into the establishment of neural superposition. Clandinin and Zipursky (2000) showed that the bundle rotation predetermines the growth cone trajectories, as evidenced by the following analyses of mutant phenotypes. In the *frizzled* mutant, individual ommatidia are rotated by 180°. Remarkably, this ommatidial rotation results in a perfect 180° rotation of the trapezoidal projection trajectories of R1–R6. This important experiment revealed that the projection direction is autonomously encoded by the orientation of the bundle, i.e., not determined by other growth cones in the lamina plexus. In contrast, in *nemo* mutants, in which ommatidia are rotated up to 45°, no corresponding angular change of R1–R6 growth cone trajectories was observed (Clandinin and Zipursky, 2000). This experiment suggests that the target grid in the lamina plexus places constraints on the orientation of the trapezoidal R1–R6 growth cone trajectories; it may allow a full 180° flip, but no partial rotations. Further mutational analyses in the same study revealed a dependency of R1, R2, R5, and R6 targeting on R3 and R4, whereas R3 and R4 themselves target independently of R1 and R6. In contrast, R2 and R5 targeting seemed to be affected by loss of R1 and R6 (Clandinin and Zipursky, 2000). These findings suggest a hierarchical pattern formation process, the rules of which remain unresolved.

Since these seminal studies, numerous mutants, predominantly affecting cell adhesion molecules, have been identified that are required for R1–R6 sorting in the lamina plexus, including N-Cadherin (Lee et al., 2001), D-Lar (Clandinin et al., 2001; Maurel-Zaffran et al., 2001), the protocadherin Flamingo (Lee et al., 2003; Senti et al., 2003), among numerous others (Hadjieconomou et al., 2011; Mast et al., 2006; Ting and Lee, 2007). Of these, arguably the most informative studies for the understanding of the development of neural superposition come from studies by Clandinin and colleagues on the protocadherin Flamingo. Individual R1–R6 cells that lack Flamingo exhibit surprisingly normal targeting behavior if they are surrounded by wild type cells. In contrast, wild type growth cones neighboring the *flamingo* mutant growth cones exhibit specific mistargeting defects (Chen and Clandinin, 2008). These findings indicate that the precise trajectory of growth cone polarization and targeting is nonautonomously determined by the neighboring growth cones in the origination bundle. This idea was recently developed further to include the concept of a network of differential adhesion through differential levels of Flamingo both within the same growth cone as well as between ommatidial bundles (Schwabe et al., 2013).

Mutant analyses of several other cell adhesion molecules reveal partially penetrant phenotypes for several steps of the developmental program (Figure 5). These include a cell-autonomous role for Dlar, Liprin-alpha, and N-Cadherin in R1–R6 targeting (Clandinin et al., 2001; Maurel-Zaffran et al., 2001; Prakash et al., 2005; Prakash et al., 2009). None of these studies suggested a molecular code for target matching, while they are consistent with an iterative pattern formation process (Chan et al., 2011). Similarly, initially it has been shown

that N-cadherin function in R7 is required for correct target layer selection in the medulla (Lee et al., 2001; Ting et al., 2005). However, ex-vivo live imaging of R7 dynamics showed that R7s that are devoid of N-Cadherin are still able to project to their correct target layer but cannot adhere so retract back which had been interpreted as targeting defects (Ozel et al., 2015). This result further suggests that N-Cadherin is not a molecular code for target matching. The precise role of interactions between R1–R6 growth cones and postsynaptic lamina neurons is unknown. At least one secreted protein, the anaplastic lymphome kinase (alk) ligand Jelly Belly (Jeb), has been characterized that anterogradely signals to lamina neurons and is required for R1–R6 targeting (Bazigou et al., 2007). However, in a later study it was shown that Jeb/alk signaling is required for survival of one of the lamina cells, L3, and R cell mistargeting is due to the loss of L3s (Pecot et al., 2014). In brief, how these different molecular signaling events interplay to set up the dynamic interplay of R1–R6 growth cone sorting remains unclear.

1.3.3 R1-R6 Growth Cone Sorting Predetermines Synaptic Columns and Partners

At P + 40% R1–R6 growth cones have established contact with their target cartridges (Meinertzhagen and Hanson, 1993; Schwabe et al., 2013). While the entire preceding sorting process occurred in a two-dimensional array, R1–R6 growth cones now commence a “dive in” process that creates tubular columns perpendicular to the lamina plexus. During this column formation process, each R1–R6 growth cone in the correct target cartridge elongates through the proximal glia cell layer toward the center of the brain. The final R1–R6 terminals exhibit

a column length of ~25 mm. The fate of the original lamina plexus, which remains distal to the expanding columns in the lamina, has received comparably little attention and its adult function, if any, is unknown.

In the final arrangement, R1–R6 form a more or less circular arrangement of R1–R6 in the periphery of the cartridge while the main postsynaptic lamina neurons L1 and L2 reside in the cartridge center (Figure 1.5). R1–R6 are organized in stereotypic rotational sequence R1-2-3-4-5-6 as determined in 1970 through the precise reconstruction of hundreds of retinula cell axons in *Calliphora* (Horridge and Meinertzhagen, 1970). Similarly, perfect stereotypy was revealed through dye labeling of all retinula cells in an ommatidium of the house fly Musca domestica (Picaud et al., 1990). In addition, the apparent stereotypic arrangement of L3 between R5 and R6 in the lamina column further supports a stereotypic arrangement of all cartridge elements (Meinertzhagen and O'Neil, 1991; Rivera-Alba et al., 2011). Since the R1–R6 in a cartridge represent input from the same field of view, it is not entirely clear whether such stereotypy has a functional significance.

The stereotypic arrangement of six terminals per cartridge is altered at the equator that separates the axonal projections from the dorsal and ventral half of the eye. On each side of the equator reside two rows of cartridges with eight terminals and one with seven terminals per cartridge (Braitenberg, 1967; Horridge and Meinertzhagen, 1970). It has therefore been argued that the equator is a region of increased sensitivity (Hardie, 1985). R1–R6 terminals in equatorial cartridges with 7 or 8 terminals per cartridge are also arranged in a stereotypic rotational organization with a characteristic complement of terminals (Horridge and

Meinertzhagen, 1970). Interestingly, Horridge and Meinertzhagen (1970a) also found that within a population of 650 R1–R6 axon terminals, not a single one projected to the wrong cartridge. In contrast, 10 of these 650 exhibited misplacements in the rotational organization within the correct cartridge, most of which occurred around the equator. Further analyses of more than 500 R1–R6 axon terminals around the equator in another single *Calliphora* specimen revealed an increased error rate specifically at places where the equator is not a straight line (Meinertzhagen, 1972). Based on these seminal studies, Meinertzhagen (1972) concluded that these errors reveal simple rules for the sorting of R1–R6 in cartridges that are not consistent with a rigid specification of terminal location.

The columnar cartridge organization has recently been described in terms of a quantitative model for "wiring economy" (Rivera-Alba et al., 2011). The placement of neurons in a lamina cartridge can be explained by minimizing lengths of connections between neurons and preventing them from taking the same physical space (volume exclusion) through optimization of a cost function that takes into consideration wiring economy and volume exclusion. Rivera-Alba et al. (2011) argue that R1–R6 should occupy the periphery of the cartridge to minimize obstruction of other neuronal connections due to their larger diameter. Since R1–R6 terminals form more synapses with L1 and L2 than any other cells, the wiring economy model offers a plausible explanation why L1 and L2 are in the center of the cartridge.

L1 and L2 extend numerous filopodia that intercalate between the R1–R6 columns and initiate synapse formation (Meinertzhagen and Hanson, 1993; Meinertzhagen et al., 2000) (Figure 1.5). Synapse formation is characterized by the appearance of presynaptic densities, so-

called “T-bars,” which become apparent in the ultrastructure only after P + 50% (Meinertzhagen and Hanson, 1993). In the adult visual map, each R1–R6 columnar terminal forms approximately 50 synapses (Meinertzhagen and Hu, 1996; Meinertzhagen and Sorra, 2001). R1–R6 form so-called tetrad synapses in which each presynaptic site is opposed by four postsynaptic spines. The assembly sequence of these tetrad synapses follows a distinct sequence and always includes at least one L1 and one L2 (Meinertzhagen and Hu, 1996; Meinertzhagen and O'Neil, 1991; Meinertzhagen et al., 2000). The synapses obey a spacing rule that ensures that in wild type each synaptic contact site is on average at least 1 μm apart from any other synapse (Meinertzhagen and Hu, 1996). Other postsynaptic cell types include amacrine cells and lamina widefield neurons, but their role in the development of neural superposition is unclear.

The assembly sequence of R1–R6 tetrad synapses is invariable and precise with respect to the cell types involved (Meinertzhagen et al., 2000). However, mutant analyses have revealed that the synapse formation program is blind with respect to whether the preceding growth cone sorting is correct or faulty (Hiesinger et al., 2006). Specifically, individual R1–R6 terminals in adult cartridges that formed after incorrect growth cone sorting still form on average the correct number of synapses. Since L1 and L2 initiate synapse formation through the extension of filopodial contact with R1–R6 it is conceivable that either the lamina neurons or the photoreceptors determine this precise number of synapses. This question has been addressed through the analysis of miswired cartridges. Such cartridges in different mutants may contain as few as one or more than ten retinula cell terminals. The precise number of synapses per retinula cell terminal is independent of such flawed cartridge compositions (Hiesinger et al., 2006).

Synapse number per R1–R6 terminal has also been analyzed in cartridges of systematically different composition in the wild type (Frohlich and Meinertzhagen, 1987). Together, these findings support the idea that synapse formation is a genetically separable developmental program that is based on cell types present in cartridges, but blind toward the earlier growth cone sorting process and with respect to the retinula cell number or subtypes in a cartridge. The same study also showed that this synapse formation program is unaffected by the loss of electrical or synaptic activity. Hence, the primary *Drosophila* visual map is an example for a genetically "hard-wired" brain region and neural circuit (Hiesinger et al., 2006), even though individual synaptic structures undergo plastic changes, e.g., in response to light (Rybak and Meinertzhagen, 1997).

1.3.4 Steps of the development of neural superposition

Extensive anatomical and genetic studies on the development of neural superposition have revealed a series of genetically separable steps (Figure 1.5): 1) axon pathfinding from the eye to the lamina occurs in a temporal wave until P + 20%, 2) growth cone sorting occurs laterally, perpendicular to the original axon bundles, in the lamina plexus layer between P + 20% and P + 40%, 3) retinula cell growth cones elongate proximally to form columns, and lamina neurons initiate synaptic partner selection after P + 35%, 4) synapses form between P + 55% and eclosion.

Of these four steps, numbers (1) and (2) are genetically separated in mutants of guidance receptors/cell adhesion molecules (e.g., *flamingo*). Similarly, steps (2) and (4) are genetically separated by numerous mutants; to my knowledge, all neural superposition mutants analyzed to date ultrastructurally still have tetrad synapses. These findings give rise to the idea that the seemingly complicated developmental program underlying the synapse-specific wiring of neural superposition is encoded by the concatenation of much simpler genetically encoded developmental subprograms (Chan et al., 2011; Hiesinger et al., 2006). Of these subprograms, step (2), the lateral sorting of growth cones in the lamina, predetermines synaptic partners.

1.4 2-PHOTON INTRAVITAL IMAGING OF *DROSOPHILA* VISUAL MAP FORMATION

Intra-vital imaging is a powerful tool to visualize developmental processes in their native environments with the least possible amount of, if any, perturbations (Pittet and Weissleder, 2011). Due to absence of any invasiveness, the need for optimization of culture conditions is minimal and the effect of a dying organism is non-existent. With conventional confocal microscopes intravital imaging of developmental processes that are close to the surface of the organism is possible (Cordero et al., 2007; Ninov et al., 2007; Ninov and Martin-Blanco, 2007). However, the main challenge for intravital imaging is the accessibility of deeper tissues of interest. 2-photon microscopy provides a way that allows for deep tissue visualization.

In 2-photon microscopy fluorophores are excited by two low energy photons with near IR (infrared) wavelength simultaneously (Weigert et al., 2013). Longer wavelengths allow

penetration of excitation light with lower diffraction which in turn allows deep tissue excitation (Svoboda and Yasuda, 2006). Since a fluorophore should be hit by 2 photons at the same time, this results in excitation in a specific focal plane without any out of focus excitation. Therefore, 2-photon microscopy causes less photobleaching and phototoxicity than conventional confocal microscopes (Pittet and Weissleder, 2011; Svoboda and Yasuda, 2006; Weigert et al., 2013).

Effective utilization of 2-photon microscopy for intra-vital imaging requires tissue accessibility (Pittet and Weissleder, 2011). To image development in mouse brain, either the skull should be thinned or a cranial window should be opened (Grutzendler et al., 2002; Holtmaat et al., 2009). In *Drosophila*, to record calcium signals in neurons that are in optomotor response pathway, a window is opened on top of the head of an adult fly for accessibility (Seelig et al., 2010). However, intravital imaging of *Drosophila* photoreceptor sorting does not require any invasive procedures since the eye tissue is very transparent during visual map formation. By just putting a cover slip on top of the eye (explained in detail in Materials and Methods Chapter) photoreceptors can be visualized for extended time periods. However, after P50, eyes start to get pigmented (Wolff and Ready, 1993) and this decreases the accessibility of photoreceptor growth cones. Therefore, pigmentation imposes an upper limit for the time span of live imaging.

Finally, photoreceptor targeting occurs during pupal stages of development when the animal is immobile and there are no muscle contractions. Therefore, no anesthesia or physical immobilization is required as in other systems (Pittet and Weissleder, 2011).

1.5 CHAPTER ONE FIGURES

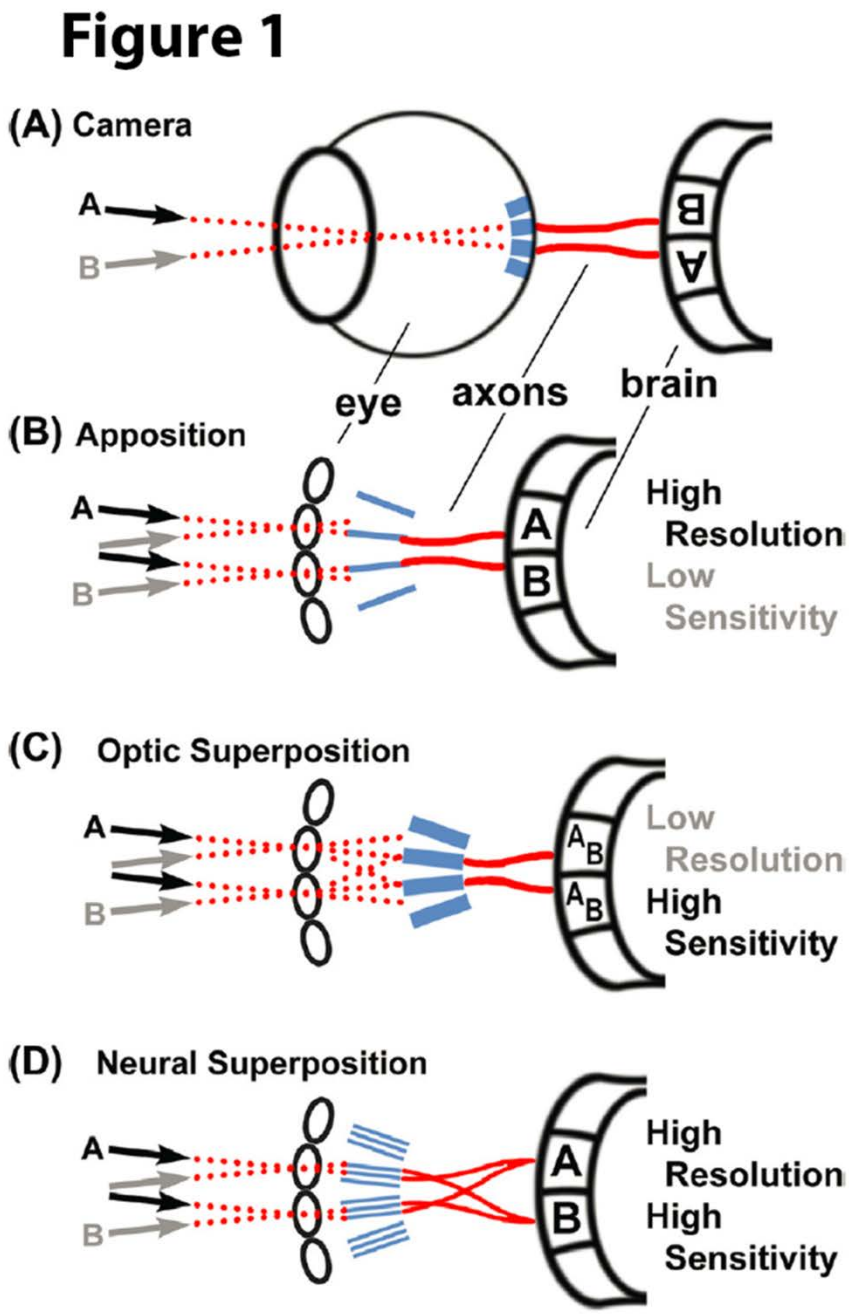

Figure 1.1. Comparison of visual systems

All light-sensitive elements (retina or rhabdoms) are shown in blue, light paths are shown as dotted red lines, and axonal connections between the eye and the brain are shown as solid red lines. (A) The camera eye of vertebrates produces an inverted image on the light-sensitive elements that is transmitted to the brain via optic nerves. (B) The apposition eye is the most common diurnal insect eye and produces an upright image on the light-sensitive rhabdoms as well as in the first optic neuropil, the lamina. Note that each individual ommatidium of the compound eye technically produces an inverted image on the rhabdom underneath that lens; however, the rhabdom is a single "fused" light guide for several retinula cells and only contributes a single pixel to the final image that is not further resolved. Apposition eyes are typically optimized for high resolution by "apposing" little overlapping visual fields of neighboring ommatidia based on small apertures and rhabdoms. (C) Optic superposition eyes comprise the reflectory and refractory superposition types. Input from several ommatidia is optically superimposed on individual rhabdoms, which increases sensitivity at the expense of resolution, typically in nocturnal insects, e.g., moths. (D) Neural superposition retains the high resolution of the apposition eye while increasing sensitivity by combining a number of input channels. This is achieved by separating the light sensitive elements (rhabdomeres) in the rhabdom and precise axonal wiring, as described in detail in Figures 2–4.

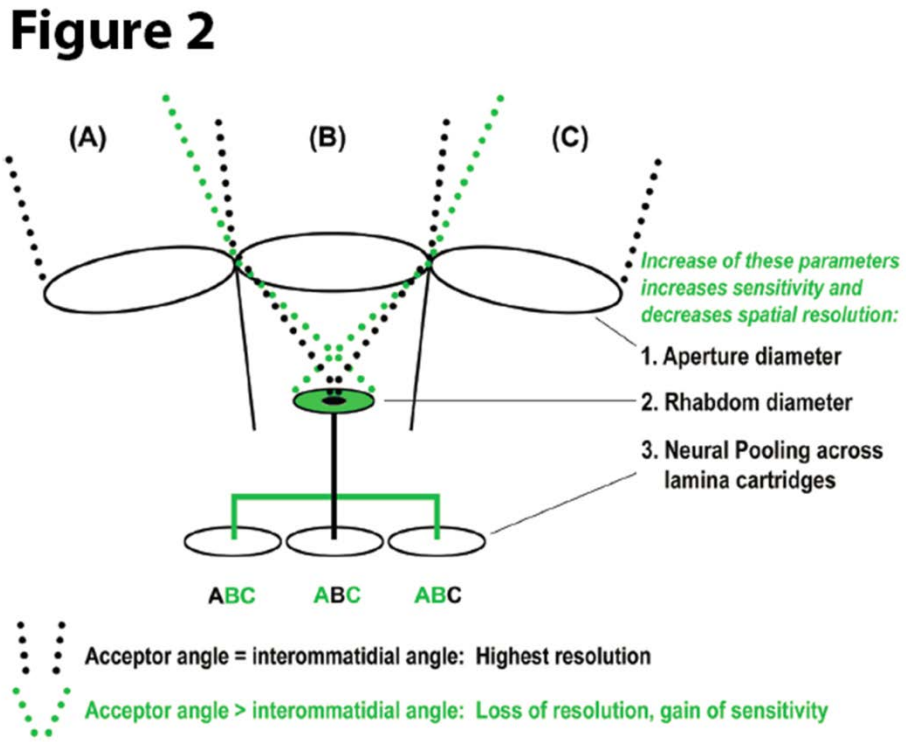

Figure 1. 2. Limits of the ancestral apposition optics reveal the improvement potential for neural superposition.

In an idealized, ancestral apposition eye each ommatidium sees a field of view (A, B, C) that directly abuts/apposes the field of view of its neighboring ommatidia. The aperture that defines this field of view only allows for a small maximum size of the light-sensitive rhabdom (small black disc). An increase of the rhabdom diameter (green disc) causes overlapping, instead of apposing, fields of view (dotted green light paths), which increases sensitivity at the expense of resolution. In the idealized (and indeed typical) apposition eye, little or no overlap between neighboring fields of view is preserved by connecting each rhabdom separately to an individual cartridge in the lamina (black line) with neighboring rhabdoms connected to neighboring cartridges. Sensitivity can be increased at the expense of resolution by distributing the input channel from a single rhabdom to surrounding cartridges (green line), in which case each cartridge receives input from several fields of view (green A,B,C). Both neural pooling and increased rhabdom size occur in nocturnal insects with typical diurnal apposition eyes. Note that for a given increase in neural pooling, a corresponding increase in rhabdom size will further increase sensitivity without loss of resolution.

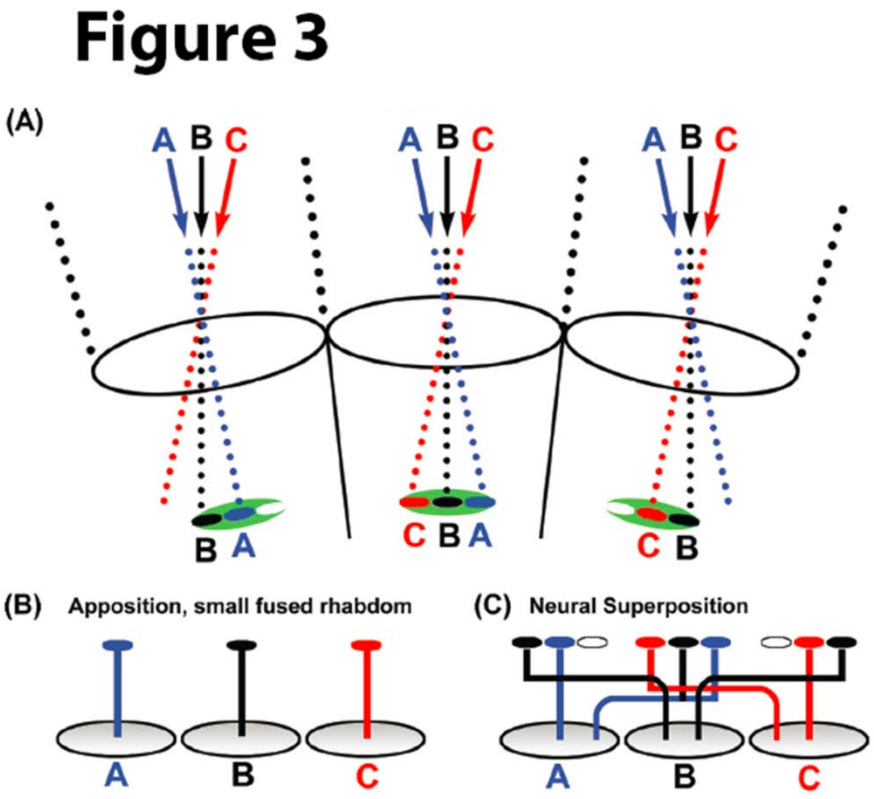

Figure 1.3. Separating rhabdomeres is a strategy to avoid loss of spatial resolution.

(A) Principle optics for differently sized open and fused rhabdoms. Note that these optics are based on an ideal apposition eye (as shown in Figure 2) in which the central disc represents the maximal sized rhabdom (blue for A, black for B, and red for C). The green disc denotes an enlarged (fused) rhabdom area that leads to increased sensitivity and a loss of resolution, as shown in Figure 2. The green disc also marks the area in which separate rhabdomeres in an open rhabdom are positioned (small red, black and blue discs). (B–G) Different wiring diagrams underneath the optics shown in (A). (B) In an idealized apposition eye, small fused rhabdoms receive input from fields of view with little or no overlap (small blue, black, and red discs) and this information is mapped via single retinula cell axon bundles to neighboring cartridges in the lamina. This type of apposition eye is considered ancestral (Nilsson, 1989) and most commonly found in diurnal insects. (C) Neural superposition is based on an open rhabdom in which separate rhabdomeres utilizes additional space around the small rhabdom of an equivalent apposition eye (red, black, and blue discs) and are wired according to their input without loss of resolution.

Figure 4

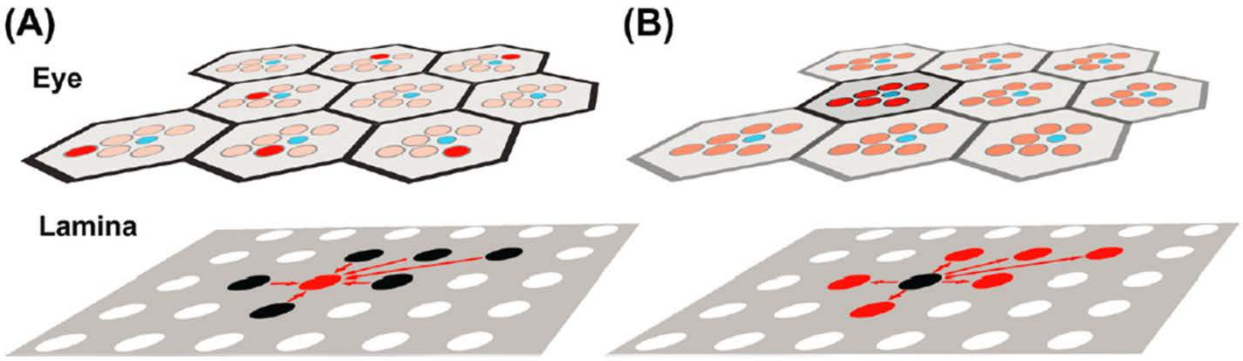

Figure 1.4. Mapping of light-sensing rhabdomeres in the eye onto lamina cartridges in the first optic neuropil, the lamina, in neural superposition of advanced flies (Brachycera).

(A) A single R1 in one ommatidium "sees" the same point in the environment as a single R2 in a neighboring ommatidium, a single R3 in a different neighboring ommatidium, etc. (marked in red in the eye). The six R1–R6 rhabdomeres that have the same visual field converge upon the same cartridge in the lamina (red dot). (B) R1–R6 in a single ommatidium see six different points in space through the separate rhabdomeres (red) and a seventh point through the central, stacked R7/R8 rhabdomeres (blue). The six R1–R6 input lines from a single ommatidium are separated into six separate cartridges in the lamina (red dots).

Figure 5

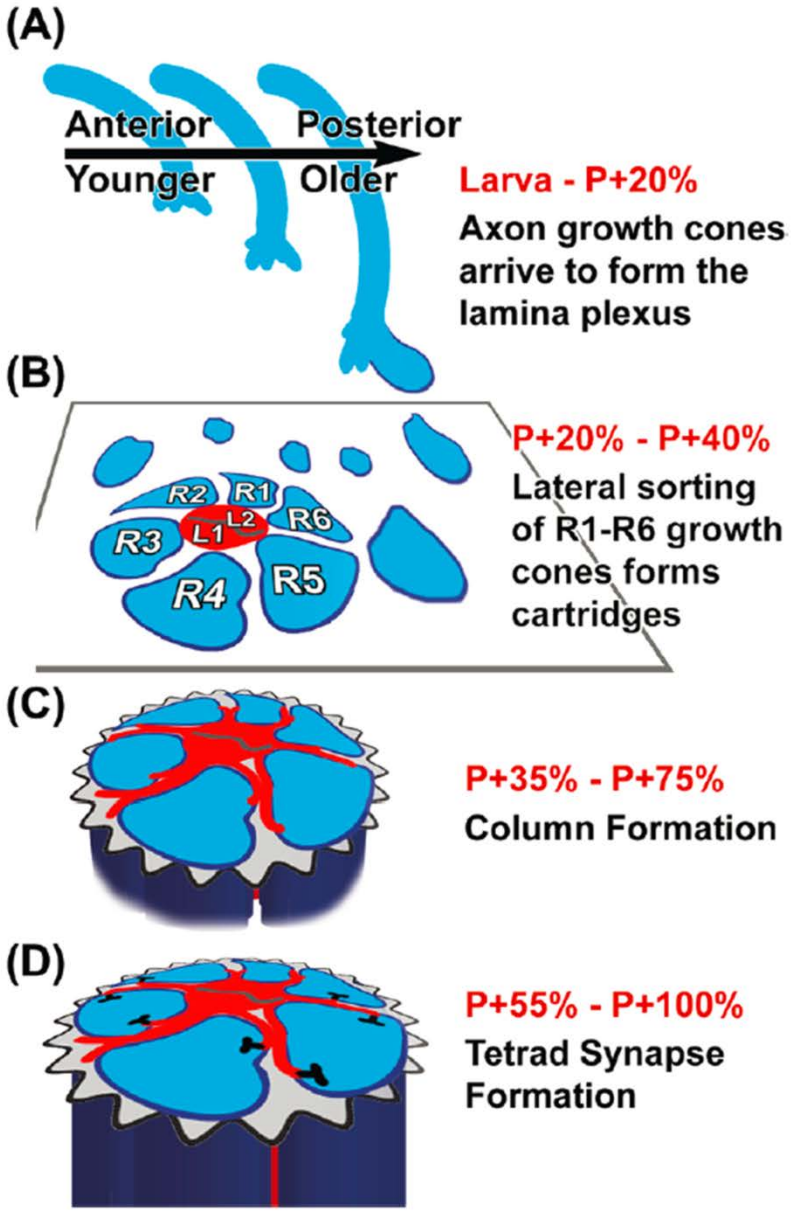
(A)
Anterior
Posterior
Younger
Older
Larva - P+20%
Axon growth cones arrive to form the lamina plexus
(B)
R2
R1
L2
L1
R6
R3
R4
R5
P+20% - P+40%
Lateral sorting of R1-R6 growth cones forms cartridges
(C)
P+35% - P+75%
Column Formation
(D)
P+55% - P+100%
Tetrad Synapse Formation

Figure 1.5. *Development of neural superposition axon projection pattern as observed in Drosophila*

(A) Retinula cell axons arrive in the optic lobe during a temporal wave in the wake of photoreceptor differentiation in the developing eye disc (Tomlinson & Ready, 1987; Wolff & Ready, 1991, 1993). The intermediate target for retinula axons are two layers of glial cells in the optic lobe. (B) The arrival of retinula axon bundles is followed by a lateral growth cone sorting process. The growth cones form a new layer perpendicular to the axons, between the layers of glia cells, called the lamina plexus. Sorting the correct R1–R6 growth cones with the same field of view from six different ommatidia predetermines synaptic partners (Clandinin & Zipursky, 2002; Hiesinger et al., 2006). (C) After growth cone sorting into cartridges that receive input from the same field of view, each retinula terminal elongates proximally for up to 30 mm (Meinertzhagen & Hanson, 1993). (D) Lastly, synapses form between the postsynaptic lamina monopolar cells (red) and the presynaptic retinula cell columns (blue), obeying a minimal spacing rule (Meinertzhagen & Hu, 1996).

CHAPTER TWO

The Developmental Rules of Neural Superposition in *Drosophila*

Acknowledgement

This chapter was previously published in my following work:

Langen, M.*, Agi, E.*, Altschuler, D.J., Wu, L.F., Altschuler, S.J., and Hiesinger, P.R. (2015). The Developmental Rules of Neural Superposition in *Drosophila*. Cell *162*, 120-133. *equal contribution

2.1 ABSTRACT

Complicated neuronal circuits can be genetically encoded, but the underlying developmental algorithms remain largely unknown. Here, we describe a developmental algorithm for the specification of synaptic partner cells through axonal sorting in the Drosophila visual map. Our approach combines intravital imaging of growth cone dynamics in developing brains of intact pupae and data-driven computational modeling. These analyses suggest that three simple rules are sufficient to generate the seemingly complex neural superposition wiring of the fly visual map without an elaborate molecular matchmaking code. Our computational model explains robust and precise wiring in a crowded brain region despite extensive growth cone overlaps and provides a framework for matching molecular

mechanisms with the rules they execute. Finally, ordered geometric axon terminal arrangements that are not required for neural superposition are a side product of the developmental algorithm, thus elucidating neural circuit connectivity that remained unexplained based on adult structure and function alone.

2.2 INTRODUCTION

A central question in neuroscience is how neural circuits selforganize into functional structures during development. The wiring of compound eyes to the brain of flies provides a fascinating model system for studying this question (Agi et al., 2014; Meinertzhagen, 1976; Nilsson, 1989). In particular, the neural superposition eye, such as found in advanced flies, is characterized by a complicated wiring diagram (Figure 2.1): each point in visual space is captured by multiple photoreceptors from different ommatidia that converge upon the same synaptic unit (cartridge) in the brain (Figure 2.1B); different photoreceptors within the same ommatidium view different points in visual space and project to neighboring cartridges (Figure 2.1A) (Braitenberg, 1967; Clandinin and Zipursky, 2002; Kirschfeld, 1967; Vigier, 1907a, b). The correct pooling of axon terminals viewing the same point in space into asingle cartridge increases sensitivity without loss of spatial resolution compared with simpler, ancestral eye types (Agi et al., 2014; Braitenberg, 1967; Kirschfeld, 1967; Nilsson, 1989). The developmental process underlying neural superposition is remarkable, because each individual axon, among thousands of neighboring axons in the brain, must be sorted together with those few axons that receive input from the same point in visual space.

A classic model of neural superposition is found in the Drosophila compound eye, which contains ~800 ommatidia. Each ommatidium projects a bundle of eight photoreceptor (retinula or R-cell) axons into the brain. Six of these photoreceptors, R1–R6 (the focus of our current study) form the primary visual map in the lamina (first optic neuropil) of the fly brain (Figure

2.1A; R1–R6 are color-coded consistently throughout the paper: R1, blue; R2, green; R3, red; R4, yellow; R5, magenta; and R6, orange). The R1–R6 axons from one bundle that receive input from six different points in visual space are denoted A–F (Figures 2.1A–1C).

After neural superposition is established, the R-cells have a precise organization of the six subtypes around the circumference of cartridges, that is, R1 neighbors R2, which neighbors R3, etc., referred to as ‘‘rotational stereotypy’’ (Figures 2.1B and 2.1C). The precision of rotational stereotypy is noteworthy, as the six axon terminals in a cartridge carry the same input information and synapse with the same postsynaptic target cells (Braitenberg, 1967; Trujillo-Cenóz, 1965). Hence, rotational stereotypy is not a functional requirement for neural superposition and increases the demands placed on the sorting problem from 800 cartridges to 4,800 (800 3 6 R1–R6) precise terminal positions. The role, development, and evolutionary origin of this wiring precision are unknown.

The neural superposition wiring diagram has a ‘‘canonical’’ pattern of six R-cell axon terminals per cartridge. An equator from anterior to posterior divides the compound eye, as well as the wiring pattern in the lamina, into dorsal and ventral halves. The wiring patterns in each half of the lamina are opposite to one another with respect to the equator axis (blue line in Figure 2.1C). As a consequence, six rows of ‘‘non-canonical’’ cartridges exist at the equator that contain stereotypic compositions of seven or eight R1–R6 cell axon terminals (Figure 2.1C) (Horridge and Meinertzhagen, 1970; Meinertzhagen and Hanson, 1993). The three different types of equator cartridges also exhibit rotational stereotypy, each with a distinct pattern (Figure 2.1C). As in the case of canonical cartridges, the function of the rotational stereotypic

arrangement of photoreceptor terminals within the equator cartridges is unknown (Horridge and Meinertzhagen, 1970). It is unclear which common developmental rules or mechanisms might robustly encode the canonical cartridges, as well as the three types of equator cartridges (Figure 2.1C).

The Drosophila visual system is an example of a genetically encoded neural circuit in which a developmental sorting step precedes and ensures synaptic specificity between input neurons and their targets (Hiesinger et al., 2006). Many aspects of the developmental sorting step have been characterized in detail, including the formation of an initial grid by lamina cells (Hadjieconomou et al., 2011; Meinertzhagen and Hanson, 1993). Previous studies have suggested the possibility of simple developmental rules underlying this sorting process (Clandinin and Zipursky, 2000; Meinertzhagen and Hanson, 1993; Meinertzhagen, 1972). Furthermore, work in recent years has revealed molecular mechanistic insight into how differential adhesion of guidance receptors may play a key role in growth cone sorting (Chen and Clandinin, 2008; Schwabe et al., 2013). However, no rule set or algorithm has been formulated that is sufficient to generate precise neural superposition in canonical cartridges and equator cartridges. Two key challenges have been (1) the inability to monitor the dynamic sorting process live in developing flies and (2) lack of quantitative, data-driven models to conceptualize or test our understanding of this apparently complicated process.

Here, we report live imaging of R1–R6 growth cone dynamics in intact developing pupa and the derivation of a model that summarizes our conceptual understanding of the development of neural superposition. We propose that three simple rules are sufficient to provide a solution to

the neural superposition sorting problem. Systematic tests of these rules in a computational model reveal that the same rule set leads to precise superposition and the three types of cartridges observed at the equator.

2.3 RESULTS

2.3.1 Intravital Imaging Reveals the Morphogenesis of the Lamina during Brain Development

In order to visualize the growth cone movements that establish neural superposition, we made use of multi-photon time-lapse microscopy to image through the eye of intact developing pupae (intravital imaging; Figure 2.2A). This approach allowed us to visualize both large-scale tissue movements and small-scale growth cone dynamics in the developing pupa. Importantly, our method is non-invasive, and only data from pupae that completed development normally were used throughout this study.

The lamina plexus is a temporary structure in which R1–R6 growth cones sort in a 2D, dynamically warping plane (Meinertzhagen and Hanson, 1993). Labeling of all photoreceptors with a membrane-tagged CD4-tdGFP (Han et al., 2011) throughout the time period of neural superposition development from 20–40 hr after puparium formation (APF) allowed the visualization of R1–R6 projections that form the lamina plexus in relation to the deeper projections of R7/8 axons (Figures 2.2A–D).

Our intravital imaging technique enabled us to identify two major large-scale tissue movements that were, to our knowledge, previously uncharacterized (Figures 2.2B–G; Movie S1). First, we observed a 90° rotation of the entire lamina-medulla complex (Figures 2.2B–D). Second, the lamina plexus flattens in a temporal wave of shortening axons underneath the eye

(Figures 2.2E–G). The 20–40 hr temporal wave alters the orientation of the lamina from a plane close to perpendicular to one that is parallel with both the eye and the medulla (Figures 2.2E–G; red arrows in Figure 2.2F). Hence, the relative change of angles between the lamina plexus and medulla, known as ‘‘medulla rotation,’’ (Meinertzhagen and Hanson, 1993; White and Kankel, 1978) is the result of the progressive intercalation of the lamina plexus between the eye and medulla. This developmental process ensures a perfect alignment of eye and lamina with minimal axon length for the transmission of graded potentials. Our understanding of lamina plexus movements allowed us to distinguish individual growth cone dynamics from movements of the tissue in which they are embedded.

To visualize individual growth cones in the lamina plexus, we utilized a sparse labeling technique (Rintelen et al., 2001). At 40 hr APF, all randomly labeled growth cones fall into one of six distinct classes based on their three dimensional morphology and orientation. Tracing axons back to their unique cell-body positions in the eye unequivocally identified each as an R1–R6 subtype (color-coded as in Figure 2.1) (Figures 2.2H–J). Next, we followed each growth cone through all time points back to 25 hr APF (Figures 2.2K and 2.2L; Movie S2). As the warped plane of the lamina plexus unfolds, different parts change their position relative to the fixed light path during intravital imaging. We therefore corrected clusters of 2–12 growth cones for these tissue movements (Experimental Procedures). The resulting data provide complete 4D dynamics of identified R1–R6 growth cones throughout the process of superposition sorting in a 2D plane.

2.3.2 The Scaffolding Rule: Bipolar Growth Cone ‘‘Heels’’ Generate a Stable Framework for the Sorting Process

During the establishment of neural superposition, 6 x 800 (4,800) growth cones leave their origination bundles and terminate in surrounding destination cartridges (Figure 2.1A). This sorting of axons predicts the repositioning of neighboring growth cones relative to each other. Such rearrangements of individual growth cones were inferred from previous studies on fixed preparations at timed stages (Meinertzhagen and Hanson, 1993; Trujillo-Cenoz and Melamed, 1973) and should be readily apparent in our intravital imaging data.

Surprisingly, we did not observe the expected rearrangements of growth cones between 25–40 hr APF, despite the emergence of polarized, extended growth cone shapes. Four out of the six subtypes develop distinct bipolar growth cone shapes that were not previously described in fixed preparations. After 30 hr APF, we observed distinct ‘‘heel’’ structures anchored at the original arrival points of the axons (arrowheads in Figures 2.3A–F) and distinct ‘‘front’’ densities in the direction of polar extension for R1, R3, R4, and R6 (arrows in Figures 2.3D–F). A time-lapse movie of the growth cone heels revealed no rearrangements of their relative positions (Figures 2.3A’–F’; Movie S3). In contrast, the growth cone fronts progressively move away from their respective heels with subtype-specific speeds and angles. Distinct filopodial movements are clearly visible at both the heels (arrowheads) and fronts (arrows) (Figures 2.3A–F). Importantly, bipolarity gives the two active ends of each growth cone—the stationary heel and the extending front—the potential to execute different functions during growth cone sorting.

Fortuitously, our imaging data revealed a background grid-like pattern (Figure 2.3G). None of the identified growth cone heels, but all fronts, overlap with this background pattern. Hence, the visible pattern in the live-imaging data of sparsely labeled growth cones coincides with the growth cone fronts in the target area, while all growth cone heels are positioned around these regions. Based on these data, we extrapolated the positions of heels and fronts for all R-cells (Figure 2.3H). The heels occupy about half of the space in the 2D grid and provide a complementary pattern to the growth cone fronts (Figure 2.3H; Figure S1). The heel and target grid frame the starting and ending positions of growth cone sorting in 2D (Figure 2.3J).

2.3.3 The Extension Rule: Quantitative Analysis of Growth Cone Dynamics Reveals Synchronized Extension Programs Specific for Each R1–R6 Subtype

Next, we analyzed the dynamics of growth cone extension between 25 and 40 hr APF. For each time point, and for each of the 58 growth cones, we measured the position of the (1) heel (solid circle), (2) front (open circle), (3) tip of the longest filopodium extending away from the heel (small solid circle), and (4) tip of the longest filopodium extending away from the front (small open circle) (Figure 2.4A; Movie S5). Heel-front separation became apparent at distinct time points for different R1–R6 subtypes (asterisks in Figure 2.4B). The distances between fronts and heels increase steadily during subtype-specific 5–10 hr time windows (black lines in Figure 2.4B; see also Figures 2.4G–I for traces of individual cells): R3 and R4 extend for more than 10 hr from 25 hr APF onward; R1 and R6 extend between 30 and 37 hr APF; and R2 and R5 show

minimal extension between 30 and 35 hr APF. Thus, polarized growth of a directed collateral, as previously speculated (Trujillo-Cenoz and Melamed, 1973), is not supported from our observations.

All six growth cone subtypes additionally exhibit angular constancy over the entire time period of their extension (Figure 2.4C). Next, we analyzed the angles between heels and the tips of the longest front filopodia, which are unequivocal and objective points for each growth cone and time point. The average of the longest front filopodia for all growth cones of one subtype revealed the same angular constancy and the same angles over time as those determined by manual front identification (compare Figures 2.4C and 2.4D). We noted that filopodia at the heel and front revealed different dynamics with characteristic filopodial exploration angles (Figures 2.4E and 2.4F) and subtypespecific lengths of exploration (Figure S2.2). In contrast to the polarized front filopodia (Figure 2.4E), all R1–R6 heel filopodia randomly explored angles around and away from the direction of polarity (Figure 2.4F). This observation further supports the notion of different functions of growth cone heels and fronts.

As shown above (Figures 2.2B–G), the entire lamina plexus undergoes a progressive alignment in an anterior-to-posterior temporal wave of shortening axons that occurs between 20–40 hr APF; this is concurrent with growth cone sorting in the lamina plexus. We sought to determine whether growth cone dynamics follow this temporal wave by analyzing growth cones in different positions along the anterior to posterior axis (i.e., in different parts of the unfolding 2D array and consequently for axon bundles of different ages). We found that growth cones of the same subtypes at different positions along the anterior-to-posterior axis exhibit no significant

differences, neither in their start time nor in their extension behavior (Figures 2.4G–I). These measurements are consistent with previous observations in fixed preparations that suggested growth cones of distinct subtypes exhibit no morphological gradient (Hiesinger et al., 2006; Schwabe et al., 2013). We conclude that the tissue movements of the lamina between 20–40 hr APF are unlikely to play an instructive role in the synchronous sorting of growth cones.

A previous study on fixed preparations proposed that the development of polarity as early as 20 hr APF precedes and predicts the direction of a separate extension phase after 32 hr APF (Schwabe et al., 2013). However, our live imaging did not reveal separate polarization and extension phases at least for time points after 25 hr APF, but rather showed one continuous extension process. The angles and speeds specific to each R1–R6 subtype ensure that all R-cell growth cone fronts ‘‘meet’’ in the correct target areas for neural superposition as defined by the corresponding heel scaffold. A key aspect of this ‘‘extension rule’’ is that all growth cones of each of the six R-cell subtypes exhibit identical extension behavior across the entire lamina, including the equator region (see below).

2.3.4 The Stop Rule, Part 1: Growth Cone Fronts Overlap with Multiple Targets in the Scaffold

How does growth cone extension stop? We systematically considered extension stop rules ranging from stop rules that require no interactions with surrounding cells to stop rules that integrate multiple intercellular interactions. We envision that ‘‘no interaction’’ stop rules would be either (1) ‘‘programmed’’ into cell-autonomous extension or (2) triggered by an exogenous

stop signal that functions synchronously across the entire lamina plexus. In both cases, the targeting accuracy depends fully on the precision of the scaffold and the extension angles. Our imaging data show that the scaffold within the unfolding lamina exhibits minor warped or bent areas (Figure S2.1) and that the measured extension angles have SDs of around 10° (Figure 2.4C). A lack of feedback from the target area for either of the ‘‘no interaction’’ stop rules would thereby lead to inaccuracies in arrival points of growth cone fronts. This would likely lead to high error rates for wiring and especially rotational stereotypy, which has not been observed (see discussion in section Validation at the Equator). We therefore consider ‘‘no interaction’’ stop rules unlikely, though they remain a theoretical possibility. In the following, we focus on interaction-based stop rules but return to a test of both types of rules in the last section.

Arguably, the simplest interaction based stop rule would be the recognition of a target cell. Can a target cell be robustly recognized among incorrect alternatives in the densely packed lamina plexus? The lamina neurons (L-cells) are R1–R6’s prospective synaptic targets and are also the main cells in the putative target region (Figure S2.1). Throughout the establishment of neural superposition, the L-cells are positioned in the correct target areas and surrounded by R heels (Figures 2.5A and S2.1). However, the extent and arrangement of L-cell processes between 20–35 hr APF also pose a potential problem for L-cells in providing restricted target cues. At 28 hr APF, L-cell processes form a filopodial mesh that covers most of the lamina plexus (Figure 2.5A). This network of L-cell processes overlaps to a large extent with the R1–R6 growth cones. For example, R3 growth cones overlap to different degrees with three to six L-cell clusters in

potential target areas. Importantly, the closest target areas to the R3 growth cones are incorrect (Figure 2.5B, black asterisks).

To quantitatively analyze the conditions under which L-cells could serve as targets, we developed a computational model. The scaffolding rule was implemented using the measured heel grid (Figure 2.3J). The extension rule was implemented using synchronous movements of R front sensing areas (Figure 2.4). We defined the distance between centers of adjacent target areas as D = 1 (5.5 mm; Figures 2.5C and S2.3). However, the shape and area of R-cell growth cone fronts that sense potential targets could not be easily determined from the biological data. Instead, we approximated sensing regions of R-cell fronts as discs. Our data suggest a range of sensing radii (SR) between 0.22 and 0.5: an area defined by SR = 0.22 is contained in >90% of the imaged R front areas; SR = 0.36 is contained in 60%–90% of R front areas; and SR = 0.5 (a circle with a full cartridge diameter) is contained in >30% of imaged R front areas.

If minimal overlap of an R-cell front with a single target region is sufficient to stop growth cone extension, even a relatively small sensing radius would lead to incorrect targeting (black arrow in Figure 2.5D). However, R3 fronts experience partial overlap in passing with even relatively small incorrect targets (Figures 2.5D–F, gray circles with SR = 0.22). (This would also be true for an elliptic R-cell front shape—either centered on or extended ahead of the growth cone front—that has a much larger SR in the direction of polarity; see blue shapes at 30 and 35 hr time points in Figure 2.5D). Partial overlap is apparent in the case of a single representative growth cone over time (Figure 2.5E) and especially for outlines of all imaged R3 growth cones (Figure 2.5F). This observation suggests that partial overlap must be

permissible to avoid stopping the R3 fronts prematurely. Therefore, in our model we allowed R fronts to ignore partial overlaps with targets, up to the distance SR, during extension. For example, the partial overlaps highlighted by the black arrow in Figures 2.5D, 2.5G, and 2.5J are not sufficient to arrest R3 growth cone extension, because the distance between the overlapping circumferences is less than SR = 0.22. Hence, the model allowed us to systematically explore stop rules based on varying R-cell front sizes and overlaps with targets.

We first simulated the extension of R-cell growth cone fronts away from the heels in the scaffold with measured angles (see the Supplemental Experimental Procedures). Our simulation shows that correct sorting is possible for R-cell fronts and target sensing areas as small as SR = 0.22. The total overlap with any target for each R-cell front with SR = 0.22 (moving at measured angles) reveals overlap of R3 with an incorrect target (arrows in Figures 2.5D and 2.5G), although the overlap is below threshold for stopping. Note that our defined threshold covers a variety of alternative sensing possibilities. For example, a given sensing radius with SR/2 overlap is equivalent to half that sensing radius when sensing ‘‘on touch’’ (Figure 2.5L). For an R3 front with SR = 0.36 this overlap reaches SR and causes an early, incorrect stop (arrowhead in Figure 2.5H); R fronts with SR = 0.5 exhibit so much target overlap with surrounding targets that none of them move far (Figure 2.5I).

Finally, we tested whether possible measurement inaccuracies caused this lack of robustness by simulating targeting with ideal (mathematically computed) angles from heel to target regions (Figures 2.5D, 2.5J, and 2.5K). Remarkably, the ideal model yielded almost

identical results to measured data, including a failure to establish neural superposition wiring with growth cone front SRs of 0.36 and above (arrowhead in Figure 2.5K).

Our analyses of a ‘‘target only’’ stop rule indicate that L-cells— or any other cue at the target area—can function as a stop signal only within substantial constraints. Specifically, our model shows that the premature arrest of growth cone extension can be averted only if R-cell fronts use a sensing area that is either insensitive to or much smaller than the apparent morphological area covered by the growth cone front and its filopodia when it passes the incorrect targets.

2.3.5 The Stop Rule, Part 2: Overlaps between R1–R6 Growth Cone Fronts Can Increase the Robustness of the Stop Rule

In addition to overlaps of R1–R6 fronts with multiple target areas, overlaps among the R1–R6 fronts themselves in the correct target region are already apparent around 25 hr APF (Figures 2.6A–C). This overlap increases substantially until 35 hr APF (Figures 2.6D–F). At the end of growth cone sorting, each R1–R6 front covers ~50% or more of its target area, which is shared with the five other growth cone fronts needed to establish correct neural superposition (Figure 2.6G; arrow shows overlap of all six ‘‘incoming’’ R-cell fronts needed to establish the correct pattern of sorting). We therefore incorporated increasing overlaps between R1–R6 fronts into the model.

We first simulated a ‘‘combinatorial overlap + target’’ stop rule, in which an R-cell growth cone front stops only if it encounters a target area plus five other R-cell fronts (defined by overlap of a given SR). In order to allow the R-cell fronts to move out of their originating bundles, the stop rule was required to begin shortly after extension starts (Experimental Procedures). A simulation with SR = 0.36, which failed using the ‘‘target only’’ stop rule (Figures 2.5D and 2.5H), reveals correct establishment of neural superposition wiring in the model (Figure 2.6H, top row) (Movie S6 shows a ‘‘combinatorial overlap’’ simulation without requiring a target, which behaves identically to the ‘‘combinatorial overlap + target’’ stop rule, see below). Remarkably, even an extraordinarily large sensing area, with a diameter of the entire inter-cartridge distance (using SR = 0.5), can correctly establish neural superposition (Movie S6; Figure 2.6H bottom row). This is surprising because larger sensing radii have a higher chance to cause a premature stop due to overlap. However, R fronts exhibit a collective, sharp increase of total area overlap with other R fronts and target areas only once they reach the correct target area (Figure 2.6I).

Next, we systematically compared the precision of wiring for ‘‘combinatorial overlap + target’’ stop rules for different numbers k (k = 0 to 5) of other R-cell fronts. We additionally performed this test while scanning SR from 0.2 to 0.5. Our results show that all combinatorial stop rules for overlap with $k \geq 3$ other R-cells perform more robustly with larger sensing areas than the ‘‘target only’’ (k = 0) rule (Figure 2.6J). Stop rules that combine target recognition with the sensing of 4 or 5 other R-cell fronts function robustly over the wide range of scanned sensing radii. Hence, these findings suggest that R fronts of large sizes and substantial overlap can target

correctly if the target is defined by coincidence detection of the target plus other R-cell fronts, independent of their subtype.

Surprisingly, a ‘‘combinatorial overlap’’ stop rule, based on R-cell front sensing when the target area itself does not contribute to the combinatorial stop rule, functions robustly (Movie S6). Specifically, recognition of $k \geq 4$ other R-cell fronts without the target area itself is nearly as robust as when the target area is included (Figure 2.6J). This finding reveals the theoretical possibility that target recognition during growth cone sorting may be an intrinsic property of the R-cell growth cone array and does not require the recognition of the actual target itself (e.g., L-cells) as part of the stop rule. In addition, our results show that even in an unconstrained model in which all R-cells sense all other R-cells, the geometry of the scaffold ensures that only the ‘‘right’’ R-cell fronts stop each other in the right place (Movie S6).

Next, we quantitatively assessed the robustness of the ‘‘target only’’ and ‘‘combinatorial overlap’’ models with respect to perturbations in extension angle. We computed the probability of accurate neural superposition patterning in the case when the extension direction of each R1–R6 subtype was randomly varied up to ±10° around its idealized direction (Figure S2.4; n = 100 simulations per condition). We created phase plane diagrams of accuracy as a function of the sensing radii of R-cell fronts, sensing start time and stop rules (Figures 2.6K–M). The simulations of the ‘‘target only’’ model reveal that correct neural superposition wiring is only robust for small sensing radii (SR < 0.35) if the overlap is sensed throughout sorting (sensing start time earlier than 30 hr APF; Figure 2.6K). However, larger sensing radii can function robustly in the ‘‘target only’’ model only if overlap sensing is turned on at 35 hr APF or later,

i.e., at the very end of extension, after R-cell fronts have already passed incorrect targets. Such a late overlap sensing start would be facilitated by the synchronous nature of growth cone sorting. However, the ‘‘target only’’ model lacks robustness for sensing radii that match the morphological appearance of the imaged R fronts (Figures 2.5D–F, 2.6A–G, and S2.4A) and overlap sensing prior to 32 hr APF. In contrast, ‘‘combinatorial overlap’’ stop rules based on R-cell front sensing (with or without the target) exhibit robustness for larger sensing radii that have extensive R-cell overlap throughout sorting. Consistent with the biologically relevant parameters of SR > 0.2, and the time for actual sorting to fall between 20 and 40 hr APF (red boxes in Figures 2.6K–M), these combinatorial stop rules exhibit a high probability of perfect wiring (yellow) for SR > 0.3 despite the random angle variation (Figures S2.4B and S2.4C). In summary, our model indicates that ‘‘combinatorial overlap’’ stop rules that utilize R-cell front overlaps, as observed in the imaging data, greatly improve robustness of the stop rule. The model further predicts optimal sensing radii between 0.3 and 0.4, closely resembling the observed size of growth cone fronts (compare Figure 2.5E and Figures 2.6A–G). However, our modeling results alone only reveal the ‘‘combinatorial overlap’’ stop rule as a robust solution, but do not exclude the ‘‘target only’’ or ‘‘no interaction’’ stop rules.

2.3.6 Validation at the Equator: The Three Neural Superposition Rules Provide an Explanation for Reduced Equator Wiring Robustness and All Four Types of Rotational Stereotypy within Cartridges Observed in Wild-Type

A test of the growth cone extension and stop rules in perturbation experiments by ablating R- or L-cells is not easily possible, because loss of any of the involved cell types disrupts the scaffold. However, the wiring pattern around the equator provides an important natural experiment that tests the model: six rows of cartridges have varying composition and represent three different degrees of disruption of the canonical wiring pattern (Figures 2.1C and 2.7A). Specifically, cartridges of the three rows near the equator differ from the canonical cartridge patterning by containing: an extra R3 (wiring-type ‘‘7R;’’ Figure 2.7A), an extra R3, an d an extra R4 (‘‘8R type 1;’’ Figure 2.7A) and extra R2, R3, R4, and R5 with missing R1 and R6 cells (wiring-type ‘‘8R type 2’’; Figure 2.7A), respectively. Each of the three equator cartridge types exhibits a distinct pattern of rotational stereotypy (Figures 2.1C and 2.7A) (Horridge and Meinertzhagen, 1970; Meinertzhagen, 1972). This enigmatic and ‘‘overly precise’’ wiring specificity has remained unexplained.

The computational model based on a combinatorial stop rule generates precise equator wiring and all precise patterns of rotational stereotypy in the placement of R-cell terminals in cartridge profiles (Figure 2.7B; Movie S7). This observation suggests that the apparent precision of the wiring pattern is a side effect of the developmental algorithm presented here. The observed four types of R-terminal rotational stereotypy also provide support for the idea that R-cell front interactions are part of the stop rule. The measured vectors (Figure 2.3J) and R front overlap (Figure 2.6) alone do not obviously lead to rotational stereotypy. However, recognition and ‘‘sandwiching’’ between direct neighbors provide an elegant mechanism that preserves the rotational stereotypy, whereas it is more difficult to envision how

R-cell fronts would retain the exact same two R-cell subtypes as neighbors without sensing each other.

To test more directly the role of interactions between R-cell fronts during growth cone targeting, we analyzed the growth cone dynamics and robustness underlying extension and stop rules in the equator versus main lamina. The longest growth cones (R3s) need to navigate seven different environments near the equator (red vectors in Figure 2.7A). We hypothesized that if R-cell front interactions instruct either the growth cone's extension angle or its speed, then the altered equator environments should cause altered growth cone behavior. To test this hypothesis, we compared growth cones at the equator with those in the main lamina. As shown in Figure 2.7C, outlines of equator and non-equator R3s and R4s appear indistinguishable for all measured parameters and time points. Specifically, we measured heel-front length (Figure 2.7D), heel-front filopodia length (Figure 2.7E), heel-front angle (Figure 2.7F), heel-front filopodia angle (Figure 2.7G), and the lengths and angles of heel-heel filopodia and front-front filopodia (Figure S2.5A). These measurements support the idea that R growth cones extend according to the same guiding principle in both equatorial and non-equatorial regions. However, it is difficult to envision a molecular mechanism for interactions between the R-cell fronts for the seven different environments that would lead to identical dynamics. We conclude that these measurements do not support a mechanism whereby R front-R front interactions (for R-cells originating in different bundles) instruct extension angle or speed.

Next, we asked whether R-cell front interactions might play a role as part of the stop rule, as suggested by our robustness analyses in the main lamina (Figures 2.6K–M) and the

observation of rotational stereotypy in all parts of the lamina (Figures 2.1C and 2.7B). The equator region provides a decisive test, as our model predicts reduced robustness at the equator for any stop rule that involves R-cell front interactions, but not for ‘‘target only’’ or ‘‘no interaction’’ stop rules (comp. Figures S2.5B–D and Figures 2.6K–M). The ‘‘target only’’ stop rule has the same robustness at and away from the equator, with wiring succeeding or failing at the same sensing radii (red vertical line in Figure 2.7H) because the target grid is isotropic across the entire lamina (e.g., Figure 2.5A). Similarly, all ‘‘no interaction’’ stop rules have the same robustness at or away from the equator (data not shown), because the stopping condition is independent of the R-cell environment. In contrast, all stop rules based on R front sensing exhibit reduced equator robustness compared with neural superposition wiring in the main lamina (broken red lines in Figures 2.7I–M). This is consistent with the prediction that increased numbers of R-cell fronts at the equator more easily lead to a premature stop, which results from an R-cell front meeting head on with other R-cell fronts. Hence, we hypothesize that if R front sensing is part of the stop rule, the wild-type equator should exhibit reduced robustness, which would be apparent as an increased wild-type error rate.

A test of this hypothesis is available in the form of two seminal single-axon tracing studies in the neural superposition eye of the blow fly Calliphora (Horridge and Meinertzhagen, 1970; Meinertzhagen, 1972). Of a combined ~1,200 individually traced axons, none terminated in an incorrect neural superposition cartridge of the main lamina. In contrast, Meinertzhagen (1972) identified 17 targeting errors at a wild-type equator. All of these targeting errors represent premature stops in the correct direction, as predicted by our model.

Finally, rotational stereotypy errors are more commonly observed, but again are almost exclusively observed at the equator (Horridge and Meinertzhagen, 1970; Meinertzhagen, 1972). Hence, the observation of wiring errors at the wild-type equator, in conjunction with the observations that R-cell front interactions are not required during extension, supports the hypothesis that R-cell front interactions are part of the stop rule and argues against both the ‘‘no interaction’’ and ‘‘target only’’ stop rules. Similar to the equator, our model generates edge cartridges at the borders of the lamina that match and explain experimental observations (Meinertzhagen and Hanson, 1993) (Supplemental Experimental Procedures; Figure S2.6).

2.4 DISCUSSION

Here, we describe a developmental algorithm for the axonal sorting of ~4,800 presynaptic cells in the primary visual map of Drosophila. Our work suggests that the neural superposition wiring diagram found in adult fly brains can be established through simple, local pattern formation principles without the need for an elaborate molecular matchmaking code. Our codification of the developmental algorithm reveals quantitative constraints and provides a conceptual framework for molecular mechanisms that execute these rules.

2.4.1 Three Rules to Ring Them All

Our findings, together with previous studies, support the following developmental algorithm.

Rule 1: The Scaffolding Rule

Incoming rows of axon bundles from individual ommatidia are organized in a repeating pattern of evenly spaced semi-circles. This pattern and spacing of original axon arrival points provide a scaffold that remains stable during the entire process of growth cone sorting and is required for neural superposition. The future target areas are encircled by the anchored heels and thus already defined prior to growth cone movements. How the precision of the scaffold pattern develops is unknown. The scaffold is likely to instruct the extension angle through non-autonomous R-cell interactions within a bundle (Chen and Clandinin, 2008). Such intra-bundle interactions have been proposed to play a more prominent role than do interactions across bundles (Schwabe et al., 2013). To which extent the geometric arrangement of heels observed in the scaffold is influenced by their axonal arrangements within the bundles or by other cells within the target area is unclear.

Rule 2: The Extension Rule

All R1–R6 growth cones extend synchronously with speeds and angles specific to their R-cell subtype during the 5–10 hr of extension. The extension is unaffected by highly varying environments at the equator and thus is unlikely to depend on R-cell front interactions. However, precise extension dynamics may require permissive R-cell heel interactions and recognition of other cells that are equally distributed across the equator as instructive guides. It is unlikely that R-cell growth cones simply extend toward attractive cues at the target regions because the growth cones can overlap with several target regions throughout their sorting (including the target regions closest to the heels). Based on these observations, we consider that the extension

process of the bipolar R-cell growth cones differs from the classic view of growth cone movements toward attractive targets (Caudy and Bentley, 1986; Mason and Erskine, 2000).

Rule 3: The Stop Rule

The target regions defined by the scaffold (and the L-cells therein) provide possible, but poor, targets for R-cell fronts to stop extending, because those R-cell fronts overlap with multiple targets simultaneously and throughout their extension. In addition, all R-cell fronts increasingly overlap with other R-cell fronts throughout their extension. The computational model reveals that stop rules based on R-cell front overlap function even without any target-derived cues and are more robust than a ‘‘target only’’ model under the same conditions. A target model using coincidence detection of overlap with other R fronts, as well as target L-cells, performs best. R-cell front interaction is predicted to be part of the stop rule because of reduced robustness at the equator and because of the rotational stereotypy of R-cell terminal positions within cartridges. These two observations also argue against ‘‘no interaction’’ stop rules. However, our results do not rule out the existence of a synchronously applied stop signal that could act as part of a combinatorial stop rule. The precise nature and molecular correlate of the stop rule remain unknown.

Previous work has revealed important insights into further constraints of these rules. Most importantly, Clandinin and Zipursky (2000) have shown that the 180° rotation of a single bundle results in 180° rotated extension angles. This finding is consistent with our model. In addition, Clandinin and Zipursky (2000) unraveled differential subtype dependencies, where R1, R2, R5 and R6 targeting depend on R3 and R4, but not the other way round. Whether this

dependency arises from the scaffolding, extension, or stop rule remains to be determined. It is not yet known whether reconciliation of our model with these observations arises from constraining existing rules or requires new ones.

After growth cone sorting is complete, a process of centripetal growth commences synchronously from all R-cell fronts and these then generate R-cell terminal columns orthogonal to the lamina plexus (Movie 4). This columnar extension preserves and freezes the relative positions of R-cell fronts in the lamina plexus; the resulting columns of R-cell terminals then define the adult lamina.

2.4.2 On Developmental Rules and Molecular Mechanisms

Complicated wiring diagrams can originate through the iterative execution of simple rules (Chan et al., 2011; Langen et al., 2013; Rivera-Alba et al., 2011). Early brain development is associated with genetically encoded pattern formation rules, while later phases of synapse specification often depend on neuronal activity (Shatz, 1996). It is unclear which level of synaptic partner specification can be achieved through simple, genetically encoded developmental rules. In this study we focused on the identification of such rules and their quantitative constraints using the genetically hard-wired Drosophila visual map as a model (Clandinin and Zipursky, 2002; Hiesinger et al., 2006).

Much previous elegant work has focused on searching for molecular codes underlying synaptic partner specification. Such codes may be characterized by either many molecular cues (e.g., olfactory systems) or fewer molecular cues that are dynamically localized (e.g., the fly's visual system) (Clandinin and Zipursky, 2002; Yogev and Shen, 2014; Zipursky and Sanes, 2010). Our work on identifying an underlying developmental algorithm provides a framework for matching these molecular mechanisms with the rules they execute. For example, recent studies on guidance receptors of the Cadherin family have provided strong evidence for a role of differential adhesion in R-cell growth cone sorting (Schwabe et al., 2014; Schwabe et al., 2013). Specifically, R-cell growth cones interact through differential adhesion of the protocadherin Flamingo, both within the same bundle (Chen and Clandinin, 2008) and across bundles (Schwabe et al., 2013). Our data are consistent with the idea that Flamingo- dependent differential adhesion between R-cell heels prior to extension determines the extension angle (thus exercising a role in the scaffolding rule). In contrast, interactions between moving R-cell fronts are unlikely to instruct extension itself (no role in the extension rule). However, studies on the guidance receptor N-Cadherin suggest a role for the interaction of R-cell growth cones with L-cells in the target cartridge (Prakash et al., 2005). These findings are consistent with a role of N-Cadherin-mediated interactions between R-cell fronts and L-cells as part of the stop rule and thereby indicate that L-cell interactions contribute to the stop rule. These interpretations of roles of Flamingo in the R-cell heel (as part of the scaffolding rule) and N-Cadherin in the R-cell front (as part of the stop rule) are further supported by their subcellular localization within the growth cone (Schwabe et al., 2013).

Finally, our model supports R-cell front interactions as part of the stop rule. It is unclear to which degree this interaction is based on differential adhesion. How molecular signal integration is implemented to utilize the substantial increasing overlap of R-cell fronts as a stop signal remains to be discovered.

2.4.3 Wiring Specificity as a Product of the Developmental Algorithm

Both the equator and the rotational stereotypy of R-cell terminals have received little recent attention in the study of growth cone sorting and neural superposition, perhaps because they appear to be complications of an already complicated wiring problem. In particular, the findings of four types of rotational stereotypy within cartridges across the entire lamina have to our knowledge not been addressed in the literature since their discovery more than 40 years ago (Horridge and Meinertzhagen, 1970; Meinertzhagen, 1972). The stereotypic arrangement of R1–R6 terminals in cartridges that encode precise neural superposition increases the apparent number of target slots 6-fold; yet, this arrangement is not required for neural superposition, given that all six carry the same information and synapse with the same output neurons. Here, we show that evolutionary selection of the developmental algorithm that ensures precise axon sorting required for neural superposition wiring is sufficient to establish rotational stereotypy. While it is possible that rotational stereotypy may serve a function independent of neural superposition, selection for such a putative unknown function is not required to explain its occurrence. Hence, the fly's visual map provides an example for a neuronal circuit whose connectivity map can only

be understood through its developmental context. Knowledge of a circuit's developmental algorithm may more generally help to explain aspects of neuronal circuits that cannot be derived from the study of the adult wiring diagrams alone.

2.5 CHAPTER TWO FIGURES

Figure 1

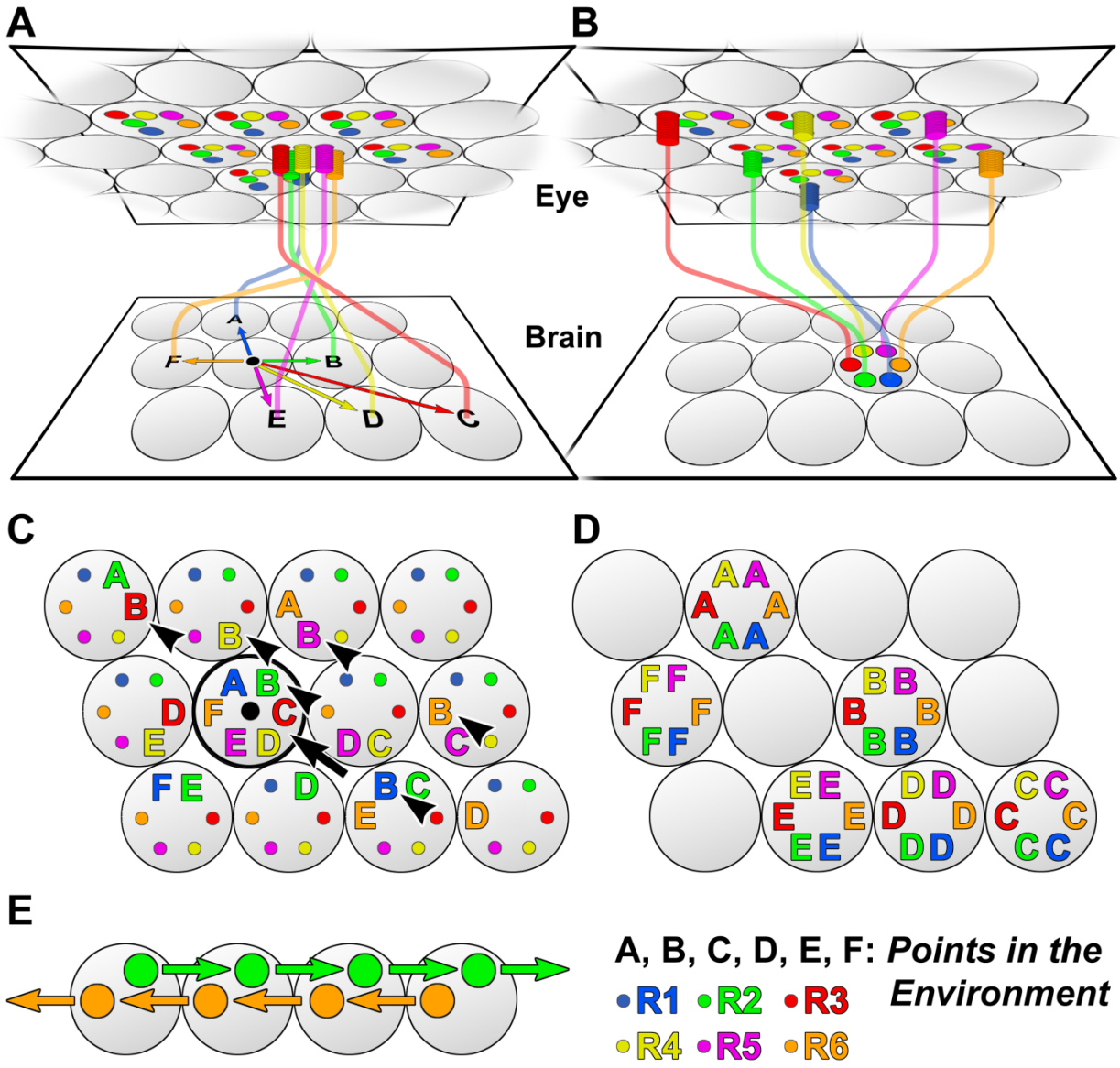

Figure 2 1. The Neural Superposition Sorting Problem

(A) The six outer photoreceptors R1–R6 from a single unit eye (ommatidium) receive input from six different points in the visual environment and project to six separate synaptic units (cartridges) in the brain. (B) The six R1–R6 photoreceptors from six different ommatidia that receive input from the same point in visual space connect to the same cartridge, in a pattern that is the reciprocal of that in (A). (C) Schematic view of a lamina section from dorsal (left) to ventral (right) across the equator. The colorcoded R1–R6 axons from different ommatidia that receive input from points in the environment (A)–(F) are shown in their final cartridge arrangement on the left. The circular arrangement of axon terminals in the cartridges shows the precise rotational stereotypic arrangement of R1–R6.

Figure 2

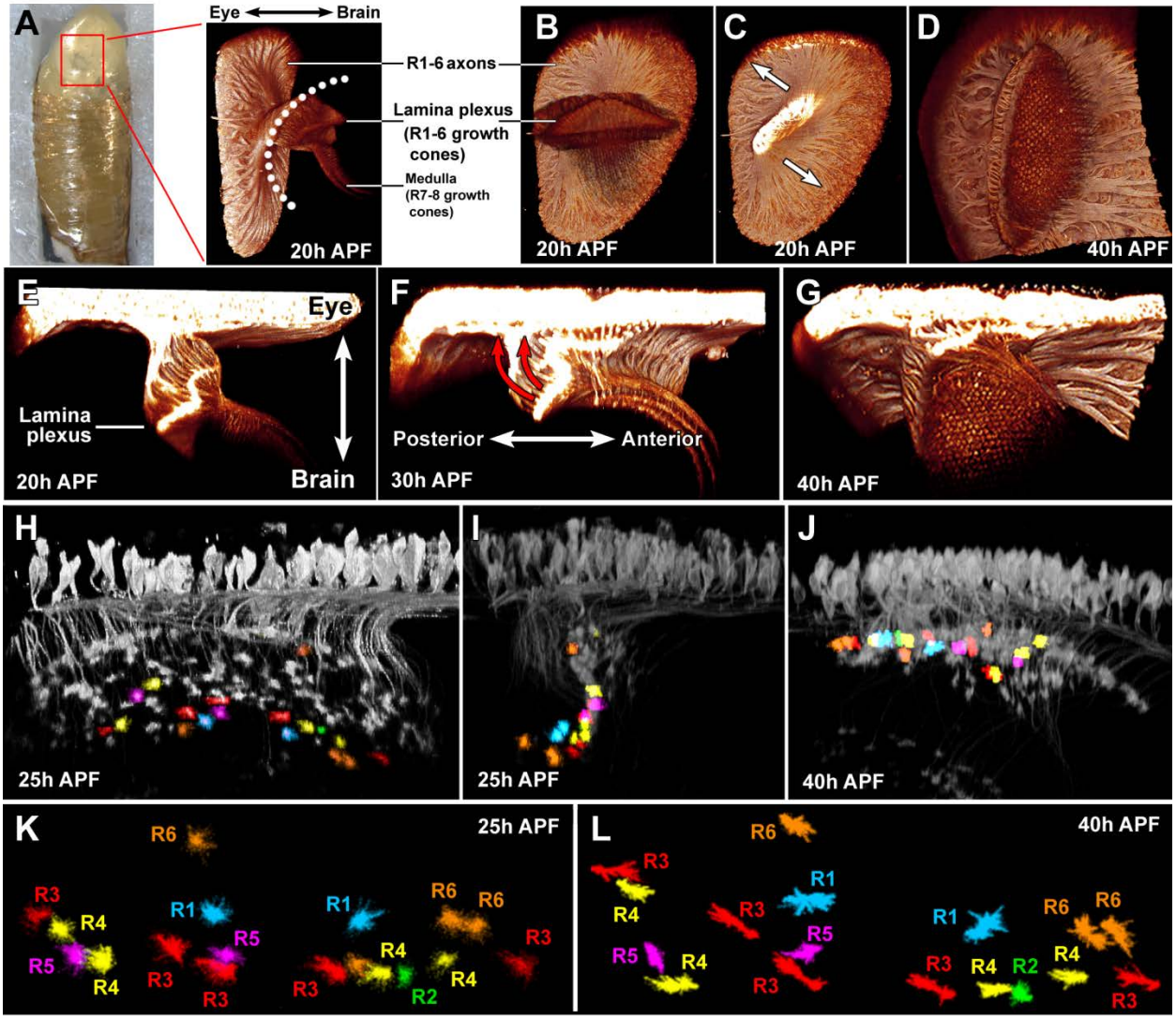
A
Eye
Brain
R1-6 axons
Lamina plexus
(R1-6 growth cones)
Medulla
(R7-8 growth cones)
20h APF
B
20h APF
C
20h APF
D
40h APF
E
Eye
Lamina plexus
20h APF
Brain
F
Posterior
Anterior
30h APF
G
40h APF
H
25h APF
I
25h APF
J
40h APF
K
25h APF
L
40h APF

Figure 2 2. Intravital Imaging Reveals the Morphogenesis of the Lamina and Photoreceptor Growth Cones during Brain Development

(A) Imaging chamber for two-photon live imaging through the intact developing pupal eye. Right: side view of all photoreceptors labeled with membrane-tagged CD4-tdGFP at 20 hr APF. (B–D) View of the same specimen as in (A) from inside the brain (B), with the axons viewed from a cut plane between eye and lamina (C) and after 20 hr hours of further development (D). (E–G) Side view of the same specimen as in (A)–(D) in 10 hr developmental intervals. See also Movie S1. (H–J) Side views of a specimen at the indicated time points with sparse photoreceptor labeling and individual identified growth cones marked in R1- to R6-specific colors as defined in Figure 1. (K and L) Visualization of individually segmented growth cones from the specimen shown in (H)–(J) at 25 hr APF (K) and 40 hr APF (L). See also Movies S1 and S2.

Figure 3

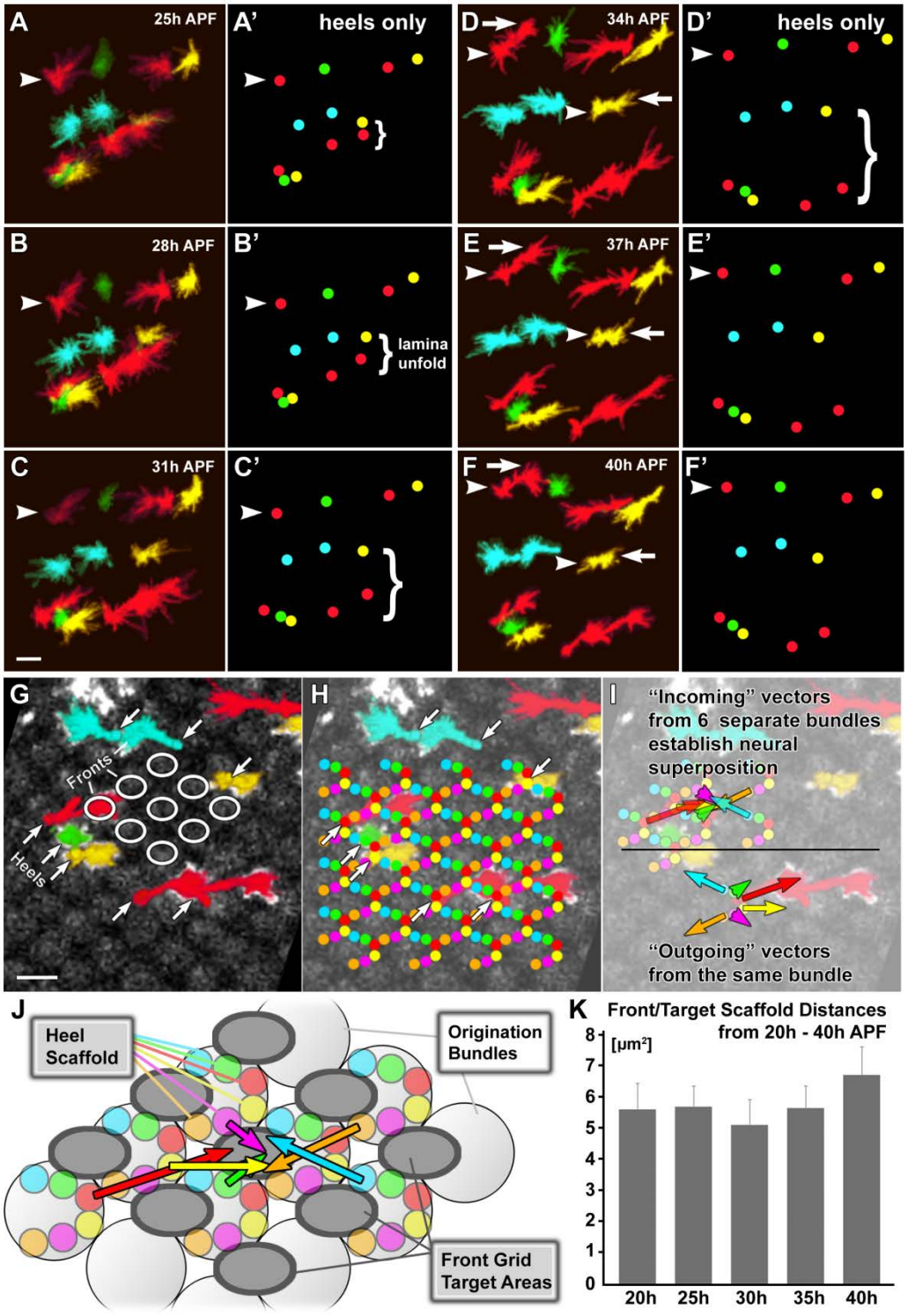
A
25h APF
A'
heels only
D
34h APF
D'
heels only
B
28h APF
B'
lamina unfold
E
37h APF
E'
C
31h APF
C'
F
40h APF
F'
G
Fronts
Heels
H
I
"Incoming" vectors from 6 separate bundles establish neural superposition
"Outgoing" vectors from the same bundle
J
Heel Scaffold
Origination Bundles
Front Grid Target Areas
K
Front/Target Scaffold Distances from 20h - 40h APF
[μm²]
8
7
6
5
4
3
2
1
0
20h
25h
30h
35h
40h

Figure 2 3. The Scaffolding Rule: Bipolar Growth Cones Generate a Stable Framework that Facilitates the Sorting Problem

(A–F) Movements of a cluster of 12 growth cones between 25 and 40 hr APF. Arrowheads denote heels; arrows mark growth cone fronts. (A'–F') The positions of the heels only are shown. Note that the lower part of this cluster expands due to lamina unfolding between 25–34 hr APF, yet no heels shift relative to each other. Scale bars, 5 mm. See Movies S2 and S3. (G–I) Cross-section through the lamina plexus at 40 hr APF for the same specimen as shown in (A)–(F). (G) Background labeling reveals a rhomboidal 80°/100° grid in the lamina plexus that overlaps all growth cone fronts (ovals). In contrast, all heels (arrows) are located outside the grid defined by R-cell fronts. Scale bars, 5 mm. (H) Extrapolation of the position of all heels in the scaffold. (I) Vectors of R1–R6 growth cones at 40 hr APF based on measurements at 40 hr APF. (J) Updated schematic of growth cone sorting in the lamina plexus, viewed from the eye, based on the schematics shown in Figure 1C. Note that the heels have a horseshoe-shaped arrangement within the circular ''arrival units'' shown in Figure 1C, whereas the target ovals form an intercalated grid. (K) Cartridge distances in the lamina plexus between 20 and 40 hr APF reveal scaffold stability throughout growth cone sorting. Measurements were taken from fixed preparations shown in Figure S1. Data shown are mean ± SD (n is R67 for each time point). See also Figure S1 and Movies S3 and S4.

Figure 4

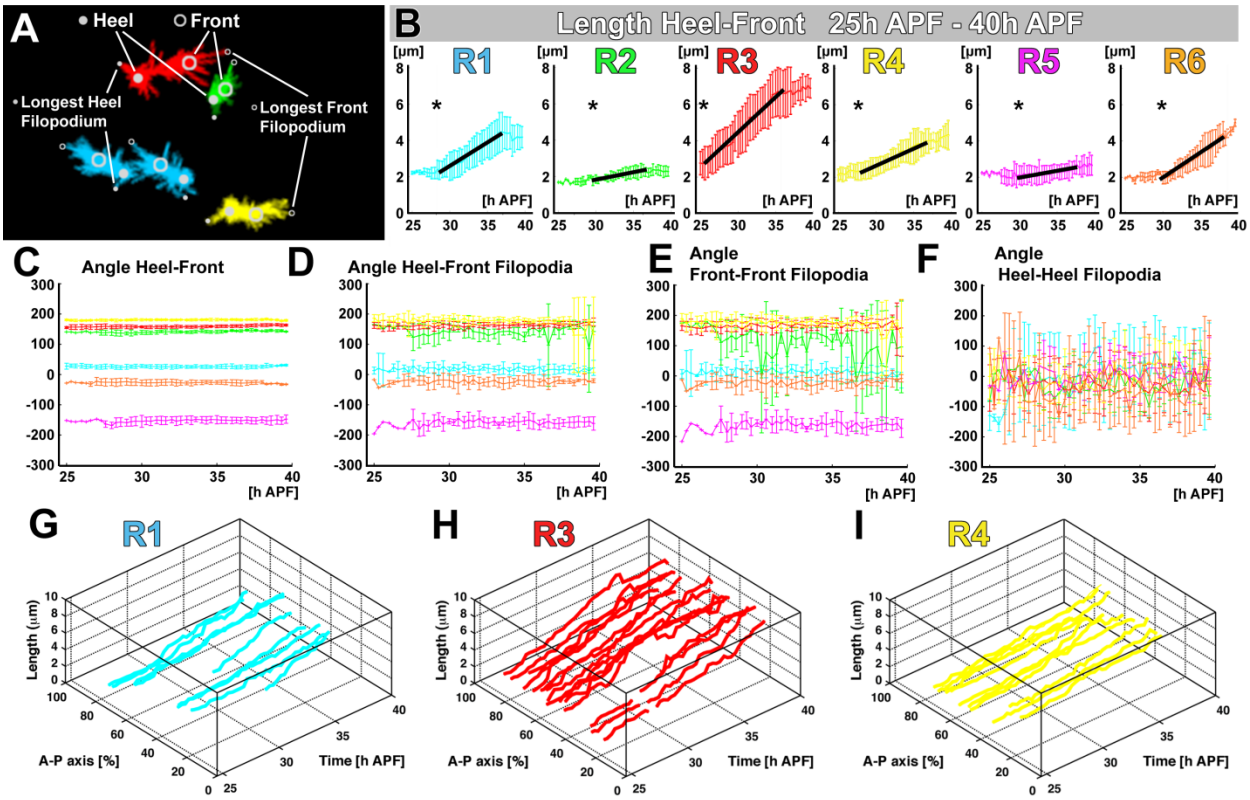

Figure 2 4. The Extension Rule: Quantitative Analysis of Growth Cone Dynamics Reveals Synchronized Extension Programs Specific for Each R1–R6 Subtype

(A) Schematic of quantified heel, front, and filopodial positions (same specimen as in Figure 3). (B) Heel-front distance for R1–R6 between 25–40 hr APF. Asterisks denote the subtype-specific initiation of extension and black lines highlight periods of nearlinear extension. (C) Heel-front angles between 25–40 hr APF reveal angle constancy for R1–R6 throughout the sorting process. (D) Angles between heel and longest front filopodium reveal average filopodial explorations at closely matching angles. (E and F) Angles of the longest front and heel filopodial exploration. (G–I) Extension dynamics are identical across the A-P axis, indicating synchronous movements across the entire lamina plexus. (B–F) Data shown are mean ± SD. See also Figure S2.

Figure 5

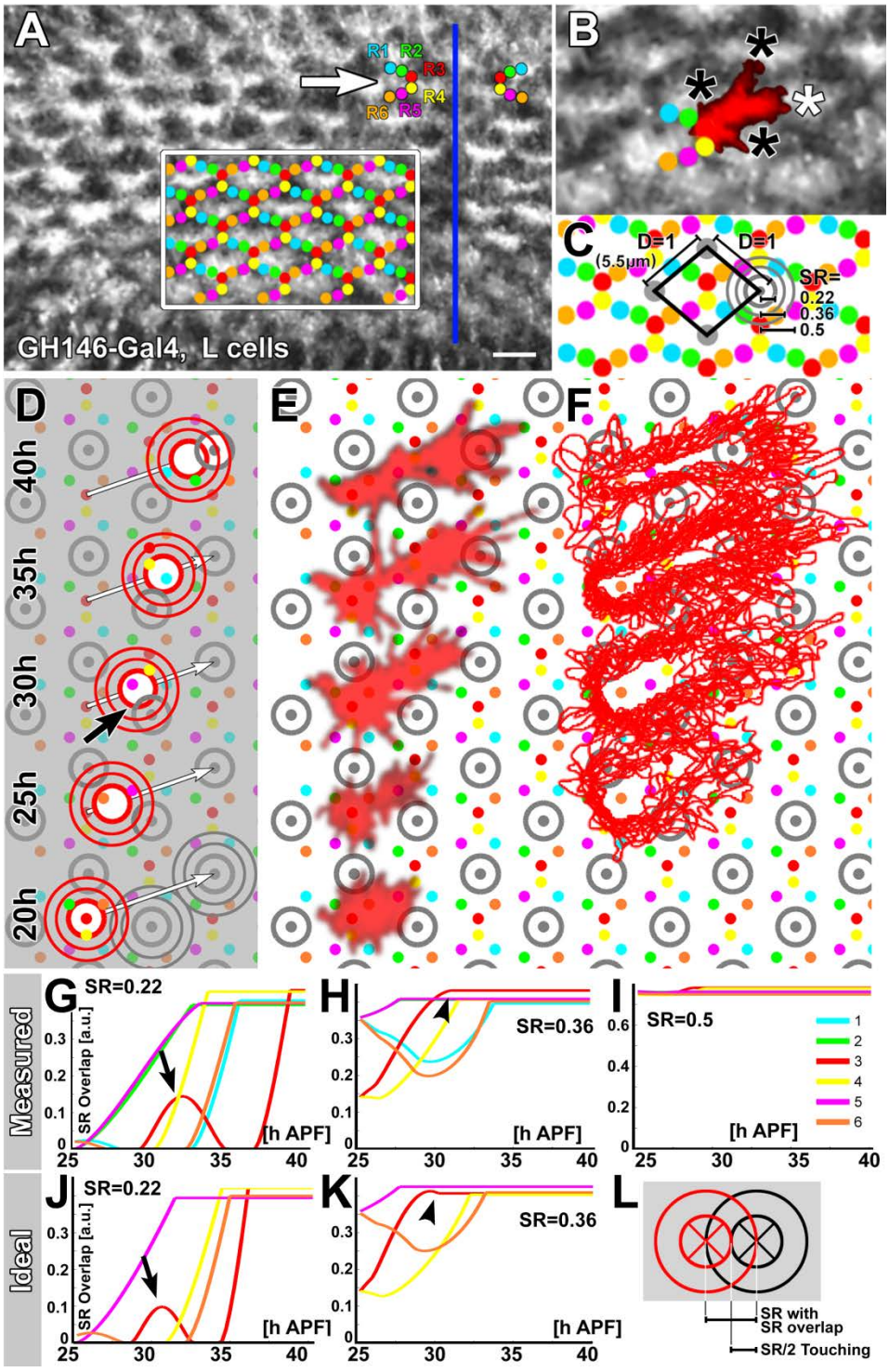
A
R1 R2
R3
R4
R6 R5
GH146-Gal4, L cells
B
C
D=1
(5.5μm)
D=1
SR=
0.22
0.36
0.5
D
40h
35h
30h
25h
20h
E
F
Measured
G
SR=0.22
SR Overlap [a.u.]
[h APF]
H
SR=0.36
I
SR=0.5
1
2
3
4
5
6
Ideal
J
SR=0.22
K
SR=0.36
L
SR with
SR overlap
SR/2 Touching

Figure 2 5. The Stop Rule, Part 1: How Good a Target Is the Target?

(A) Single frame at 28 hr APF from a 20 hr timelapse movie of all target L-cells. Arrow indicates single representative heel bundle (arrival unit). The boxed area marks the heel scaffold, and the blue line marks the equator. Scale bars, 5 mm. (B) Enlarged region within the box in (A) with one heel bundle shown. The shape of a representative R3 originating from this heel bundle reveals overlap with at least three incorrect targets (black asterisks) in addition to the correct target (white asterisk). (C) Reference schematic for quantifications and the computational model; see text for details. (D–F) Analysis of target recognition with different sensing radii for an R-cell front in a schematic (D), a single representative R3 growth cone (E), and an overlay of all R3 growth cones analyzed for this study. The blue shapes in (D) illustrate alternative sensing areas. (G–L) Overlap with any target throughout the simulated move of three R-cell sensing fronts of differing radii. Arrows indicate partial overlap, and arrowheads indicate premature final stops. See also Figure S3.

Figure 6

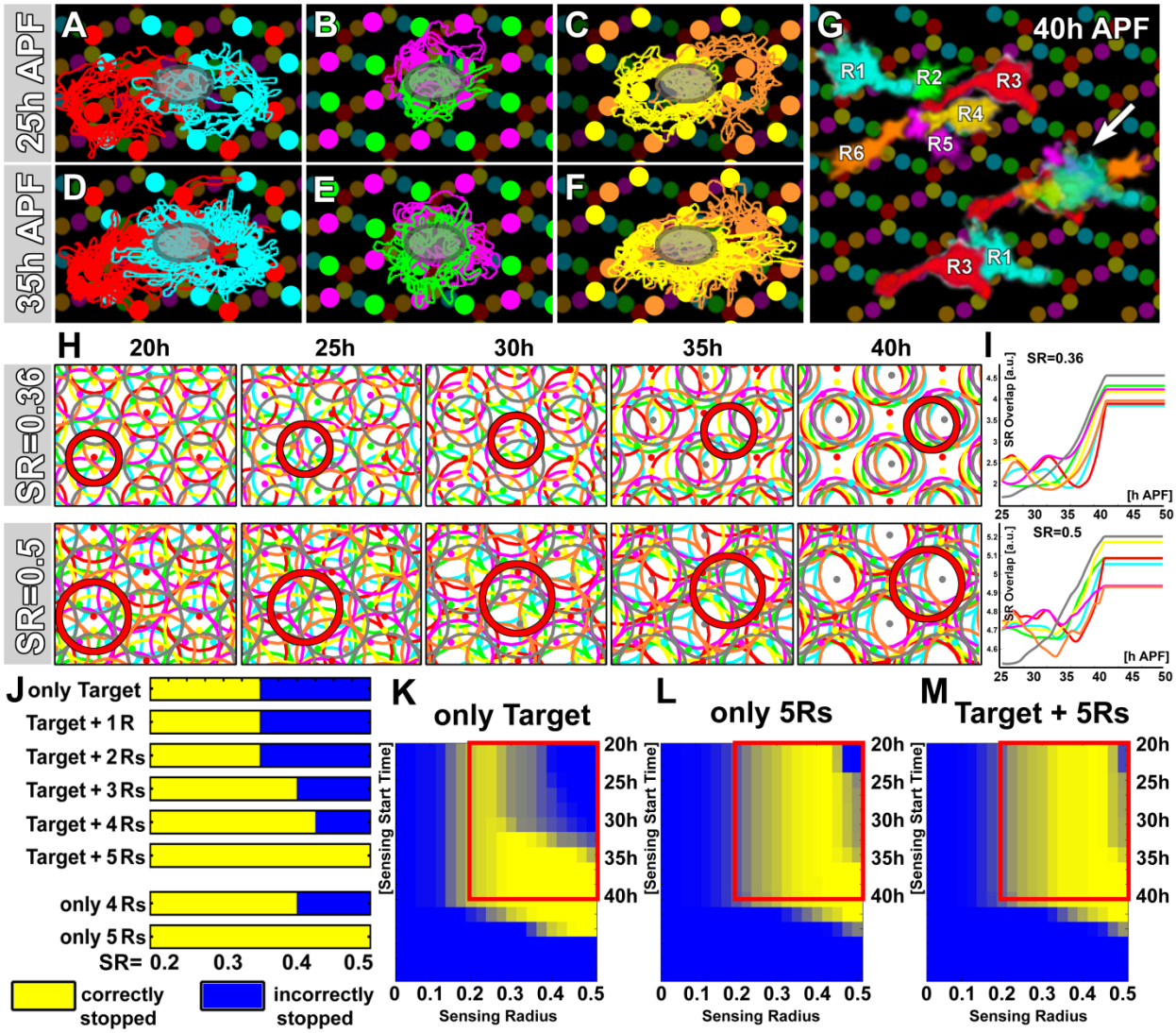
25h APF
35h APF
A
B
C
D
E
F
G
40h APF
R1
R2
R3
R4
R5
R6
R3
R1
H
20h
25h
30h
35h
40h
SR=0.36
SR=0.5
I
SR=0.36
SR=0.5
SR Overlap [a.u.]
[h APF]
J
only Target
Target + 1 R
Target + 2 Rs
Target + 3 Rs
Target + 4 Rs
Target + 5 Rs
only 4 Rs
only 5 Rs
SR= 0.2 0.3 0.4 0.5
correctly stopped
incorrectly stopped
K
only Target
L
only 5Rs
M
Target + 5Rs
[Sensing Start Time]
20h
25h
30h
35h
40h
0 0.1 0.2 0.3 0.4 0.5
Sensing Radius

Figure 2 6. The Stop Rule, Part 2: R1–R6 Growth Cone Front Overlaps Can Increase the Robustness of the Stop Rule

(A–F) R1–R6 outlines from intravital imaging data for 25 hr APF (A–C) and 35 hr APF (D–F). The outlines are shown in subtype pairs for R1+R3 (A and D), R2+R5 (B and E), and R4+R6) (C and F) to highlight the amount of and increase in overlap in the target area (dark ovals) during the 10 hr of growth cone extension. (G) Representative growth cones at 40 hr APF. The ‘‘outgoing’’ growth cones from one bundle, the ‘‘incoming’’ growth cones to one target (arrow), and a pair or R1+R3 to highlight covering and overlap in the target area are shown. (H) Computer simulations with a stop rule using coincidence detection of the target, plus all other R fronts and the sensing radii 0.36 and 0.5. (I) R1–R6 front overlaps with other R-cell fronts or targets with the noted sensing radii. (J) Systematic parameter scan of all combinatorial stop rules and sensing areas from SR = 0.2–0.5. (K–M) Systematic scans for sensing radii 0–0.5, sensing start time 20–40 hr, and ±10° randomly varied extension angles are shown for the ‘‘target only’’ rule and two combinatorial stop rules without (L) and with target (M). Each data point was simulated 100 times for angles that were randomly offset ± 10° (Figure S4). See also Figures S4 and S5 and Movie S6.

Figure 7

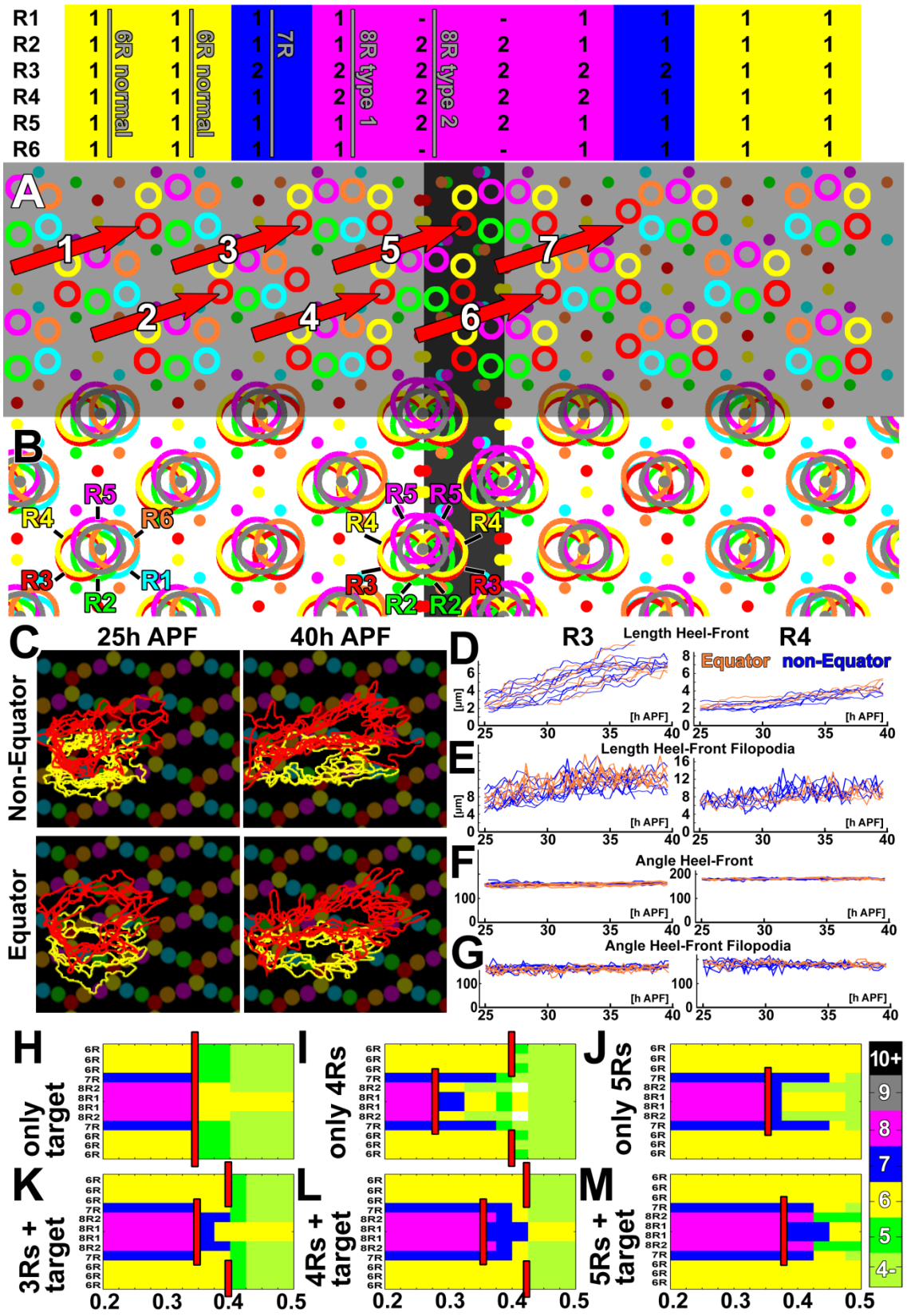
R1 1 1 1 1 1 1 - - 1 1 1 1
R2 1 1 1 1 1 1 2 2 1 1 1 1
R3 1 1 2 2 2 2 2 2 2 2 1 1
R4 1 1 1 2 2 2 2 2 1 1 1 1
R5 1 1 1 1 1 2 2 1 1 1 1 1
R6 1 1 1 1 - - - 1 1 1 1 1
6R normal
6R normal
7R
8R type 1
8R type 2
A
1
2
3
4
5
6
7
B
R5
R4
R6
R3
R1
R2
C
25h APF
40h APF
Non-Equator
Equator
D
R3
Length Heel-Front
R4
Equator
non-Equator
[µm]
[h APF]
E
Length Heel-Front Filopodia
F
Angle Heel-Front
G
Angle Heel-Front Filopodia
H
only target
I
only 4Rs
J
only 5Rs
K
3Rs + target
L
4Rs + target
M
5Rs + target
10+
9
8
7
6
5
4-

Figure 2 7. The Equator and Rotational Stereotypy Validate the Developmental Algorithm and Indicate a Role for R1–R6 Overlap Sensing as Part of the Stop Rule, but Not of the Extension Rule

(A and B) Schematic of all types of main and equator-type cartridges, their composition (top), the stereotypy of the arrangement of the varying types of R-cells (A), and the result of a simulation of the developmental algorithm using the computational model (B). Simulation with SR = 0.22 and a stop rule of ‘‘target+4R’’. (C–G) Comparative analyses of R3 and R4 growth cone dynamics in the main lamina and across the equator. (H–M) Systematic parameter scans for the labeled stop rules and all sensing radii 0.2–0.5 across the main lamina and equator. The red bar indicates at which sensing radius correct superposition sorting fails. Note that all stop rules that include R front sensing exhibit reduced equator robustness at larger sensing radii. See also Figure S6 and Movie S7.

2.7 CHAPTER TWO SUPPLEMENTAL FIGURES

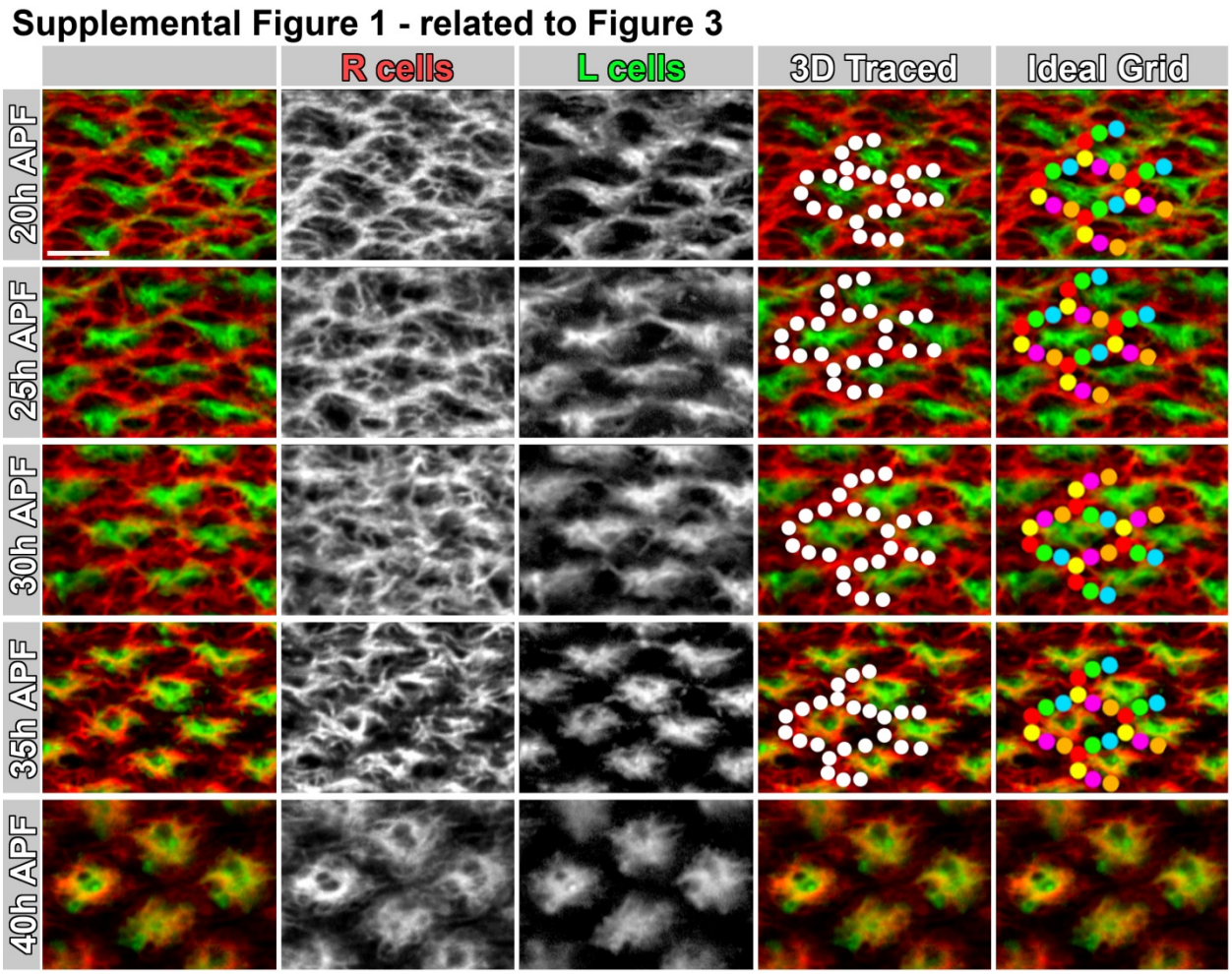

Figure S2.1. The Scaffold Remains Stable throughout the Sorting Process, Related to Figure 2.3

Fixed preparations of co-labelings of GH146-Gal4 driven CD4-tdGFP in L-cells (green) and anti-Chaoptin labeling of R-cells (red) from 20h APF (first row) through 40h APF (last row). At 20h-35h APF individual heel positions can be determined by following the axons (column 3D traced). In the co-labeling of the lamina plexus, the heel positions are visible as black regions encircled by Chaoptin labeling. The heel scaffold and distances between cartridge centers remain stable between 20h-35h APF (comp. Figure 3K). Scale bars, 5 mm.

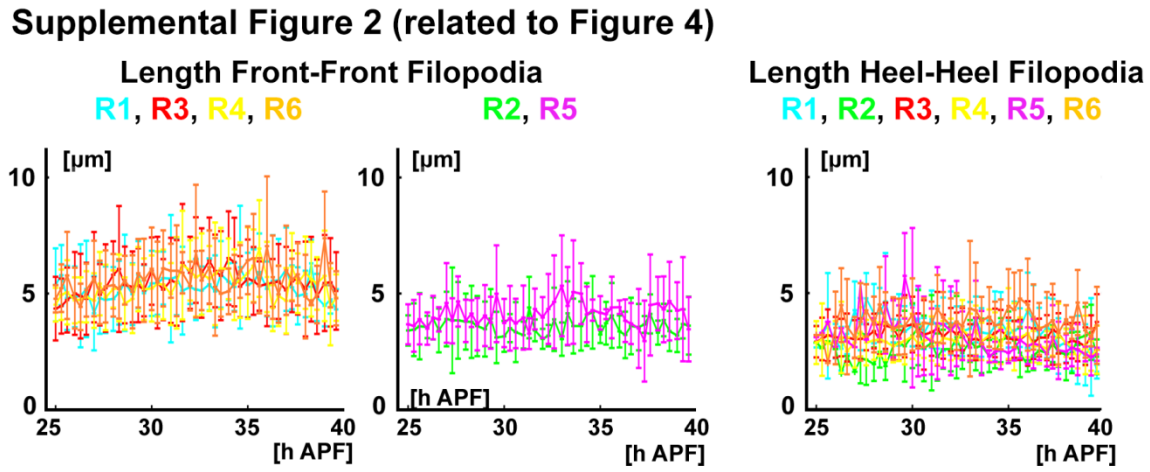

Figure S2 2. Front and Heel Filopodia Extend Characteristic Distances, Related to Figure 2.4

(Left panel) The longest front filopodia of R1, R3, R4 and R6 explore furthest between 30-35h, on average one cartridge diameter D (~5.5 mm). (Middle panel) The longest front filopodia of R2 and R5 explore less than 4 mm distance throughout the entire sorting period. (Right panel) The longest heel filopodia reveal shorter extensions than front filopodia. Data shown are mean ± SD.

Supplemental Figure 3 (related to Figure 5)

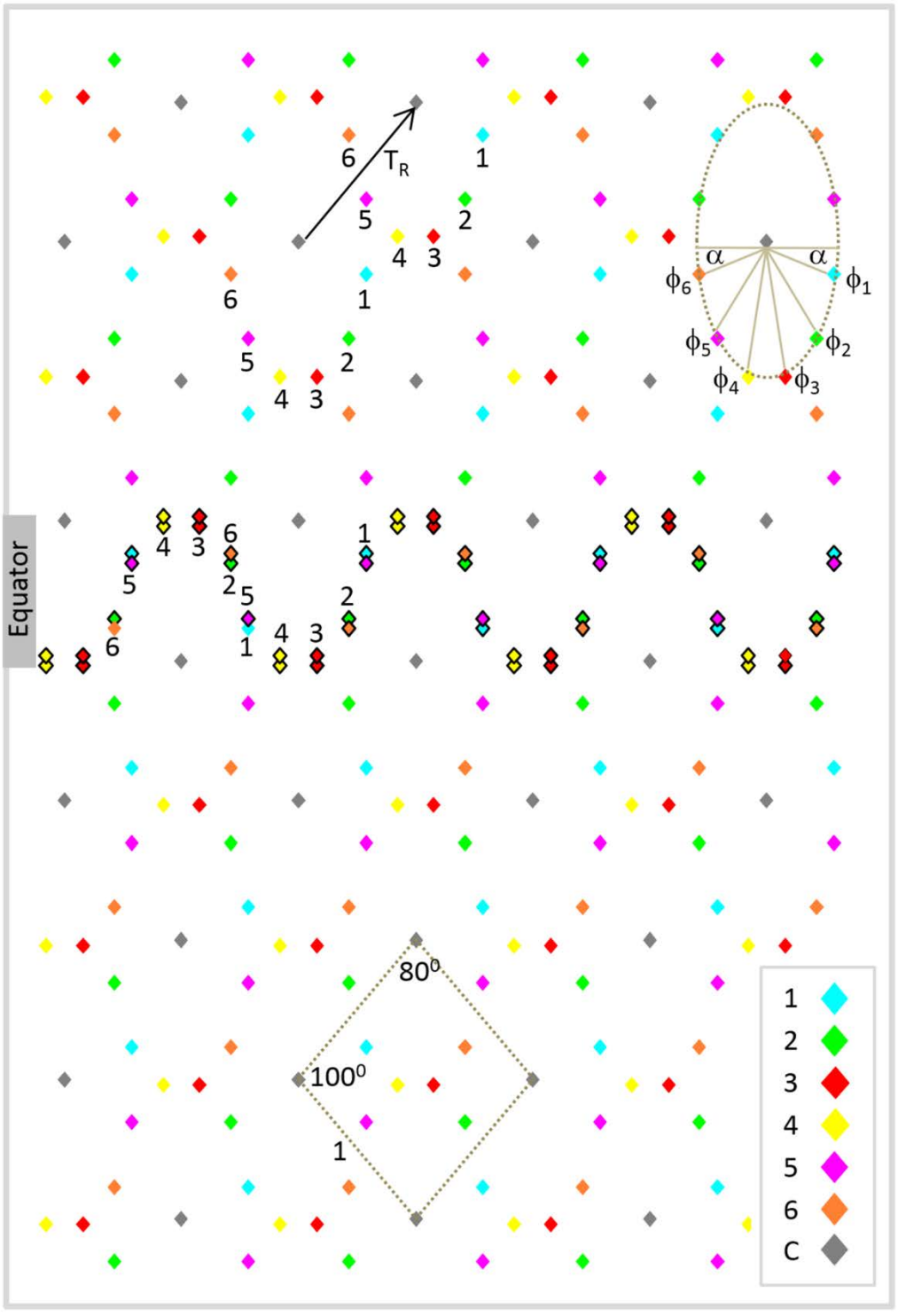

Figure S2 3. Quantitative Features of the Scaffold, Related to Figure 2.5

Based on measurements in the imaging data, the scaffold is a rhomboidal grid (80°/100° grid). The grid is uninterrupted across the equator, but the density of R-cells is locally increased with doubly occupied slots. The scaffold is computationally set up based on the cartridge distance TR and the angles as described in detail in the Supplemental Experimental Procedures.

Supplemental Figure 4 (related to Figure 6)

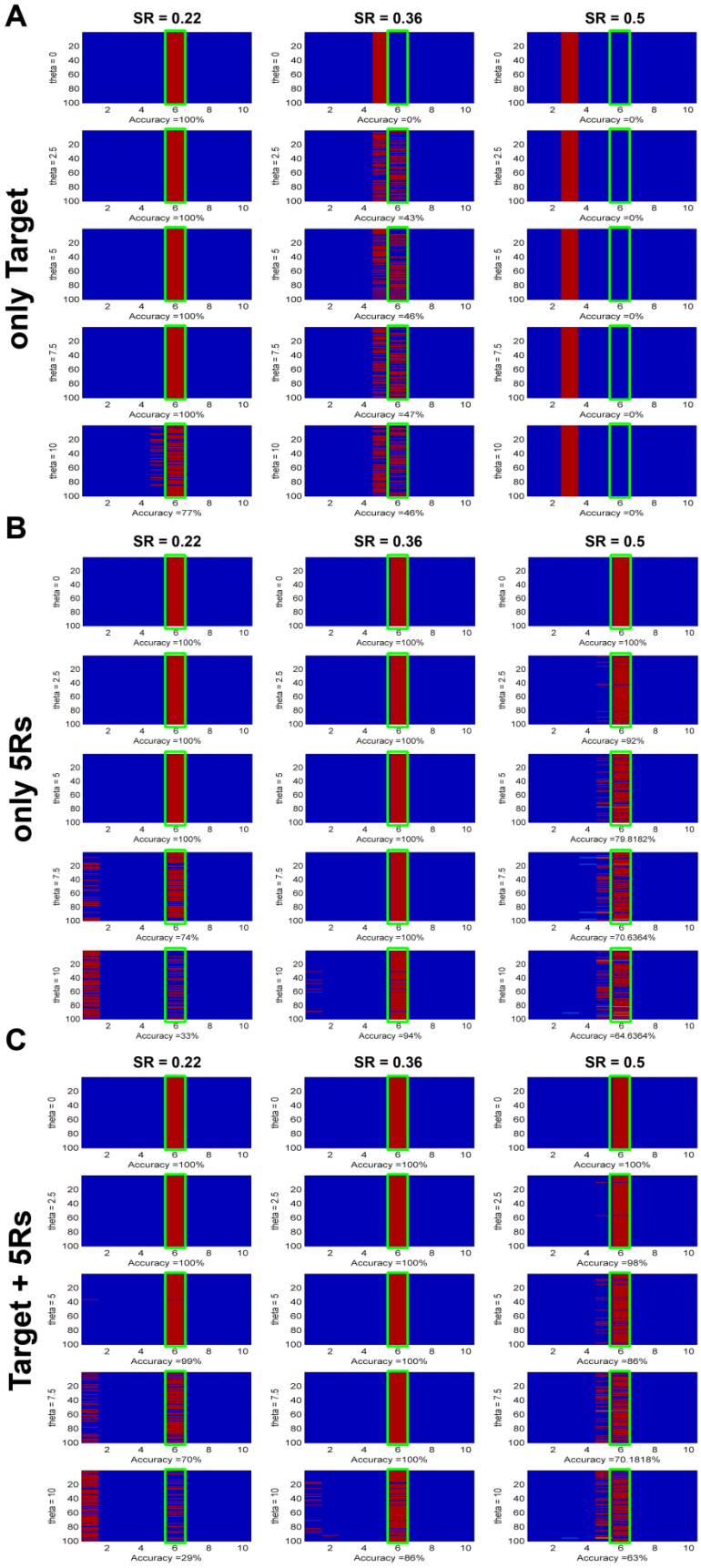

Figure S2 4. Simulations of Wiring Accuracy with Random Angle Variation, Related to Figure 2.6

(A–C) Shown are simulations for a sensing radius SR = 0.22 (left column), SR = 0.36 (middle column) and SR = 0.5 (right column). (A) Simulations for the 'only target' stop rule, (B) 'overlap with 5 other R-cells' stop rule; (C) 'overlap with target plus 5 other R-cells' stop rule. For each stop rule the first row shows 100 independent runs with no random angle variation, the second row 2.5 degree random variation, the third row 5 degree, the fourth row 7.5 degree, and the fifth row 10 degree random angle variation. All subtypes were independently varied randomly for each of the 100 runs shown in each plot. The green box marks the correct results of 6 terminals per cartridge. Orange marks results obtained in each run. Note that the 'only target' model fails with larger sensing radii, whereas the 'combinatorial overlap' stop rules function best with an intermediate sensing radius.

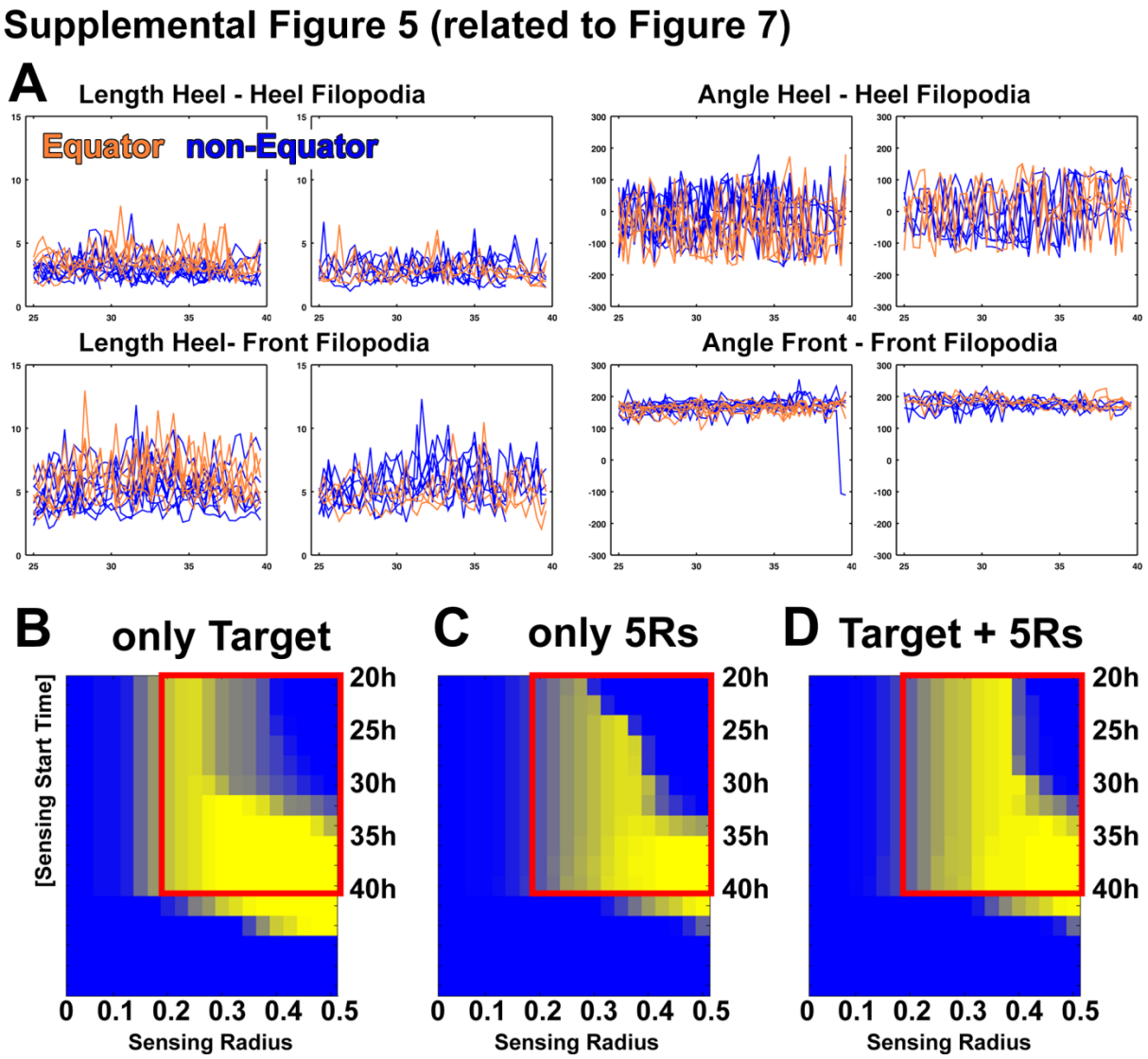

Figure S2 5. Wiring Accuracy at the Equator, Related to Figure 2.7

(A) Measurements of the lengths and angles of heel-heel and front-front filopodia reveal identical dynamics between equator and non-equator growth cones. (B–D) Systematic scans for sensing radii 0-0.5, sensing start time 20-40h and ± 10° randomly varied extension angles similar to Figures 6K–6M, but specifically for the equator region. (B) Simulations for the 'only target' rule and two combinatorial stop rules without (C) and with target (D). Each data point was simulated 100 times for angles that were randomly offset ± 10°.

Supplemental Figure 6 (related to Figure 7)

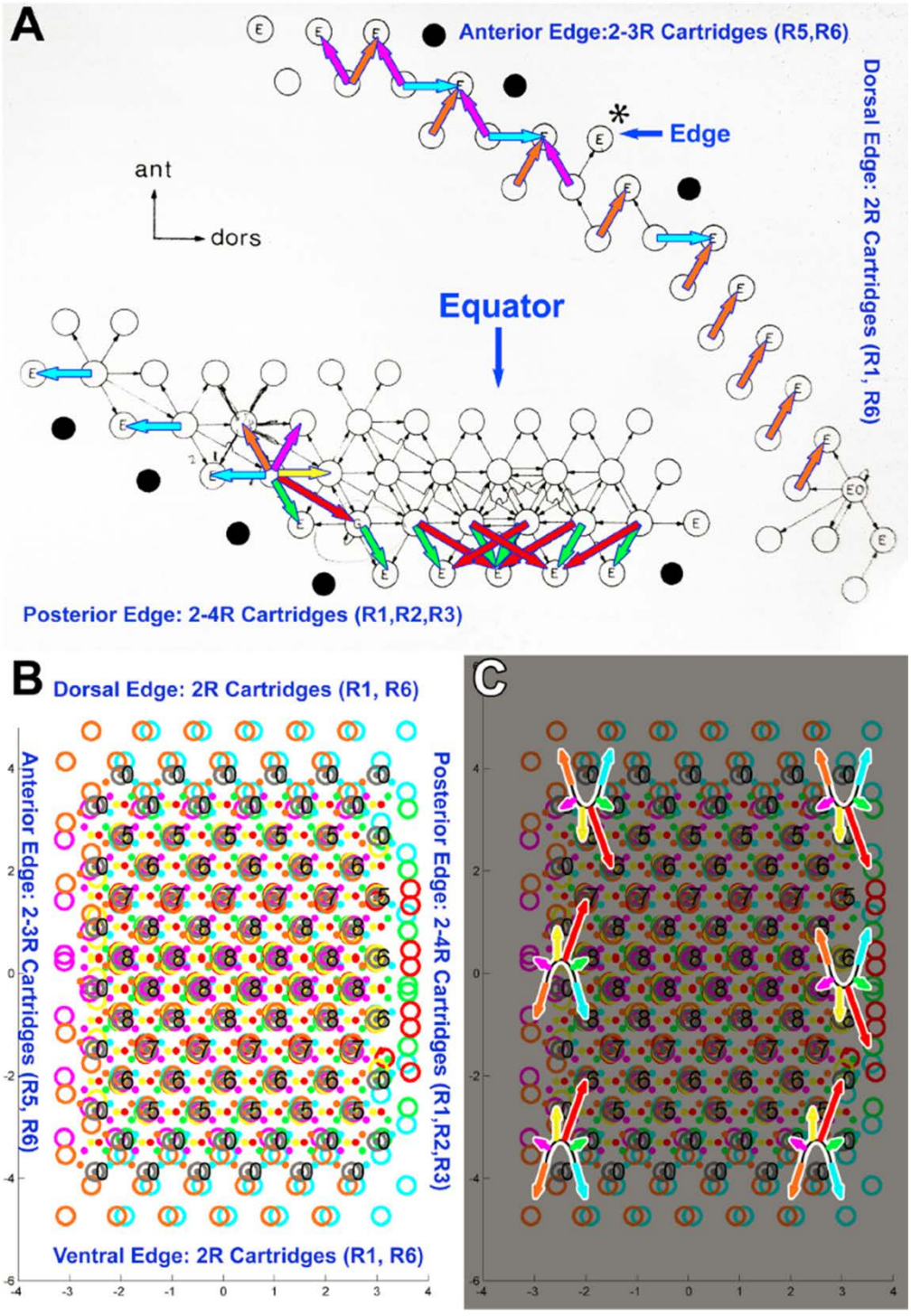

Figure S2 6. Analysis of Edge Cartridges, Related to Figure 2.7

(A) Edge cartridge analysis adapted from Figure 25 of Meinertzhagen and Hanson (1993). The border of the lamina provides, in addition to the equator, a second region of naturally occurring cartridges that do not contain the precise R1–R6 neural superposition wiring. Edge cartridges have been analyzed in detail as reported by Meinertzhagen and Hanson (1993) for individual Musca and Drosophila specimens. Edge cartridges lack an overlying ommatidium in the retina. They receive input from R growth cones from the interior of the lamina and hence contain less than six R terminals. However, the development of edge cartridges is less straight forward than equator cartridges for two reasons: first, the nature of the border of the lamina and its influence on growth cone extension and stop is unclear, whereas at the equator the homogeneous target grid is uninterrupted and no special border conditions apply. Second, edge cartridges are originally innervated by an overlying ommatidial axon bundle from ommatidia in the retina's margin that degenerate prior to eclosion (Wolff and Ready, 1991). The involvement of degenerating axons is only obvious in a small time window around 44h APF (Meinertzhagen and Hanson, 1993). However, occasional marginal R-cells and their innervations survive, causing irregularities in wild-type edge cartridges, as described below. Despite these complications, Meinertzhagen and Hanson (1993) report the following key observations on edge cartridges: First, edge cartridges receive for the most part exactly those R terminal inputs from inside the lamina that neural superposition wiring dictates. Second, similar to the equator region, the edge is a region of decreased wiring robustness, i.e., R growth cone projection errors are observed in wild-type that almost never occur in neural superposition cartridges. (B and C) Simulation of the 3-rule model predicts the observations made in (A). First, the extension of R1–R6 growth cones with constant angles predicts precisely which R front should 'hit the border' of the lamina on all sides. Second, any stop rule that is based on R front interactions is likely to fail in cartridges where number of interacting R fronts vary; at the equator, a higher density of R fronts causes more likely premature stops, whereas at edge cartridges a reduced number of R fronts may permit incorrect extensions, although the unknown role of the border itself confounds precise predictions. Both observations are apparent in a model simulation that includes the edges. Each edge at and away from the equator receives a specific complement of R fronts. Both the dorsal and ventral edge receive exclusively R1 and R6 fronts, leading to 2R edge cartridges (B, C). In contrast, the anterior edge receives exclusively R5 and R6 fronts and the posterior edge receives R1, R2 and R3 with increased density at the equator compared to the main lamina, leading to 2R, 3R and 4R edge cartridges (B, C). These data largely match the observations by Meinertzhagen and Hanson (1993) shown in (A). However, since the lamina has curved edges not all edge cartridges can be precisely predicted. In addition, the simulation reveals how an R front interaction stop rule will lead to errors at the edges. In the example shown the stop rule 'overlap of 5R fronts', causes a failure to stop for all fronts on the dorsal, ventral, and anterior edges (note, the wiring number of ''0'' along the border is due to the fact that no R-cells stopped at the correct cartridge at the end of the simulation). However, since it is unclear how the border of the lamina contributes to the stop rule, we assume that a glial, neuronal or extracellular matrix barrier prevents infinite growth cone extension. The increased error rate at the edges supports a stop rule based on R front interactions in the same way as the increased error rate at the equator:

if only L-cells in the target region served as targets, neither the equator nor the edge cartridges need to exhibit errors, since edge cartridges, like equator cartridges, contain a normal complement of exactly one of each L1-L5 cells (Meinertzhagen and Hanson, 1993).

CHAPTER THREE

Lamina monopolar cells mediate sorting of photoreceptors without acting as targets

3.1 ABSTRACT

Development of neural circuits requires precise matching of pre and post synaptic partners. Synaptic specificity is greatly facilitated by sorting right synaptic partners in close proximity. During this sorting, post-synaptic neurons are regarded as target cues for their pre-synaptic partners. Here we report the surprising finding that, *Drosophila* photoreceptors do not require their post-synaptic partners, lamina monopolar cells (L-cells), as guide posts during their sorting. Six outer photoreceptors (R1-6) in every unit eye arrive first optic neuropil (lamina) in the optic lobe as a bundle and re-sort to their respective synaptic cartridges synchronously with all the other photoreceptors coming from all unit eyes according to the principle of neural superposition. Utilizing intra-vital imaging, we showed that L-cell neurites in the lamina are quite dynamic, extensively overlapping with each other and cover the entire lamina plexus during photoreceptor sorting. When L-cells in a cartridge are ablated, photoreceptor targeting toward that cartridge is fine but the wiring is disrupted in the neighboring cartridges. This result suggests that L-cells play an early role in photoreceptor sorting but not a late role as a target cue. To evaluate the requirement of L-cells at different developmental stages of wiring, we disrupted their membrane dynamics using temperature sensitive dominant negative shibire in a temporally

specific way. We found that L-cell dynamics are indeed not required during photoreceptor extension but before extension starts, to establish an L-cell grid, which organizes photoreceptor intra- and inter-bundle organization and possibly determines extension angles of photoreceptor growth cones. Our data suggest that synaptic partner selection in the fly visual map is achieved through sorting of right partners together independent of post-synaptic neurons acting as a target cue.

3.2 INTRODUCTION

Chemoaffinity hypothesis postulates that every pre and post synaptic neuron pair is specified by a unique molecular tag (Sperry, 1963) which suggests that axons find their correct targets following molecular address codes (Zipursky and Sanes, 2010). Such matchmaking codes have been shown to exist between synaptic partners in the inner plexiform layer of mammalian retina (Krishnaswamy et al., 2015; Matsuoka et al., 2011). However, it is very unlikely that every synapse in the brain is specified with a unique code as expression of these matchmaking codes in pre and post synaptic partners in perfect synchrony at the right time and at the right place would require control mechanisms that are 'hard to imagine' (Zipursky and Sanes, 2010). In addition, perfect matching of every single neuron pair would not allow for variability which is a common feature of neurons and neural circuits (Hassan and Hiesinger, 2015). Therefore there must be additional mechanisms that would lead to synaptic specificity.

There is accumulating evidence that suggests there are 'target-independent wiring mechanisms' that would ensure synaptic specificity by sorting right synaptic partners into close spatial vicinity (Petrovic and Schmucker, 2015). In the mouse olfactory system, sorting of olfactory sensory neurons way before they reach their respective target regions ensures correct topographic map formation (Imai et al., 2009). Also in the *Drosophila* visual system, molecules that have been thought to be guidance cues turned out to be not acting as matchmaking codes that specify a certain target layer for incoming axons but rather provide adhesion between pre and post synaptic axons in a non-discriminative way (Akin and Zipursky, 2016; Ozel et al.,

2015). Also in our previous work, we computationally showed that *Drosophila* R1-6 photoreceptors form the visual map through a developmental algorithm where they may not need any guidance signal from their post-synaptic partners; lamina monopolar cells (L-cells) (Langen et al., 2015). In this chapter, I experimentally tested whether L-cells play any role in guiding photoreceptors to stop at their correct synaptic cartridges to ensure a correct visual map formation.

Every L-cell column is comprised of 5 L-cells (L1-5) and their cell bodies are placed right above the lamina plexus to where they extend their primary neurites (Meinertzhagen and Hanson, 1993). Photoreceptors make tetrad synapses with four post-synaptic neurons; invariably with L1 and L2 (main post-synaptic partners), and variably a pair of L3, lamina amacrine or glial cells (Meinertzhagen and O'Neil, 1991).

During visual map formation lamina cell development is strictly dependent on the development of photoreceptors; if the eye formation is disrupted, this will cause the loss of lamina (Selleck et al., 1992; Selleck and Steller, 1991; Steller et al., 1987). If photoreceptor innervation in the optic lobe is prevented, proliferating lamina precursor cells, which produce lamina neurons, are absent in the optic lobe (Selleck and Steller, 1991) and photoreceptor innervation controls this by inducing the transition of precursors cells from G1 phase to S phase (Selleck et al., 1992).

Dependence of target cell development on arrival of photoreceptors ensures a one to one correspondence between the number of ommatidia in the retina and the number of synaptic cartridges in the lamina (Huang and Kunes, 1998). It is a clever strategy for the photoreceptors to

initiate the differentiation of their target cells such that this would preserve the topography of the visual map. However, photoreceptors do not make synapses with the lamina cells of the cartridges where they initially arrive at; instead photoreceptors project to neighboring cartridges in accordance with neural superposition which was explained in detail in chapter 1 and 2 (Braitenberg, 1967; Kirschfeld, 1967).

During neural superposition establishment, function of N-cadherin (CadN), which is a cell adhesion molecule that belongs to classical cadherin family (Yagi and Takeichi, 2000), has been shown to be required in R1-6 photoreceptors and also in L-cells for correct photoreceptor targeting (Lee et al., 2001; Prakash et al., 2005). Also it has been shown that *CadN* is required for R7 targeting in the medulla of *Drosophila* optic lobe (Lee et al., 2001; Ting et al., 2005). However, by using ex-vivo live-imaging, it has been shown by our group that *CadN* mutant R7 photoreceptors can target to their respective final layer like wild type R7s but cannot adhere there so retract back, which might be mistakenly regarded as a targeting defect in fixed images (Ozel et al., 2015). This raises the question whether R1-6 photoreceptors can also target correctly but cannot adhere to their correct target regions when they or L-cells lack CadN.

In this part of my thesis, I presented data that suggest L-cells are not required for photoreceptor targeting but scaffold formation which is a prerequisite of correct visual map formation. Ablation of L-cells in a cartridge leads to wiring defects in the neighboring cartridges but not the cartridge itself. With temporally specific perturbation experiments where I blocked endocytosis in L-cells at different developmental stages of visual map formation, I found that L-cells are specifically required during scaffold formation. Since scaffold formation dictates the

extension angles of photoreceptor growth cones, this result suggests that L-cells play a role in determining the extension angles of photoreceptor growth cones which would explain why in ablation experiments neighboring cartridges have more wiring defects. Furthermore, I showed that CadN function in L-cells has a late phenotype, probably after photoreceptor targeting is done. My data suggest that L-cells are required for final wiring pattern by organizing the target field and not by acting as attractive guide posts.

3.3 RESULTS

3.3.1 Lamina cells form a filopodial mesh that covers the entire lamina plexus throughout sorting period

Adult synaptic cartridge organization has been studied at the EM level (Meinertzhagen and O'Neil, 1991; Meinertzhagen et al., 2000) and cell type composition and the network of synaptic connections in one cartridge has been determined (Rivera-Alba et al., 2011). These EM studies showed the final placement of photoreceptor R1-6 cells and their post-synaptic partners, L-cells, in the cartridge. However, to attain this final placement, L-cells should go through an organizational change as they form a single fascicle at the beginning of the lateral sorting of photoreceptors (Schwabe et al., 2014). How single L-cell neurites change their positions in the cartridge during development of the visual map was shown by Schwabe and colleagues (Schwabe et al., 2014). They labelled individual L-cells by using mosaic analysis with a repressible cell marker (MARCM) (Lee and Luo, 1999) and they found that as photoreceptors approach towards their target cartridges, they encircle L1-2 neurites and separate them from L3-5 neurites. However, in none of these studies dynamics of L-cell neurites during photoreceptor targeting were investigated. I reasoned that live observation of dynamics and positioning of L-cell neurites during photoreceptor targeting would give valuable information about the underlying role of L-cells in sorting of photoreceptors by revealing the constraints on the

interaction of photoreceptors with L-cells and this would help me answer the question of whether L-cells can guide photoreceptors to stop at their correct target cartridges.

Utilizing the 2-photon technique that I developed, I visualized the development of visual map formation in an intact pupae for over 24 hours where I labelled all L-cells with a membrane bound GFP tag (Han et al., 2011) and all photoreceptors with a membrane bound tomato fluorescent protein (FP) tag (gift from Larry Zipursky) (Figure 3.1A-I). L-cell bodies are localized right above the lamina plexus where photoreceptor sorting happens (Figure 3.1A). We have previously shown that photoreceptor axons get shorter in a temporal wave during sorting and this shortening causes the lamina plexus to rotate 90° underneath the eye and also to get straighten out and become parallel to the eye (Langen et al., 2015). I observed the same two major movements when all L cells were genetically labelled as well (Figure 3.1A-I). L-cell neurites in the lamina plexus rotated together with the photoreceptor terminals while terminals of both cell types were getting closer to the eye. Different than the photoreceptors, L-cell bodies located above the lamina plexus also rotated and the whole cell body layer got parallel to the eye (Figure 3.1C). This suggests that, photoreceptor axon shortening causes the entire lamina layer to rotate and L-cell neurites remain closely associated with photoreceptor terminals. Rotation of the L-cell bodies did not re-organize photoreceptor bundles passing through the L-cell body layer as the relative positions of photoreceptor bundles at different depths of L-cell body layer remained the same at different time points during sorting (Figure S3.1A). Interestingly, organization of photoreceptor bundles varies between different depths of the L-cell body layer: at the top of the L-cell body layer, photoreceptor inter-bundle organization seems random whereas at the lamina

plexus, bundle distances become regular (Figure S3.1B). This data suggests a role for L-cells to organize photoreceptor inter-bundle spacing.

Photoreceptor growth cones sort to their targets laterally between two glial sheets, in a 2D plane (Langen et al. 2015; Meinertzhagen and Hanson, 1993). I reasoned that if the L-cells guide photoreceptor growth cones to stop at their correct target cartridges, L-cell neurites should be positioned at the same 2D plane as photoreceptor growth cones. Side view of the lamina plexus at different developmental stages of sorting revealed that photoreceptor growth cones and L-cell neurites indeed co-localized at the same level in lamina plexus (Figure 3.2). This co-localization was even more obvious at the single photoreceptor level; I stochastically labelled photoreceptor growth cones with GFP and L-cells with Tomato FP (Han et al., 2011; Rintelen et al., 2001) and visualize the development in live. After determining the types of growth cones from their final morphologies and elongation angles, I color coded every single subtype as in Chapter 2 (Langen et al., 2015). Side view of the lamina plexus shows how every photoreceptor growth cone subtype elongates at the same physical level with L-cell neurites (Figure S3.2A-C).

How are photoreceptor growth cones and L-cell neurites positioned in the xy plane of the lamina plexus? Cross sections of the lamina plexus along dotted lines in the side view pictures show that L-cell neurites are very dynamic (Figure 3.2); they initially start to expand along dorso-ventral axis with many projections covering the entire lamina plexus. In the middle of the sorting period, neighboring L-cell neurites are in contact with each other, possibly overlapping. Towards the end of the sorting period, L-cell neurites start to shrink and are encircled by arriving photoreceptor terminals. Then, L-cells start to extend their processes in between the

photoreceptor terminals to start synaptogenesis. With the extended processes, L-cell neurites look like stars. As L-cell neurites cover the entire lamina plexus and possibly overlap with each other for most of the sorting period, I wanted to determine whether photoreceptor growth cones make any contact with an L-cell neurite group in the wrong target cartridge during their elongation (Langen et al., 2015). When all photoreceptors and L-cells are labelled, the overlap is obvious but I needed to tackle this question at the single cell level (Figure S3.2A-C). I stochastically labelled photoreceptors with GFP while labelling all L-cells with tomato FP. I segmented all different subtypes of R1-6 photoreceptor growth cones at different time points during sorting. The signaling sequence of the tomato FP construct is not as efficient to go to thin processes as CD4 tagged GFP (Han et al., 2011), so that in these pictures processes extending from the L-cells in the lamina plexus seem less dense which makes L-cell neurites look quite small. However, even with this small area coverage, photoreceptors make incorrect contacts with L-cells in wrong cartridges (Figure S3.2A). This fact makes L-cells poor targets for photoreceptors because photoreceptors need to be able to distinguish the right target among the wrong choices while being in contact with many of them at the same time. We have previously computationally shown that it is possible that L-cells may not be required as targets for photoreceptors at all (Langen et al., 2015) (Chapter 2). So I wanted test this possibility experimentally.

3.3.2 Killing all L-cells in one cartridge disrupts the wiring pattern in the neighboring cartridges but the cartridge itself

To test the requirement of L-cells for photoreceptor sorting, one trivial experiment is to kill them and ask whether the final wiring pattern is disrupted or not. Ectopic induction of apoptosis by expressing pro-apoptotic genes is a way to selectively ablate cells (Wing et al., 1998). *Head involution defective (hid)* gene is a regulator of programmed cell death and ectopic expression in the *Drosophila* retina causes loss of eye (Grether et al., 1995). Therefore, L-cells can be killed by ectopic overexpression of Hid with an L-cell specific driver. The ideal experiment would be to kill all L-cells only in one cartridge but not the others and observe the photoreceptor targeting to this cartridge that is devoid of L-cells (Figure 3.3A). However, to ablate all L-cells only in one cartridge is technically very hard, if not impossible, with the existing expression systems in *Drosophila* (del Valle Rodriguez et al., 2011) so I designed ablation experiments with a general L-cell specific Gal4 driver, 9B08-Gal4 (Pecot et al., 2014). These ablation experiments are performed by Charlotte Wit, another graduate student in Hiesinger lab. Fortuitously, when we expressed Hid specifically in L-cells, we got a sparse ablation pattern where a few of the cartridges were completely devoid of L-cells in adult lamina (Figure 3.3B,C). This is due to the fact that it is very hard to kill post-mitotic neurons as they are to serve in neural circuitry for the lifetime of the organism (Kole et al., 2013). Surprisingly, when we scored the number of terminals in these few cartridges we found that most of them had 6 terminals as in WT which would suggest L-cells are not required for targeting of photoreceptors (Figure 3.3C,D). But puzzlingly, in the neighboring cartridges, which still had some L-cells, we

found wiring defects which would suggest a requirement of L-cells for targeting (Figure 3.3C,D). As we did not have temporal control on when to ablate L-cells, they might have got killed in different cartridges at different developmental stages, for example during scaffolding (Chapter 2) or during photoreceptor extension. If L-cells are required during scaffolding before photoreceptor extension, their ablation in one cartridge would affect the scaffold formation and this might cause a change in extension angles of photoreceptors that extend away from this cartridge. Change in extension angles would cause photoreceptors to target wrong neighboring cartridges whereas targeting to the cartridge with no L-cells would still be fine as the extension angles of photoreceptors coming from cartridges with L-cells would not be affected. To test this idea, we did the same experiment, i.e. ablated L-cells, and checked the structure of the scaffold around the time photoreceptors started extending, at 25% pupal development (which corresponds to 25 hours after puparium formation (hAPF) at 25°C). When all the L-cells in one cartridge were missing, bundle organization of the photoreceptors that were coming from the same ommatidium became circular instead of crescent organization (Figure 3.3F). Since the extension angles of photoreceptors are determined in the bundle (Chen and Clandinin, 2008), our data suggest that crescent to circular bundle change may alter the projection directions of photoreceptors which will cause miswiring in the neighboring cartridges (Figure 3.3G). Implication of this result is that L-cells are required during scaffold formation but not during photoreceptor extension. To test the requirement of L-cells at different stages of development of visual map formation, I utilized a method which allowed me to do temporally specific perturbation experiments.

3.3.3 L cell membrane dynamics are not required during targeting but scaffolding

Testing the requirement of cells for a process at different stages demands temporally specific ablation experiments. Toxic genes can be expressed in a temporally specific manner in the cell group that is wanted to be ablated. In *Drosophila*, by using temperature sensitive proteins temporal specificity can be achieved. For example, a temperature sensitive suppressor of GAL4, GAL 80^{ts}, is used to inhibit the expression of GAL4 and GAL4-driven transgenes (del Valle Rodriguez et al., 2011). At permissive temperatures, GAL80 inhibits the expression of GAL4 and the transgene, whereas at restrictive temperatures, inhibition is relieved which means that shifting temperatures gives temporal control on the expression of transgenes. Although using $GAL80^{ts}$ allows a high degree of temporal control (del Valle Rodriguez et al., 2011), expression of the transgene and the amount of time that it would take to ablate cells create a bottleneck for tight temporal control. In addition, to test requirement of cells during a developmental stage that is preceding other stages, cells should be put back in place during the succeeding stages not to confound the final phenotype. This is impossible. The ideal method to somehow take the cells out of the play should be temporally specific, fast and also reversible and to my knowledge that kind of a method does not exist. I reasoned that the closest I could get is by blocking the membrane dynamics of L-cells for two main reasons. First, by blocking membrane dynamics, all the filopodial extensions and retractions would be blocked, so the interaction of L-cells with their environment would be diminished. Secondly, trafficking of any signaling protein that might be required for L-cells' function in wiring would be disturbed; this is in line with the finding that turnover of guidance proteins in photoreceptors is required for correct wiring (Williamson et al.,

2010). To block the membrane trafficking, I utilized a temperature sensitive dominant negative form of *shibire*, which is the *Drosophila* homolog of *dynamin* (Gonzalez-Bellido et al., 2009). *shibire* is required for fission of invaginated membrane during endocytosis (Kroll et al., 2015). Temperature sensitive dominant negative *shibire* functions as wild type at permissive temperatures (in this study it is 22°C), however, it acts as dominant negative at restrictive temperatures (in this study it is 31°C) (Gonzalez-Bellido et al., 2009) and blocks endocytosis. Since at permissive temperature dominant negative form of shibire protein is readily expressed, as soon as the temperature is shifted to restrictive level, endocytosis is blocked (Luo et al., 2008), which is very important for a tight temporal control. In addition, effect of mutant shibire is reversible: when shifted to permissive temperatures, dominant negative mutant protein goes back to function like wild type so the block on endocytosis is released almost instantaneously (Luo et al., 2008).

As proof of principle, I expressed temperature sensitive mutant shibire and CD4-GFP in all L-cells and I visualized the dynamics of L-cell neurites in live at restrictive temperature (31°C) between 20-45 hAPF (Figure 3.4). In the control animals I only expressed CD4-GFP. To keep the temperature constant at 31°C throughout imaging period, I used a heater unit with a temperature controller and all the imaging was done in a closed chamber. In the experimental animals, L-cells lost most of their filopodial extensions, and they failed to cover the entire lamina plexus in contrast to control animals. Eventually they acquired a blob shape instead of a star shape. This suggested that membrane dynamics of L-cells can be manipulated by expression of temperature sensitive mutant shibire. Next, I disrupted membrane dynamics of L-cells

specifically during either 1) scaffold formation (10-20 hAPF), or 2) photoreceptor targeting (between 20-45 hAPF) (Figure 3.5). To test the requirement for L-cell membrane dynamics during scaffolding, I blocked endocytosis in L-cells between 10-20 hAPF which is before lateral sorting of photoreceptors start; to test the requirement for L-cell membrane dynamics during lateral photoreceptor sorting I blocked endocytosis in L-cells between 20-45 hAPF. I scored the number of cartridges with different number of terminals in the adult lamina as a measure of correct wiring. Interestingly, when the L-cell membrane dynamics were blocked during lateral sorting, most of the adult lamina cartridges had 6 terminals as in wild type (Figure 3.5 A,B). To eliminate the possibility of L-cells catching up with the normal development once the block was released, I dissected the brains of experimental and control animals immediately after the block ended at 45 hAPF, instead of looking at adult cartridges. Although in the experimental animals L-cell neurites completely lost their wild type morphology, number of photoreceptor terminals at the cartridges was like in control animals (Figure 3.5D). These data suggest that L-cell dynamics do not play a role during photoreceptor lateral sorting. However, blocking membrane dynamics of L-cells during scaffolding completely messed up the lamina cartridge organization suggesting that L-cell membrane dynamics are required during scaffolding (Figure 3.5A,C). This result is consistent with the fact that when L-cells are completely ablated, photoreceptor bundle organization gets disrupted before lateral sorting starts (Figure 3.3F), and this might cause a change in elongation angles of photoreceptor growth cones which would end up targeting to wrong cartridges (Figure 3.3E). In conclusion, these data suggest a role for L-cells to ensure correct establishment of the scaffold which is a prerequisite of correct targeting of photoreceptor growth cones. However, L-cells do not act as target cues during photoreceptor extension.

3.3.4 N-Cadherin function in L-cells has a late role in photoreceptor targeting

Logically, if L-cells are not required during lateral sorting of photoreceptors, any molecule in L-cells should not be required for this process either. However, Tom Clandinin's work previously showed that function of *CadN* (N-cadherin) in L-cells in the target cartridges of photoreceptors but not in the origination cartridges, is required for correct targeting of photoreceptors (Prakash et al., 2005). How can we explain this discrepancy?

One possible explanation is that if CadN is required in the target areas, photoreceptors might still have access to CadN from other sources once the L-cells are killed and cleared. If this is not true, when we kill all L-cells in one cartridge and label the brain for CadN, we should expect to see a hole where the L-cells are missing. When we did this experiment we saw that although L-cells were completely vanished from some cartridges, CadN was still there (Figure S3.3). Indeed, CadN is expressed also in photoreceptor growth cones and required for correct targeting (Lee et al., 2001). This result suggests that even in the absence of L-cells, photoreceptors have access to N-cadherin from other cells, possibly from other photoreceptors.

Another possible explanation is that since correct scaffold formation is a prerequisite of correct photoreceptor targeting, CadN function in L-cells might be required for correct scaffold establishment. To test this hypothesis, I knocked down CadN in L-cells by expressing *CadN* RNAi with GCM-Gal4 driver which drives expression in L-cells (Schwabe et al., 2014; Ting et al., 2005) (Figure 3.6). To assess the formation of a correct scaffold, I measured the distances between future target areas in the laminas of pupae at 25 hAPF, which is around the time

photoreceptor sorting starts (Figure 3.6A-C). I found that there was no significant difference between control and *CadN* knocked down scaffolds, suggesting CadN function in L-cells has no role in scaffold formation (Figure 3.6C). This finding is in accordance with a previous observation of Schwabe and colleagues where they showed that when L-cells are missing CadN, directionalities of the R1-6 photoreceptor growth cones at 28 hAPF are not disrupted, which implies that scaffold is not disrupted (Schwabe et al., 2013). Also, Prakash et.al. showed that CadN function is required in the target cartridge of photoreceptors, not in their origination cartridges (Prakash et al., 2005) which is again in line with my result.

Schwabe and colleagues also showed that CadN function in L-cells has a late role in cartridge formation which is different than the targeting role Prakash et.al. had shown (Schwabe et al., 2014): according to differential adhesion hypothesis, less adhesive cells surround more adhesive cells (Duguay et al., 2003; Schwabe et al., 2014). Schwabe et.al. tested whether this is the reason why L-cells are surrounded by photoreceptor terminals in the final cartridge organization. First, they showed that CadN expression in L-cells is more than it is in photoreceptor growth cones. Then, by knocking down CadN in L-cells, they shifted this difference in favor of photoreceptors and showed that photoreceptor terminals invaded the center of the cartridge while the L-cell neurites stayed at the periphery. However, neither Prakash et.al. nor Schwabe et.al. showed when the targeting or cartridge organization defects arose during development. I hypothesized that when L-cells are devoid of CadN, photoreceptors can still target normally and both of the aforementioned defects occur at a late stage of photoreceptor lateral sorting. Since in both of the aforementioned studies phenotypes were scored in fixed

images which were taken after photoreceptor targeting was done, authors might have missed this possibility. First I replicated the cartridge organization defect (Schwabe et al., 2014); when I knocked down CadN in L-cells, at 50 hAPF cartridges collapsed and they lost the hole in the center where typically L-cell neurites sit (Figure 3.6D). Next, I expressed CD4-Tomato in all photoreceptors and image them live during the targeting period while in the same animals I knocked down *CadN* in L-cells (Figure 3.7). The structure of the lamina was like wild type until around 35 hAPF, which is very close to the end of targeting period. The defects in cartridge and overall lamina organization started to occur around 37-38 hAPF and became apparent at 41 hAPF. By 44 hAPF, most of the cartridges lost the hole in the middle and collapsed. In addition, at this time point some of the cartridges fused with each other. In a fixed preparation, this would definitely seem as a targeting defect although it is a defect that arises after targeting is completed. This result suggests that function of CadN in L-cells causes a late stage defect in photoreceptor sorting without possibly affecting the ability of photoreceptors to target normally. Indeed, in a similar model, *CadN* mutant R7 photoreceptors had been previously shown to have targeting defects in the medulla which suggested CadN functioned as a guidance molecule (Ting et al., 2005). However, work from our lab showed that *CadN* mutant R7 photoreceptors could target normally to their respective layer in the medulla but retracted due to the fact that they could not adhere to their correct layer without CadN. This might be the case also in the lamina; when L-cells lose CadN, photoreceptors can still target normally but because they cannot adhere to the L-cells in the correct target region, they adhere to other sources of CadN which is seen as wiring defects in adult animals. Best way to test this idea is observing dynamics of individual WT photoreceptor growth cones when all L-cells lack N-Cadherin. This experiment would give a

definitive answer whether photoreceptors have targeting defects or adhesion defects when L-cell lack N-Cadherin.

3.4 DISCUSSION

3.4.1 L-cells are not required for targeting but scaffolding

The data I presented in this chapter suggest that L-cells do play a role in the sorting of photoreceptors to their correct target regions in a rather unconventional way: instead of acting as a target cue to guide photoreceptors, L-cells ensure the establishment of correct scaffold which ensures correct extension angles of photoreceptors resulting in correct visual map formation (Langen et al., 2015; Schwabe et al., 2013). In other words, once the extension angles are correctly set, photoreceptors do not rely on L-cells for further targeting. This makes sense when we think about the area coverage of L-cell neurites in the lamina plexus, which makes them very poor targets for photoreceptors: as photoreceptors make multiple contacts with L-cell neurites in the wrong cartridges, it is hard to think of a mechanism where photoreceptors can distinguish right target from a wrong one. Expressing unique molecular tags in L-cells at different cartridges might sound like a solution for this problem. However, any mechanism that will ensure to express different tags in L-cells, should also ensure at the same time that matching molecules should be expressed in the pre-synaptic photoreceptors as well. For example, fly Dscam1 protein, which is a cell adhesion molecule of immunoglobulin superfamily has been suggested to

'contribute to specificity of neuronal connections' (Schmucker et al., 2000). Alternative splicing of *Drosophila Dscam 1* creates thousands of splice variants, each encoding a protein with a different ectodomain and each protein shows isoform-specific binding (Wojtowicz et al., 2004; Wojtowicz et al., 2007). As this might be seen as the perfect candidate for a specificity code, it has been further shown that these homophilic interactions on the dendritic branches of the same cell are repulsive (Hughes et al., 2007; Matthews et al., 2007; Soba et al., 2007) and mediates neuronal self-avoidance. Most importantly, splicing of *Dscam1* is probabilistic such that probability of neighboring cells expressing the same type of isoforms is very low and this gives each cell a unique identity in a very robust way (Miura et al., 2013). Even if the homophilic interactions were attractive, stochastic expression of different protein variants in different cells makes it impossible to use it as a matchmaking code between two neuronal groups as this would result in unique visual maps in different animals which is not the case. In the case of fly visual system, Dscam 1 function in L-cells has been shown to be not required for normal visual circuitry (Millard et al., 2010).

I showed that L-cells are required during scaffold formation which is required for correct wiring. For a correct scaffold three things has to be established properly: 1) Distances between target areas, 2) Photoreceptor inter-bundle spacing and 3) Photoreceptor inter-bundle organization. How can L-cells mediate these? L-cell neurites sit at the future target areas of photoreceptors. If L-cells from different columns can tile the lamina plexus, this would result in a regular spacing of L-cell neurites. This can be envisioned like many repelling identical magnets; on a flat surface, balance between repulsion from all neighboring magnets will cause

the magnets to space uniformly. Indeed, it has been shown that *Dscam 2*, another cell adhesion molecule, mediates homophilic, repulsive interactions between L1 projections in the medulla which ensure L1s invade one and only one medulla column, i.e. tile the medulla space (Millard et al., 2007). This tiling function has been shown to exist to some extent also in the lamina; when the L1s are mutant for *Dscam2*, cartridge organization is disrupted with many fused cartridges (Millard et al., 2010). In other words, by proper tiling which can be mediated by only one protein, L-cells can organize target area. If L-cells tile uniformly, since every photoreceptor bundle is associated with a lamina column (Meinertzhagen and Hanson, 1993), this will ensure regular inter-bundle spacing. Indeed it has been shown that if the L-cells cannot form lamina columns, organization of photoreceptor bundles in the lamina gets disrupted (Umetsu et al., 2006) and for correct lamina column formation, interaction of L-cells and photoreceptors through Hibris and Roughest, which are two cell adhesion molecules, is required (Sugie et al., 2010). My data suggest that L-cells physically open up a photoreceptor bundle to give it a crescent shape. However, the exact nature of this organizational change should be investigated further.

3.4.2 CadN does not function as a guidance cue for photoreceptor targeting

CadN has been shown to be required in both photoreceptors and L-cells for correct wiring (Lee et al., 2001; Prakash et al., 2005). Furthermore, it has been shown that for a photoreceptor to target correctly, CadN function is required in L-cells that are in the target cartridge but not in the origination cartridge of this photoreceptor (Prakash et al., 2005). This is consistent with our finding that CadN in L-cells is not required for scaffold formation but is contradictory with our

results from ablation and temperature sensitive *shibire* experiments which showed L-cells are not required as targets. One possible explanation for this discrepancy is that without CadN in L-cells or photoreceptors, photoreceptors can still target correctly and reach their respective target cartridges but fail to adhere which would cause them to retract. In the case of CadN mutant photoreceptors, almost all observed targeting defects were that photoreceptors either couldn't extend or they partially extend toward their correct target cartridge (Lee et al., 2001; Schwabe et al., 2013). Since in fixed images retracted photoreceptors cannot be distinguished from the ones that cannot extend at all or that are partially extended, previous studies may have mistakenly label these phenotypes as targeting defects. In the case of CadN mutant L-cells, since photoreceptors can still adhere via CadN, after targeting correctly and failing to adhere, they may retract back or adhere to another source of CadN. The live imaging data of photoreceptors in the background of CadN deficient L-cells showed that targeting defects do not arise until almost the end of targeting period which supports the idea that photoreceptors can target normally but cannot adhere at the correct target region. Then how can photoreceptors adhere at the right cartridge when there are no L-cells? Our data showed there was still CadN in the cartridges where there were no L-cells. This result is not surprising since we know photoreceptors express CadN, too. So the incoming photoreceptors might adhere to other photoreceptors that are projecting from different bundles to the same cartridge. Knowing that CadN is mainly localized at the filopodial tips of photoreceptor growth cones (Schwabe et al., 2013), this is in line with the idea that interactions of photoreceptor growth cone fronts mediate them to stop at the correct target areas (Langen et al., 2015).

In conclusion, our data shows a surprising role for post-synaptic neurons to ensure synaptic partner sorting without acting as a target cue in the *Drosophila* visual map formation.

3.5 CHAPTER THREE FIGURES

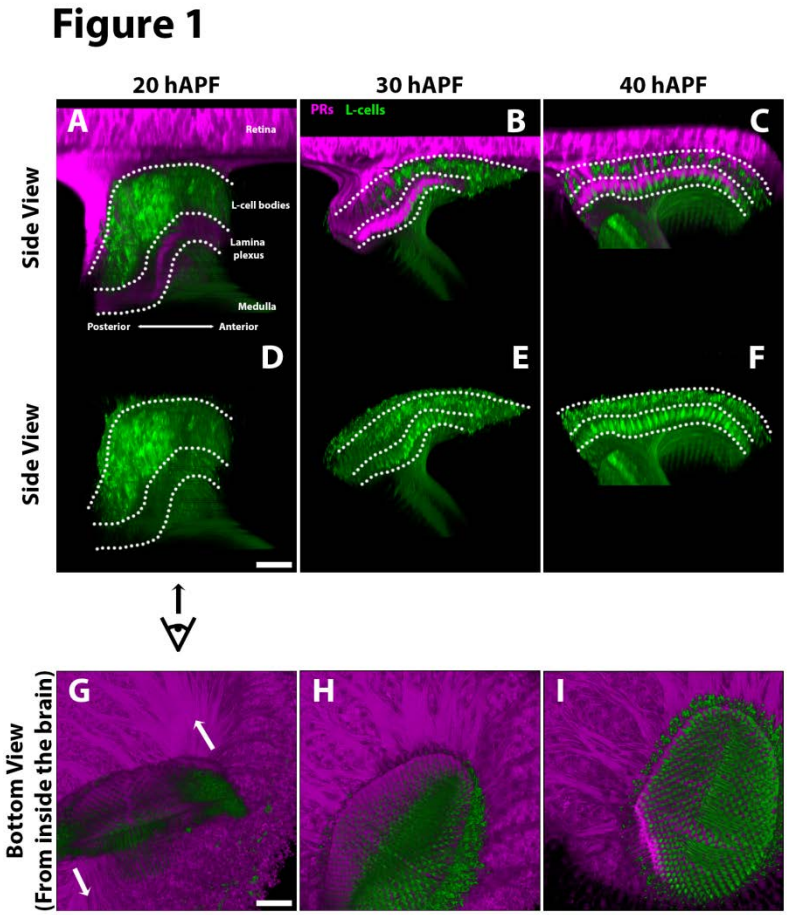

Figure 3 1. Intravital imaging reveals the close association of L-cell cell bodies and terminals with photoreceptor axons and terminals

(A) Side view of eye-lamina complex at the beginning of photoreceptor sorting. Photoreceptors are in magenta, L-cells are in green. (B,C) View of the same specimen in 10 hr increments. Terminals of both photoreceptors and L-cells in the lamina get straighten out and become parallel to the eye at the end of the sorting period. (D-F) Only L-cells of the same specimen in (A-C) are shown. (G-I) View of the same specimen from inside the brain in 10hr increments. The whole lamina plexus rotates in the direction of the arrows.

Figure 2

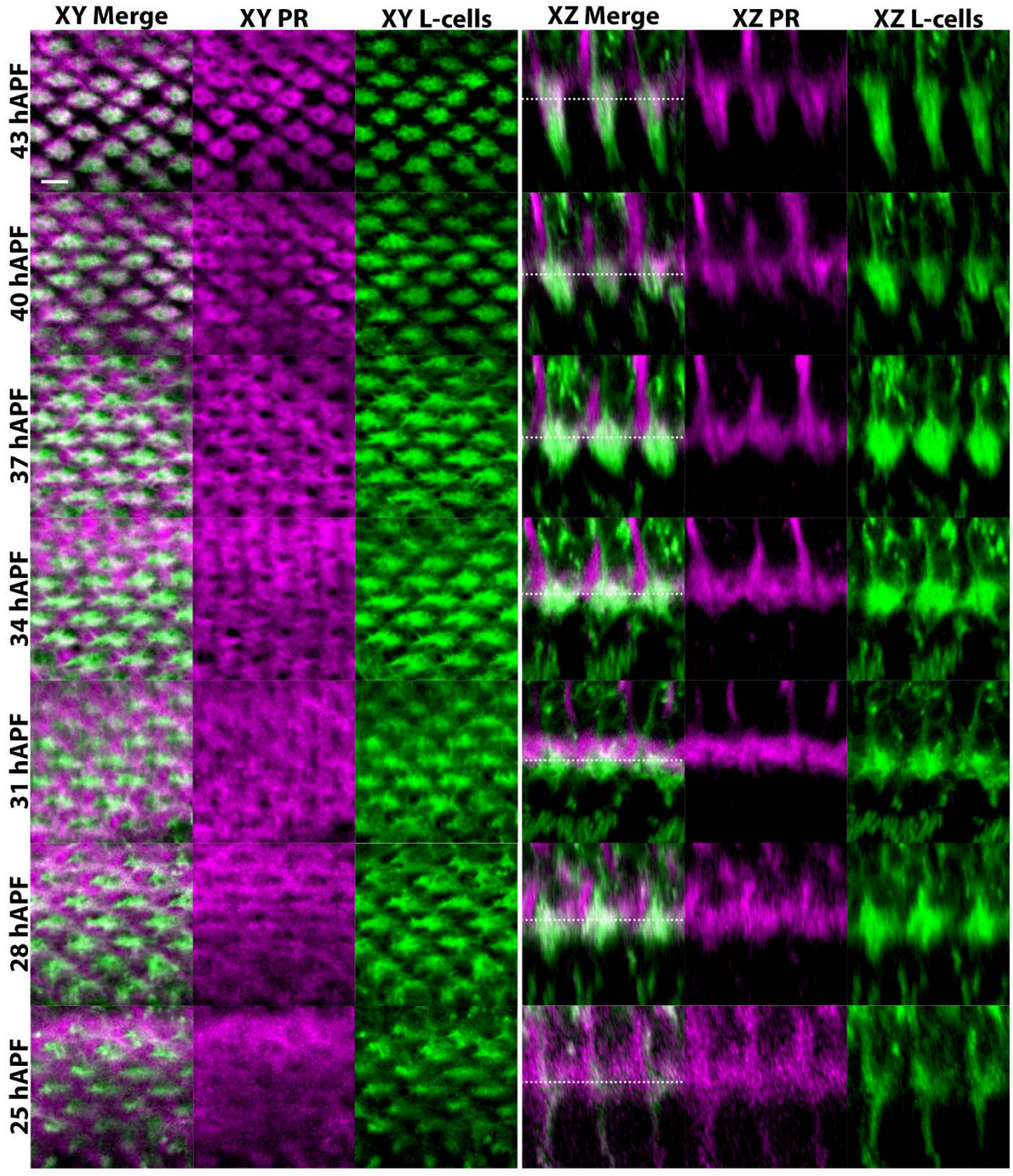
XY Merge
XY PR
XY L-cells
XZ Merge
XZ PR
XZ L-cells
43 hAPF
40 hAPF
37 hAPF
34 hAPF
31 hAPF
28 hAPF
25 hAPF

Figure 3 2. Photoreceptor growth cones and L-cell neurites are positioned at the same 2D plane in lamina plexus.

(Left three panels) Cross section (top view) of lamina plexus at different developmental time points. Photoreceptors (PR) are in magenta, L-cells are in green. (Right three panels) Side view of the lamina from the same specimen at different developmental time points. Dotted lines show where the cross sections in the left panels were taken.

Figure 3

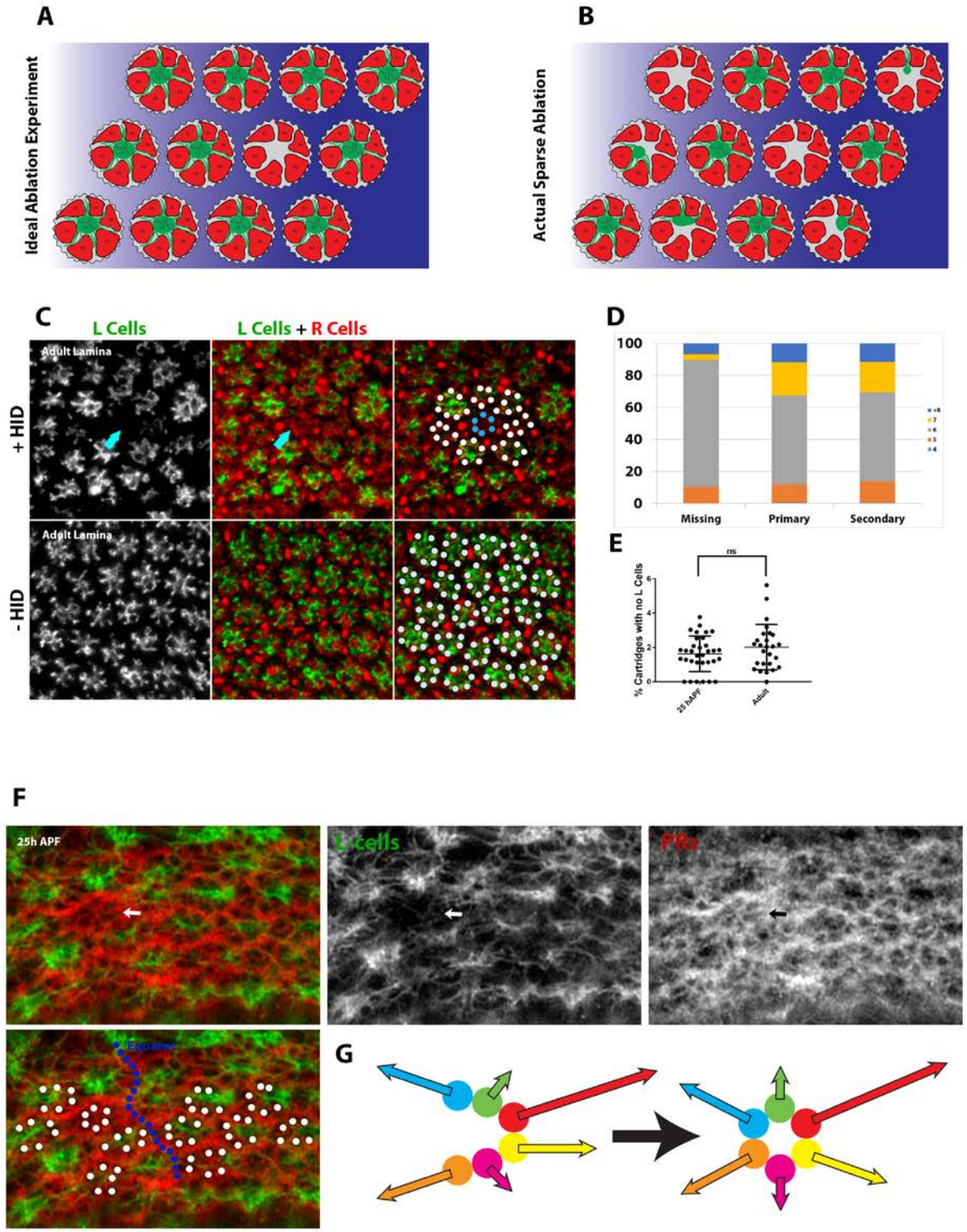
A
Ideal Ablation Experiment
B
Actual Sparse Ablation
C
L Cells
L Cells + R Cells
Adult Lamina
+ HID
Adult Lamina
- HID
D
100
80
60
40
20
0
Missing
Primary
Secondary
E
ns
% Cartridges with no L Cells
25 hAPF
Adult
F
25h APF
L cells
PRs
Equator
G

Figure 3 3. Killing all L-cells in one cartridge disrupts the wiring pattern in the neighboring cartridges but the cartridge itself

(A) Schematic of adult lamina after an ideal ablation experiment. In an ideal ablation experiment only one cartridge is devoid of all L-cells. (B) Schematic of adult lamina after an actual ablation experiment. Some cartridges lack all L-cells, some cartridges lack some, some cartridges retain all the L-cells. (C) (Top three panels) Adult lamina after ectopic Hid expression in L-cells. L-cells are in green, photoreceptor terminals are in red. Cyan arrow shows a cartridge that has no L-cells. Marking the terminals in cartridges reveals that neighboring cartridges show miswiring defects. (Lower three panels) Control experiment where Hid was not expressed. (D) Percentages of cartridges with different number of photoreceptor terminals. Cartridges that have no L-cells show less frequent miswiring defects than their primary and secondary neighbors. n>29 (E) Percentages of cartridges with no L-cells at 25 hAPF and adult laminae. n>37, unpaired t-test (F) Lamina at 25 hAPF after ectopic Hid expression in L-cells. Photoreceptors (PRs) are in red, L-cells are in green. Arrows show a cartridge area that has no L-cells. Photoreceptor heel organization is circular when there are no L-cells in the cartridge. (G) Schematic of the change in photoreceptor heel organization when L-cells are lost in one cartridge at the beginning of sorting.

Figure 4

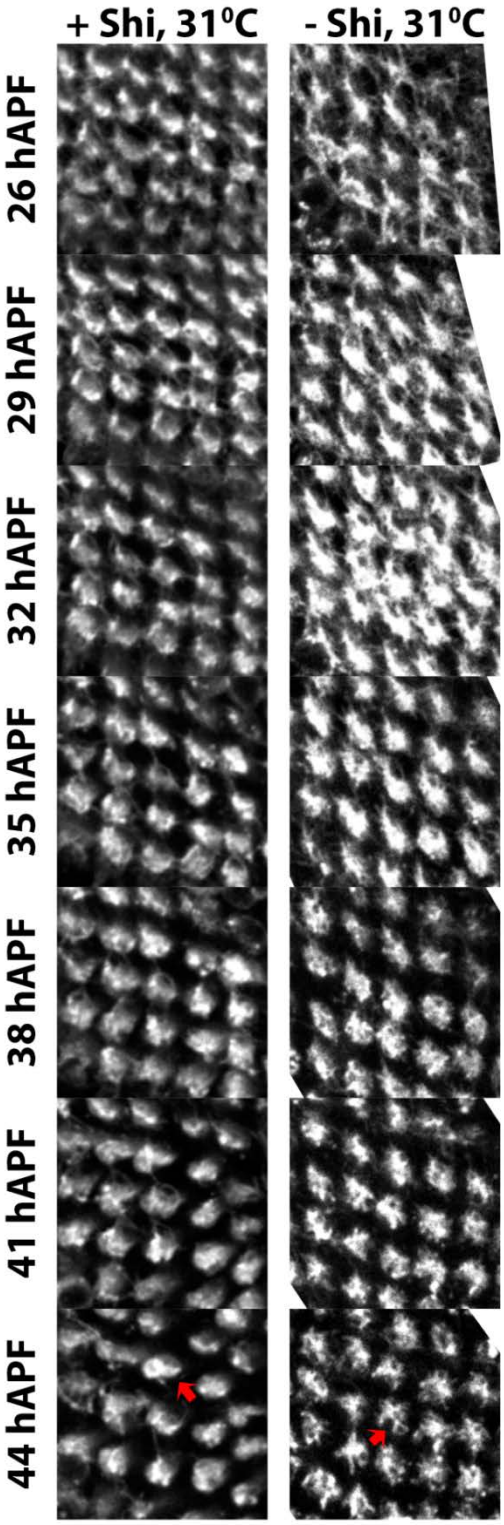
+ Shi, 31°C
- Shi, 31°C
26 hAPF
29 hAPF
32 hAPF
35 hAPF
38 hAPF
41 hAPF
44 hAPF

Figure 3 4. Temperature sensitive mutant shibire^{ts} expression in L-cells at restrictive temperature causes L-cells to lose their filopodial dynamics.

(Left panels from top to bottom) 2-photon intra-vital time series pictures of same set of L-cell neurites in an experimental animal expressing *shibire^{ts}* at restrictive temperature. L-cells lose their filopodial dynamics and do not cover the entire lamina plexus (compare with the control on the right panels, especially at 29 and 32 hAPF). At 44 hAPF, they become blobs instead of acquiring a star shape (compare the L-cell neurites that are shown by red arrows). (Right panel from top to bottom) 2-photon intra-vital time series pictures of same set of L-cells in a control animal at restrictive temperature without expressing *shibire^{ts}*.

Figure 5

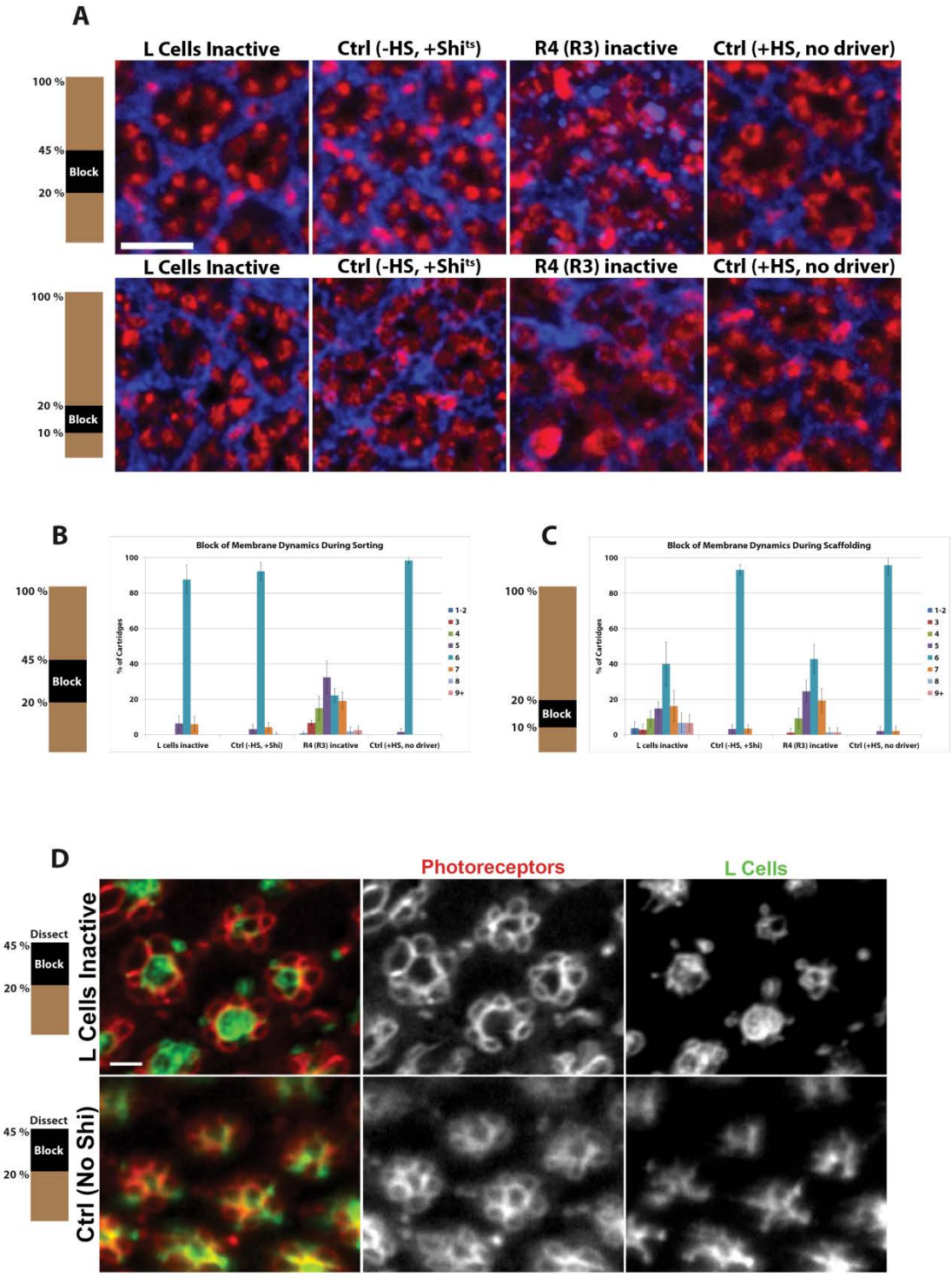
A
L Cells Inactive
Ctrl (-HS, +Shi^ts)
R4 (R3) inactive
Ctrl (+HS, no driver)
100 %
45 %
Block
20 %
L Cells Inactive
Ctrl (-HS, +Shi^ts)
R4 (R3) inactive
Ctrl (+HS, no driver)
100 %
20 %
Block
10 %
B
Block of Membrane Dynamics During Sorting
% of Cartridges
L cells inactive
Ctrl (-HS, +Shi)
R4 (R3) incative
Ctrl (+HS, no driver)
1-2
3
4
5
6
7
8
9+
C
Block of Membrane Dynamics During Scaffolding
D
Photoreceptors
L Cells
L Cells Inactive
Ctrl (No Shi)
Dissect
Block

Figure 3 5. L-cell membrane dynamics are not required during photoreceptor targeting but scaffolding.

(A, top four panels) Adult lamina after L-cell membrane dynamics were blocked between 20-45 hAPF. Blue is glia, red is photoreceptor terminals. Left-most panel shows adult lamina when membrane dynamics of L-cells were blocked and cartridge organization is very similar to controls (2^{nd} and 4^{th} panels). When membrane dynamics of only 2 photoreceptor subtypes (R3 and R4) were blocked (3^{rd} panel), lamina organization is completely messed up. (A, lower four panels) Adult lamina after L-cell membrane dynamics were blocked from 10-20 hAPF. Blue is glia, red is photoreceptor terminals. First picture shows adult lamina when L-cell membrane dynamics were blocked and cartridge organization is disrupted in comparison to controls (2^{nd} and 4^{th} panels). When membrane dynamics of only 2 photoreceptors were blocked (3^{rd} panel), lamina organization is completely messed up as in the case of block between 20-45 hAPF. (B) Percentage of cartridges with different number of terminals in the adult laminae when membrane dynamics were blocked between 20-45 hAPF. (C) Percentage of cartridges with different number of terminals in the adult laminae when membrane dynamics were blocked between 10-20 hAPF. (D) Pictures of laminae at ~45 hAPF. Photoreceptors are in red, L-cells are in green. After membrane blockage between 20-45 hAPF, both experimental and control groups dissected immediately. Compare the morphologies of L-cell neurites in the upper panels with controls in the lower panel. Data is shown as mean ± SD. n >50 for each group. Scale bar is 5 μm in (A), 2 μm in (D).

Figure 6

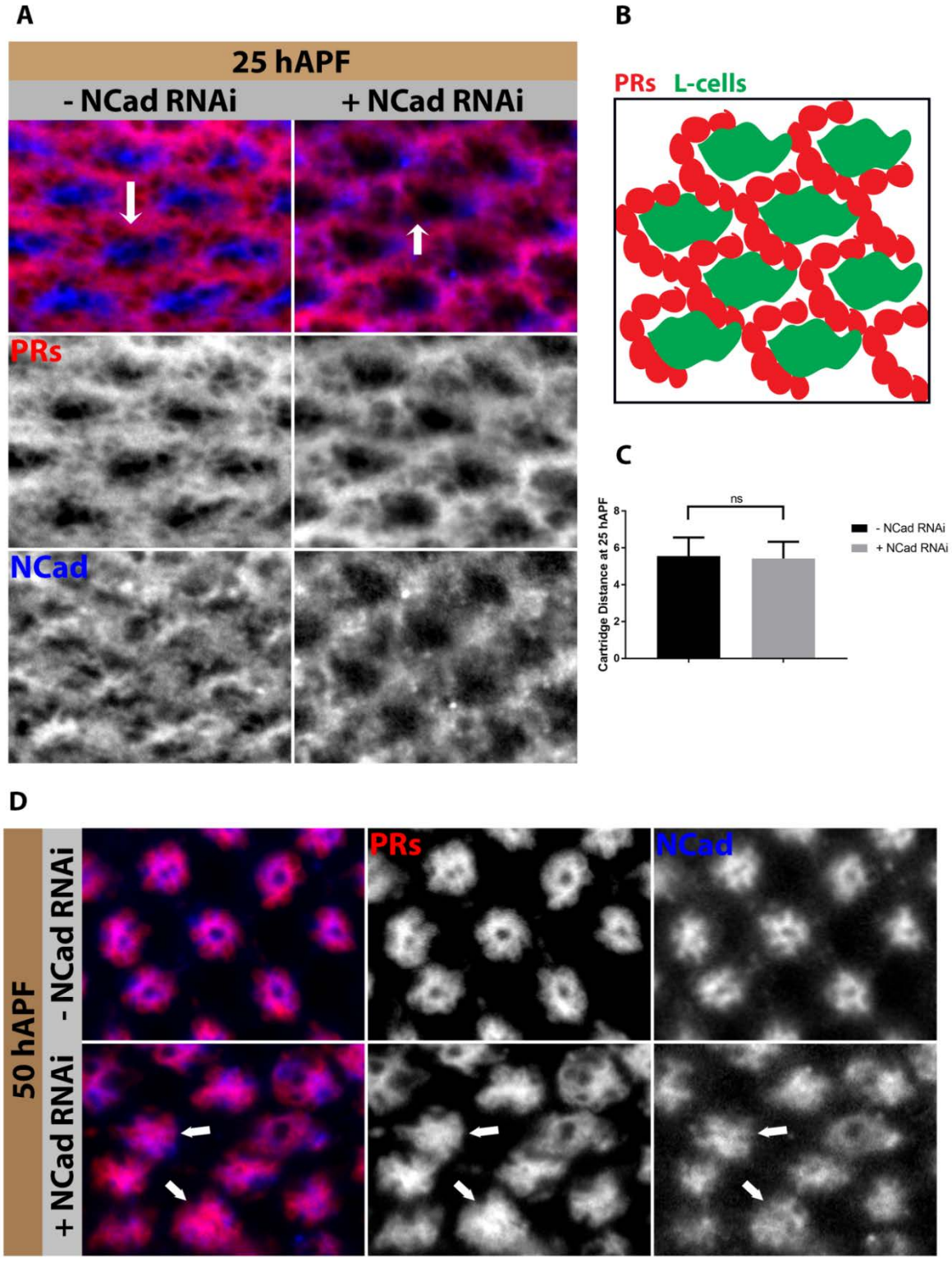
A
25 hAPF
- NCad RNAi
+ NCad RNAi
PRs
NCad
B
PRs L-cells
C
ns
Cartridge Distance at 25 hAPF
0
2
4
6
8
- NCad RNAi
+ NCad RNAi
D
50 hAPF
- NCad RNAi
+ NCad RNAi
PRs
NCad

Figure 3.6. N-Cadherin function in L-cells is not required for correct scaffold formation.

(A) Pictures of lamina after N-Cadherin was knocked down with RNAi in L-cells. Red marks photoreceptors, blue is N-Cadherin. N-Cadherin expression in L-cells (shown in schematic in B) drastically reduced in comparison to controls. (C) Comparison of mean cartridge distances (in µm) as a measure of scaffold integrity. At 25 hAPF there is no significant difference between control vs. when N-cadherin is absent in L-cells. n>149, unpaired t-test. (D) N-Cadherin has a late function in L-cells to keep the organization of cartridges intact. Arrows show collapsed cartridges.

Figure 7

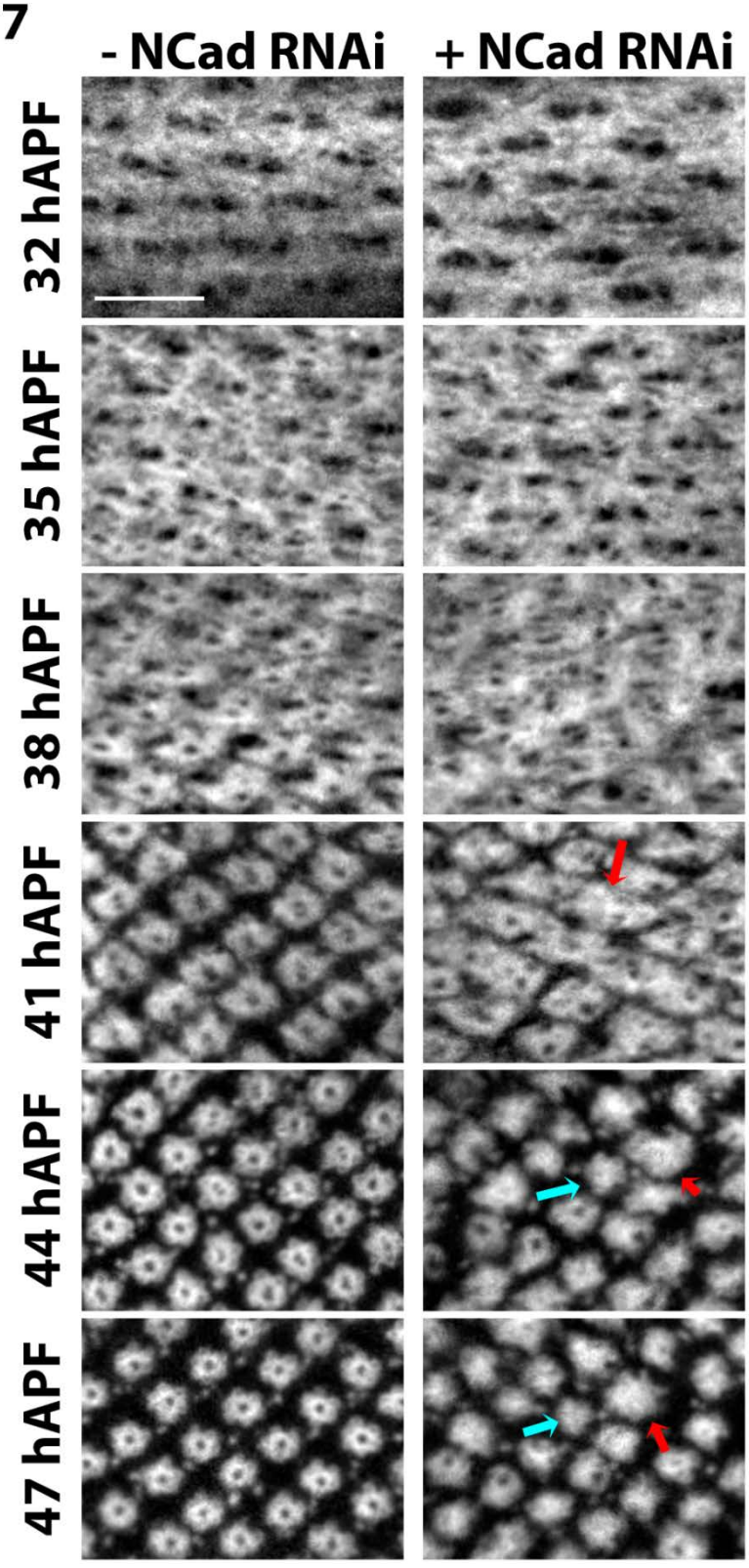
- NCad RNAi
+ NCad RNAi
32 hAPF
35 hAPF
38 hAPF
41 hAPF
44 hAPF
47 hAPF

Figure 3.7. N-Cadherin function in L-cells has a late role in photoreceptor targeting

2-photon, intravital time series pictures of all photoreceptors in the lamina when N-cadherin was knocked down in all L-cells (left panels) vs control (right panels). Defects in lamina organization start to arise around 38 hAPF, which is almost the end of sorting period. At 41 hAPF, when L-cells are devoid of N-Cadherin, size of cartridges start to show differences in comparison to controls (red arrow at 41 hAPF panel). By 44 hAPF, cartridges start to collapse (cyan arrows at 44 and 47 hAPF panles). In addition, after 41 hAPF, some cartridges start to fuse with each other (red arrows at 44 and 47 hAPF panels).

3.6 CHAPTER THREE SUPPLEMENTAL FIGURES

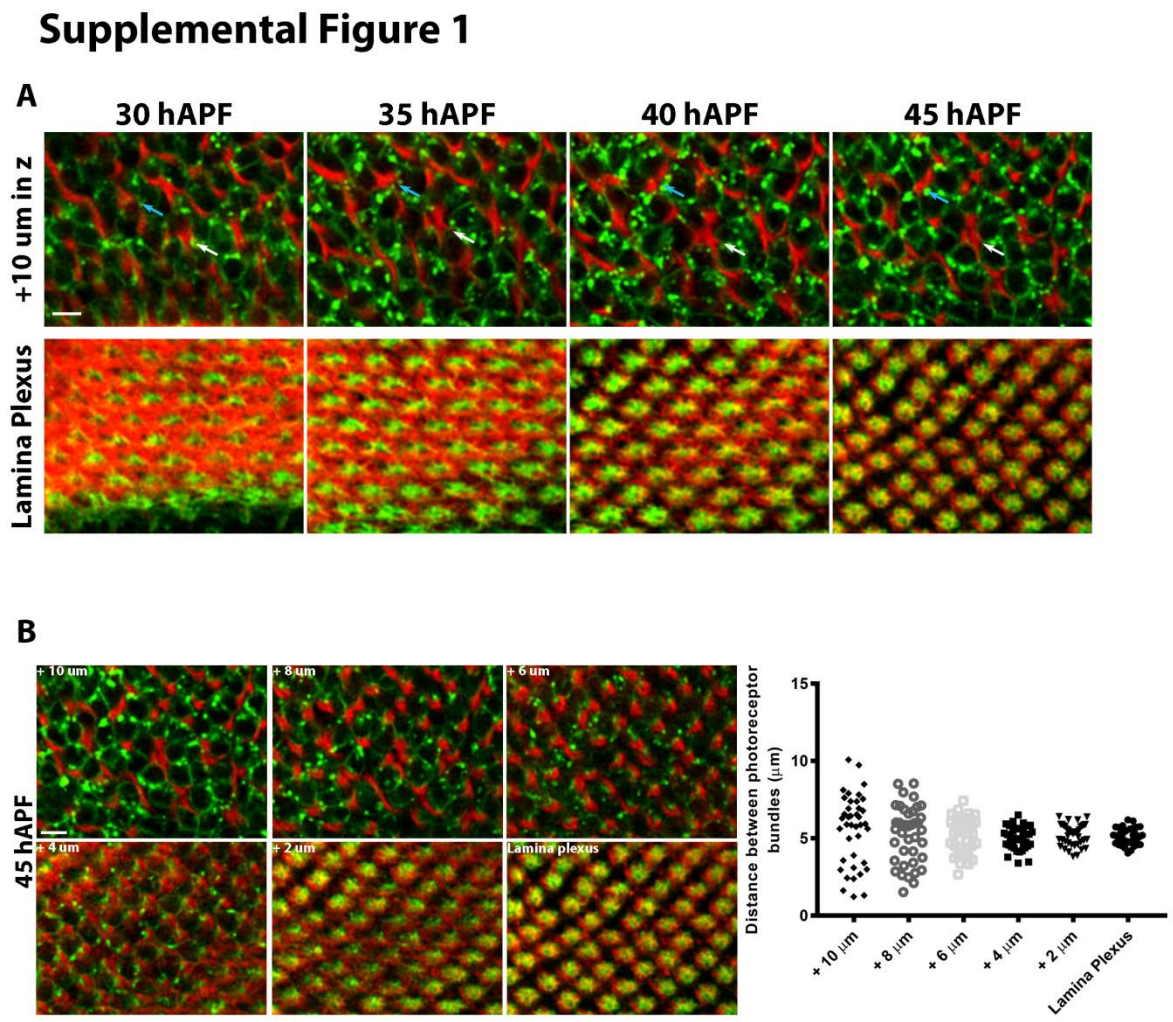

Figure S3 1. Photoreceptor bundle organization remains the same at the same z-level over time, but changes at different depths of the L-cell body layer.

(A) Photoreceptor bundle organization is shown 10μm above and at the lamina plexus. Blue and white arrows show the same bundles over time. (B) Photoreceptor bundle organization at different depth of the L-cell body layer at 45 hAPF. Bundles get organized as they get closer to the lamina plexus. Quantification shows that the distances between bundles approach around 5μm at lamina plexus.

Supplementary Figure 2A

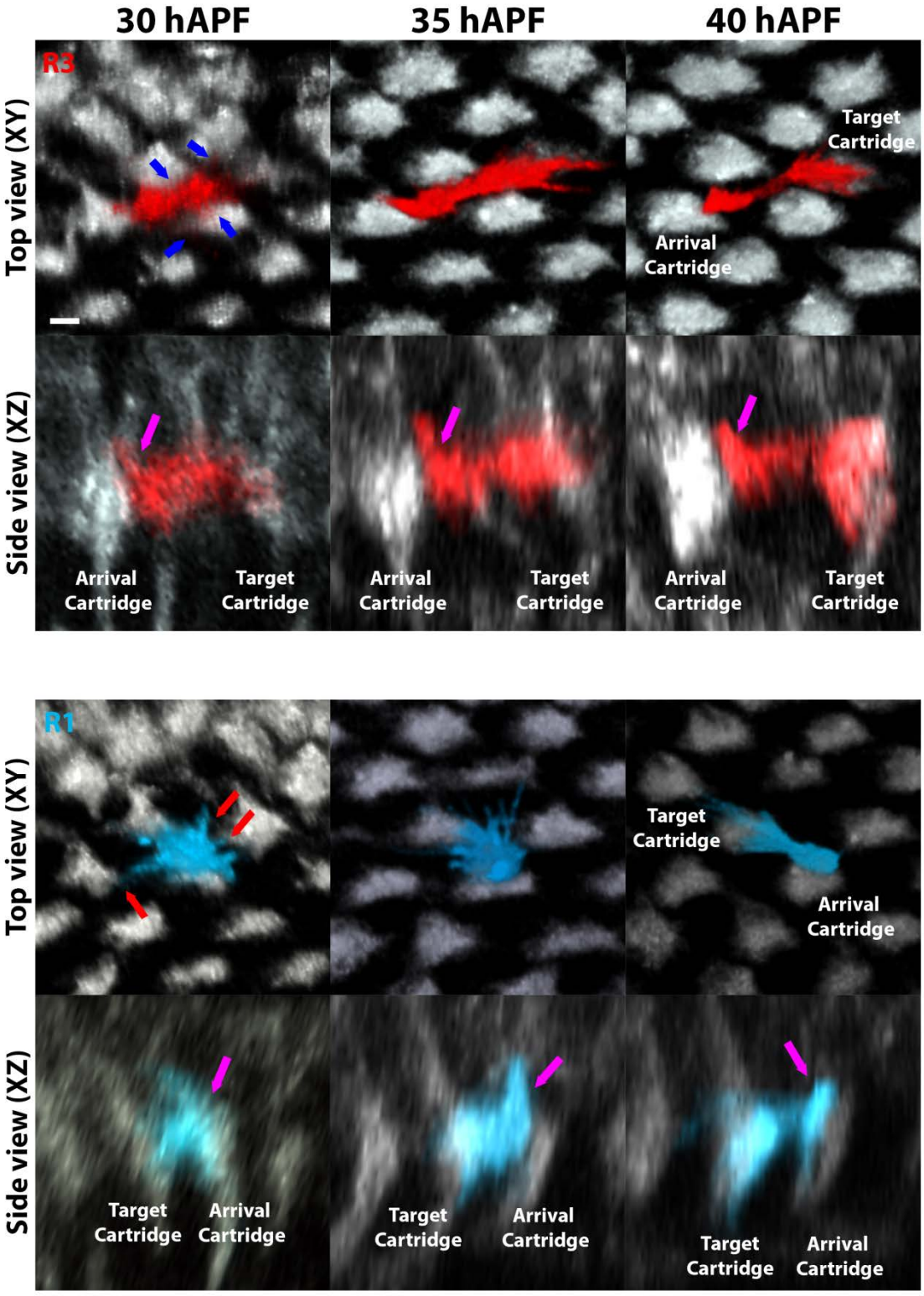

Figure S3 2A. R3 and R1 photoreceptors sort at the same plane with L-cell neurites while contacting with many L-cell neurites that are in wrong cartridges.

(Top six panels) An individual R3 is labelled in red, L-cell neurites are in gray. Top and side views of the same R3 at different times during sorting is shown. In the side views, pink arrow shows the initial arrival cartridge of the R3. Blue arrows in the top view of 30 hAPF show the contacts that the R3 makes with L-cell neurites in wrong cartridges. (Lower six panels) An individual R1 is labelled in blue, L-cell neurites are in gray. Top and side views of the same R1 at different times during sorting is shown. In the side views, pink arrow shows the initial arrival cartridge of the R1. Red arrows in the top view of 30 hAPF show the contacts that the R1 makes with L-cell neurites in wrong cartridges.

Supplementary Figure 2B

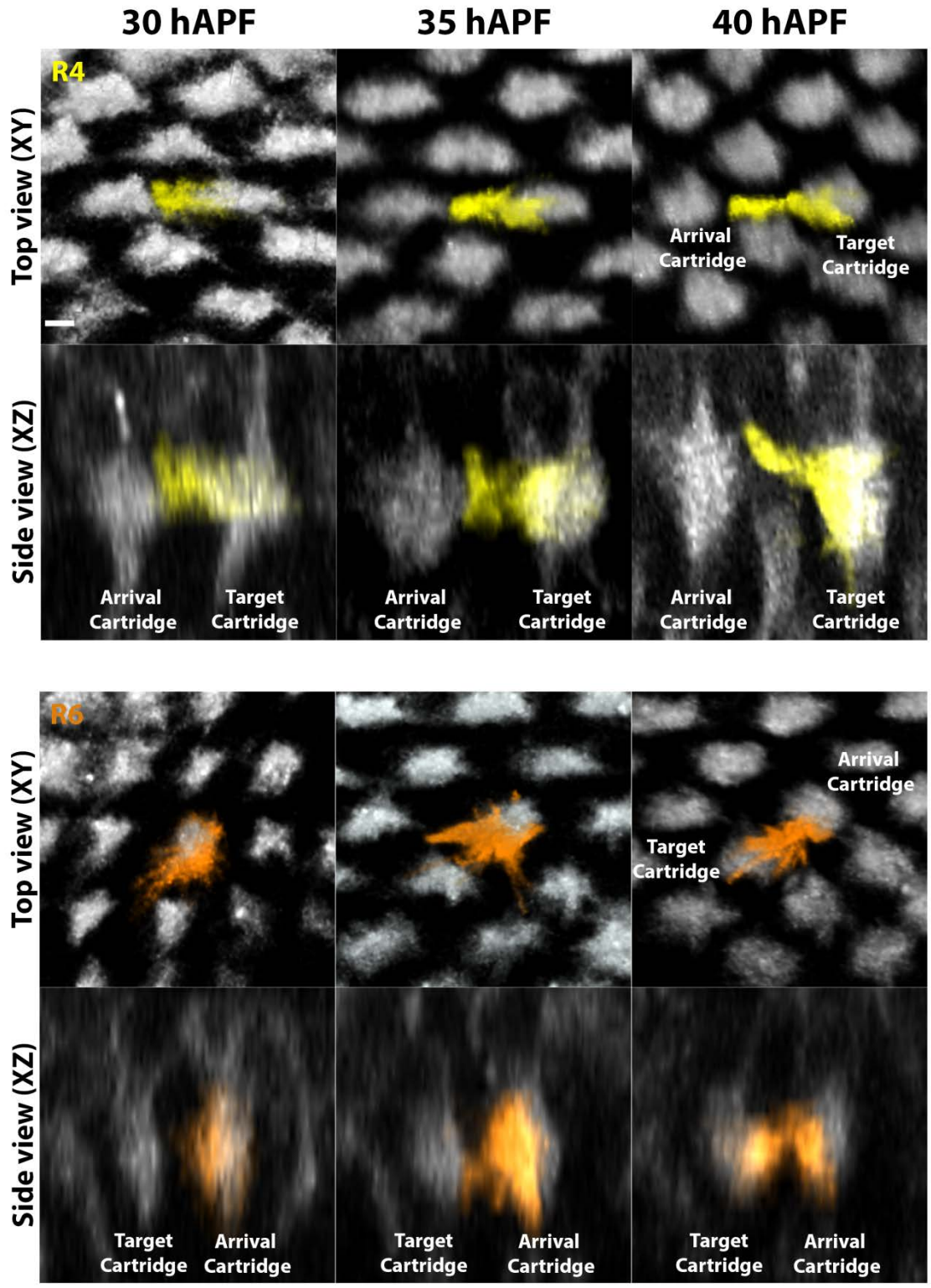

Figure S3.2B. R4 and R6 photoreceptors sort at the same plane with L-cell

(Top six panels) An individual R4 is labelled in yellow, L-cell neurites are in gray. Top and side views of the same R4 at different times during sorting is shown. (Lower six panels) An individual R6 is labelled in orange, L-cell neurites are in gray. Top and side views of the same R6 at different times during sorting is shown.

Supplementary Figure 2C

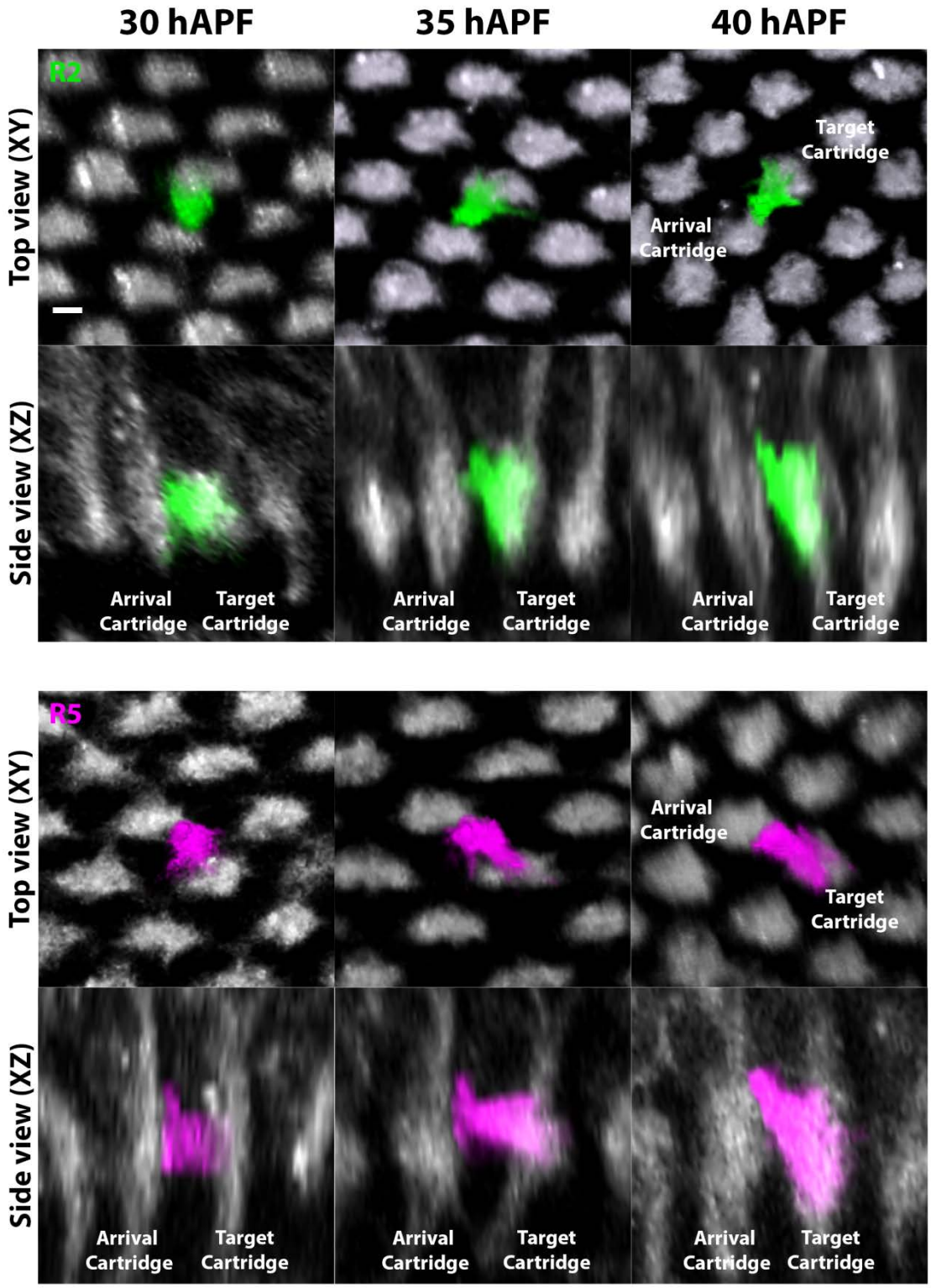

Figure S3.2C. R2 and R5 photoreceptors sort at the same plane with L-cell

(Top six panels) An individual R2 is labelled in green, L-cell neurites are in gray. Top and side views of the same R2 at different times during sorting is shown. (Lower six panels) An individual R5 is labelled in magenta, L-cell neurites are in gray. Top and side views of the same R5 at different times during sorting is shown.

Supplemental Figure 3

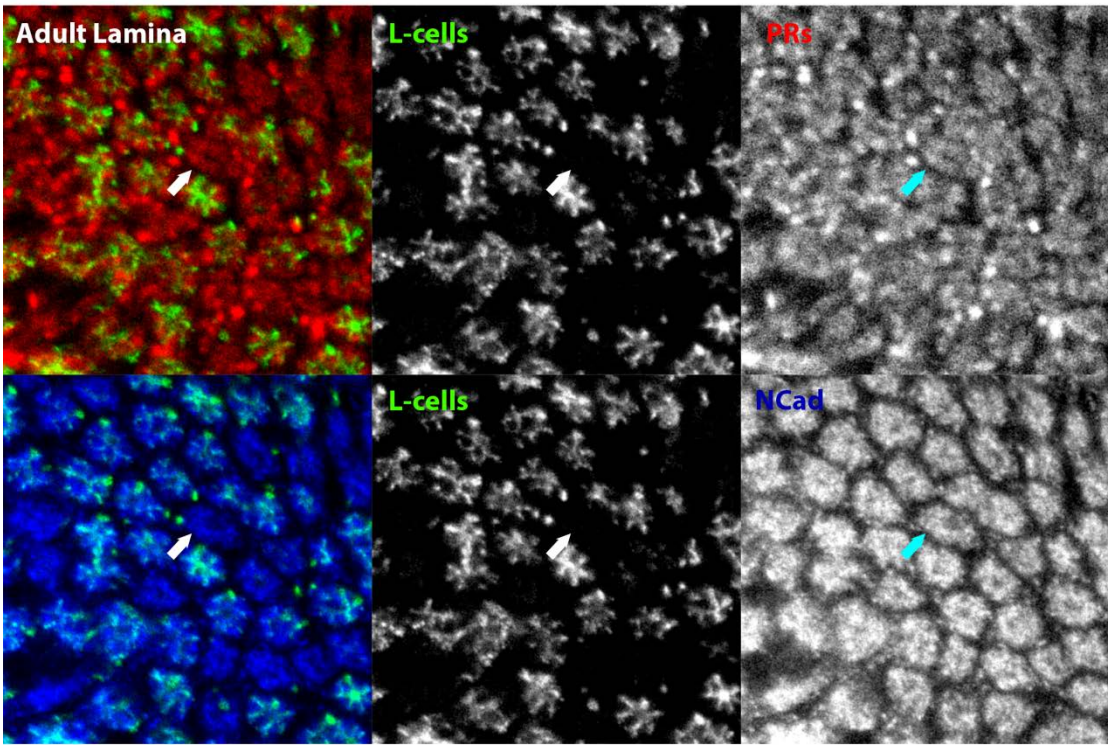

Figure S3.3. N-cadherin signal in the adult lamina persists in the absence of L-cells

An adult lamina, after L-cells are ectopically ablated. Photoreceptors are in red, L-cells are in green, N-cadherin is in blue. Arrows show a cartridge where there are no L-cells. In the same cartridge N-Cadherin is still available.

CHAPTER FOUR

Materials and Methods

Acknowledgement

2-photon intravital imaging technique that I used for my experiments was developed by me.

All the intravital imaging and fixed tissue experiments in Chapter Two were conducted solely by me and Dr. Marion Langen. In addition, stock maintenance and generation of flies with different genotypes were conducted by me and Dr. Marion Langen. Computational model was developed by Dr. Steven Altschuler and Dr. Lani Wu.

In Chapter Three, all the experiments and the necessary fly lines were designed and generated by me. All the experiments, except L-cell ablation experiments, are performed by me. L-cell ablation experiments were performed by Charlotte Wit.

4.1 EXPERIMENTAL PROCEDURES FOR CHAPTER TWO

Fly Stocks

Flies with the following genotypes were used to visualize photoreceptor growth cones and lamina cells. To label all photoreceptors, we used +;GMR-Gal; UASCD4- td GFP; for sparse random photoreceptor labeling, we used hsFlp/+; GMR-FRT-w+-FRT-Gal4/+; Uas-CD4-td-GFP/+; for labeling of only R1 and R6, we used GMRFlp/+;GMR-Gal4/+; Uas-CD4-td-GFP,

FRT80B / tubulin- Gal80, FRT80B and for L-cells, we used GH146Gal4/+; Uas-CD4-td-GFP/+. To induce sparse labeling, we heat shocked hsFlp/+; GMR-FRT-w+-FRTGal4/+; Uas-CD4-td-GFP/+ larvae for 12–15 min at 37°C 2 to 4 days after egg laying (AEL).

Immunohistochemistry and Fixed Imaging

Pupal brains were dissected and prepared for confocal microscopy. The tissues were fixed in PBS with 3.7% formaldehyde for 20 min and washed in PBS with 0.4% Triton X-100. The following antibodies were used: Chaoptin (1:50). For secondary antibodies, we used Cy3 (3:500; Jackson ImmmunoResearch Laboratories). For fixed images, we used a Leica SP5 Confocal Microscope with HyD detectors.

Intravital Imaging

Pupae with the correct genotype were collected at 0 hrs after puparium formation (APF) and aged at 25°C. In preparation for imaging, the pupal case surrounding the head was removed, exposing both eyes (Figure 4.1A). Double sided tape (Scotch, 3M, Cat. No. 665) was adhered to a glass slide (VWR Microscope Slides, Cat.No. 16005-106) and 0.7x0.5 cm filter paper (Fisher Scientific, Cat.No. 09-790-2F) then placed on the tape. The pupa was placed sideways on the filter paper with its right eye facing up. Another small filter paper was placed at the tip of the tail to prevent the pupa from moving. These two filter papers were moistened so that other layers of filter paper would remain in position on top of each other. Two 1.2x0.1 cm wet filter papers were

placed in parallel on either side of the pupa to constitute the second layer. On top of the second layer, an additional two 1.2x0.1 cm wet filter papers were placed at the tip of the head and tail, perpendicular to the pupa's main body axis. Finally, on top of the third layer, two 1.2x0.1 cm wet filter papers were placed in parallel one on either side of the pupa as the fourth and last layer (Figure 4.1C,D). The right eye of the pupa should be in a slightly higher position than the last layer of filter paper such that the cover slip is closest to the eye. 4% low melting point agarose (Ultra Pure Low Melting Point Agarose, Invitrogen, Cat. No. 15517-022) was applied at the points union between the wet filter paper layers to stabilize the paper tower around the pupa. Once the agarose had set, high vacuum grease (Dow Corning Corporation) was applied by a syringe around the double-sided tape to form a square wall. The thickness of the grease was slightly larger than the distance between the right eye and the glass slide. Grease served as further support for the cover slip. 1.5 µl HL3 solution (Stewart et al., 1994) or PBS was put on the cover slip (VWR micro cover glass, 22x22 mm, No.1.5, Cat.No. 48366-227) and the cover slip was placed on the pupa such that the drop of HL3 touches the pupal eye. Once the contact between the cover slip and the grease was secured and the contact between the cover slip and the pupal eye established, samples were immediately imaged. Imaging data were obtained using a Zeiss LSM 780 upright Multi-photon with a Non Descanned Detector (NDD) and an LD C-Apochromat 40x/1.1 W Korr UV-VIS-IR objective. Developing pupae were recovered from the imaging chamber after 24 hours of continuous scanning to develop in a humid chamber to adulthood. We only analyzed scanned data from pupae that subsequently developed to become healthy adults.

Analysis of 4D data

All original 4D imaging data were processed using Amira 5.2.2 (FEI Visualization Sciences Group) using volume rendering, surface rendering and manual image segmentation tools. For each image stack at a given time point, growth cones were manually segmented and traced through all time points using the Segmentation Editor. Growth cones were identified based on morphology and cell body position. Each threedimensional growth cone was volume rendered using a single color map. A total of 13 clusters of 2-12 growth cones were manually corrected for all rotations and aligned in a viewing angle orthogonal to the XY plane ('top view', Movies 05-17). Individual images were aligned in Adobe Photoshop. All movies were assembled in Windows Moviemaker. To analyze the dynamics of single growth cones, coordinates were taken from heel, front, longest heel filopodium and longest growth cone front filopodium using ImageJ (NIH). These coordinates were then exported to Excel. A Matlab program was implemented to calculate the angle and length of each individual growth cone for each time point using the aforementioned coordinates. We used as measured angle the precise measurements of the longest average front filopodial angles between 30h and 35h APF. Graphs were generated in Matlab (MathWorks). Final figures were assembled in Photoshop. To determine individual growth cone positions within the anterior-posterior axis of the lamina plexus, the lamina plexus for the last time point of each data set was manually segmented. For each data set, the last time point of individually isolated, color-coded growth cones was visualized together with the isolated lamina as a background. For each growth cone, the distance from the most anterior point to the heel and the distance between the most anterior and most posterior points were measured by SplineProbe tool of Amira 5.2.2. The ratio of the measured distances was calculated to determine the position

of the growth cone along the anterior-posterior axis. For the tracing of individual R cell axons in fixed preparations (Suppl. Fig. 1B), axons were traced as dark interiors surrounded by high-quality 24B10 stainings in conventional confocal image stacks of fixed preparations. In total, we measured 58 growth cones, including 9xR1, 6xR2, 16xR3, 12xR4, 6xR5, 9xR6 cells (Fig4B-F).

Implementation of the computational framework (by Dr. Steven Altschuler and Dr. Lani Wu)

The three rules of growth cone sorting were implemented (in Matlab v.2014a) as follows. Refer to Supplementary Figure 3 for the following description.

The scaffolding rule: Guided by the experimental data, we constructed the "heel" grid as follows. (1.) To create a diamond-shaped grid, we placed bundle centers (gray diamonds) down on integer lattice points and then shifted every other row in the x direction by one half. (2.) For the dorsal portion of the grid, we placed the R1-R6 heels at equal angles apart in an ellipse around each center: ($a \cos(\phi_n)$, $b \sin(\phi_n)$), with $\phi_n = -[\alpha + (n-1)(\pi - 2\alpha)/5]$ and n = 1 to 6. We set b = ½, and solved numerically for *a* (the width of the ellipse) and α (the offset angle from 0 or - π for R1 and R6 respectively), using the following two experimentally observed constraints (see Suppl. Fig. 3): (i) heels R1 and T_R(R5) have the same *x* position; and (ii) the differences in *y* positions of T_R(R5) – T_R(R4) and R1 – T_R(R4) are equal. Here, T_R is the translation of a heel by (1/2, 1/2) (see arrow in Suppl. Fig. 3). The heel positions were inverted with mirror-symmetry along the x-axis to create the ventral portion of the grid. (3.) We warped the grid by 10°, as observed in the experimental data (see olive-colored diamond in figure). The grid was

normalized so that the distance from a bundle center C to $T_R(C)$ was normalized to unity (edges of diamond are length 1).

The extension and stop rules: The "idealized" direction and speed of each R-cell was computed so that all R-cells would reach the intended target at 40 hrs APF. (For simulations testing wiring robustness, the direction in which R-cells of each given type moved was altered by a randomly selected angle within the stated ranges.) Each R-cell front was assigned one of two states: "moving" or "stopped". These states were computed based on the numbers and types of neighbors whose centers were within a prescribed sensing radius (SR). The time at which sensing began could be delayed and was set to 1/5 of the extension distance (corresponding to 3h after start [28h APF] unless otherwise noted. As described in the main text, this allowed us to explore combinatorial rules for stopping. When in a "moving" state, an R-cell extended linearly. We note that in some cases "stopped" states can switch back to "moving states" due to non-transitivity of stopping conditions. For example, consider the case of a rule that tells an extending R-cell to stop if two other R-cells are nearby. Then two R-cells passing to the left and right of a third R-cell (but not near any other cells) would stop the one in the middle, but not be stopped themselves; after moving away, the middle cell could switch back to moving. This non-transitivity makes it difficult to predict theoretically the final configurations of the R-cells, and is the reason why simulations were required for this study.

Measurements of wiring accuracy: Final wiring accuracy was computed at the end of the simulation by counting the number of cells that were stopped within a Voronoi cell around each

center. (A Voronoi cell around a target is the set of points that are closer to that target than any other target.) The number was compared with idealized numbers at or away from the equator.

Area overlap: For each time step during the simulation, all areas of overlap between queried R-cell (with or without target cell) were summed and then normalized by the area of the queried R-cell's sensing disk. In Fig 5G-K, only overlap with the target cell was computed; in Fig 6I overlap with all other cells was computed.

4.2 EXPERIMENTAL PROCEDURES FOR CHAPTER THREE

Fly Stocks

Flies with the following genotypes were used to visualize photoreceptor growth cones and lamina cells.

- To label all photoreceptors: +;+; GMR-tdTom (Gift from Larry Zipursky)

- To label all photoreceptors and L-cells at the same time; eyGal80/+ or Y;UAS-CD4tdGFP/+;GMR-tdTom/9B08-GAL4 (Han et al., 2011; Pecot et al., 2014)

- For sparse random photoreceptor labeling in the background of labelled L-cells; hsFlp/+; GMR-FRT-w+-FRT-Gal4/LexAop-Tom; UAS-CD4tdGFP/27G05-LexA (Rintelen et al., 2001), 27G05-LexA is a gift from Larry Zipursky

- To label all photoreceptors while knocking down N-Cadherin in all L-cells; +;GCM-GAL4/UAS-CadN-RNAi;GMR-tdTom/+ (Schwabe et al., 2014). UAS-CadN-RNAi is obtained from VDRC (1093).

- For L-cell ablation experiments we used UAS-Hid/Y;UAS-CD4tdGFP/+;9B08-GAL4; (Grether et al., 1995)

- To block membrane dynamics of L-cells (*shibire*^{ts} experiments) and at the same time labeling them with GFP; eyGal80/+ or Y;UAS-CD4tdGFP/+;9B08-GAL4/UAS-shi^{ts}.

- For control experiments of *shibire*^{ts} experiments; +;+/Cyo or CyoGFP;UAS-shi^{ts}

- To induce sparse labeling, I heat shocked hsFlp/+; GMR-FRT-w+-FRTGal4/LexAop-Tom; UAS-CD4tdGFP/27G05-LexA larvae for 12–15 min at 37°C 2 to 4 days after egg laying (AEL).

Immunohistochemistry and Fixed Imaging

Pupal brains or adult brains were dissected in PBS and prepared for confocal microscopy. The tissues were fixed in PBS with 3.7% formaldehyde for 30-50 min and washed in PBS with 0.4% Triton X-100 for at least 2 hours. The following antibodies were used: anti-Chaoptin (1:50), anti-ebony (1:200), anti- N-Cad (mAb DNEx8) (1:50). For secondary antibodies, we used Cy5, Cy3 (3:500; Jackson ImmmunoResearch Laboratories). For fixed images, we used a Leica SP8 White Laser Confocal Microscope with HyD detectors.

2-photon Intra-vital imaging

Imaging chambers were prepared as explained above. For live *shibire^{ts}* experiments, to keep the temperature constant at 31°C, I used a temperature controller (Cube) with a closed chamber (Life Imaging Service). I acquired all the live imaging data with Leica SP8 upright multiphoton microscope which is equipped with HyD detectors. For 2 channel image acquisition, I used Coherent Chameleon laser along with Chameleon Compact OPO (optical parametric oscillator): Chameleon Compact OPO provide me with longer wavelength excitation for red shifted fluorophores whereas I used Coherent Chameleon laser to excite GFP.

Shibire^{ts} experiments

Fly crosses were kept at room temperature (22°C). White pupae were collected at 0 hAPF and placed in an Eppendorf tube which had a hole for air and damp tissue at the bottom for humidity. Eppendorf tube was placed in a 25°C incubator for staging. For blocking membrane dynamics during photoreceptor extension period, pupae were kept at 25°C for 20 hours and afterwards immediately put on a heating block (Corning) which was set at 31°C and kept there for 25 hours. After 25 hours, pupae were either dissected directly, or put in a humid vial at 22°C until adulthood. Once they hatched, 1-7 day old flies were dissected and their laminae were analyzed. For blocking membrane dynamics during scaffolding, white pupae were collected at 0 hAPF and kept at 25°C incubator for 10 hours. After 10 hours, pupae were placed in a heating block at 31°C for 10 hours. Afterwards, pupae were kept at 22°C until adulthood and dissected for analyzing their laminae.

Cell Ablation Experiments

To stress the cells and achieve more cell killing, we kept our crosses at 29°C at all times. Since development at 29°C is faster than it is at 25°C , for 25% development analysis, we dissected pupae which were kept at 29°C for 20 hours. We only analyzed male pupae or male adult laminae because eyGal80 construct that we had in our 9B08-GAL4 stocks suppressed the expression of UAS-hid and prevented cell killing. When a cartridge lacked all L-cells, we defined its immediate neighbors as primary, and the second row of neighbors as secondary.

Image Analysis

All the live and fixed image analyses were done in Amira 5.6 (FEI Visualization Sciences Group). For the live experiments, same set of cells were found for all time points and a cross section picture was taken by using oblique slicer tool. Afterwards all the images were aligned, and all the figures were assembled in Adobe Photoshop CS6.

4.3 CHAPTER FOUR FIGURES

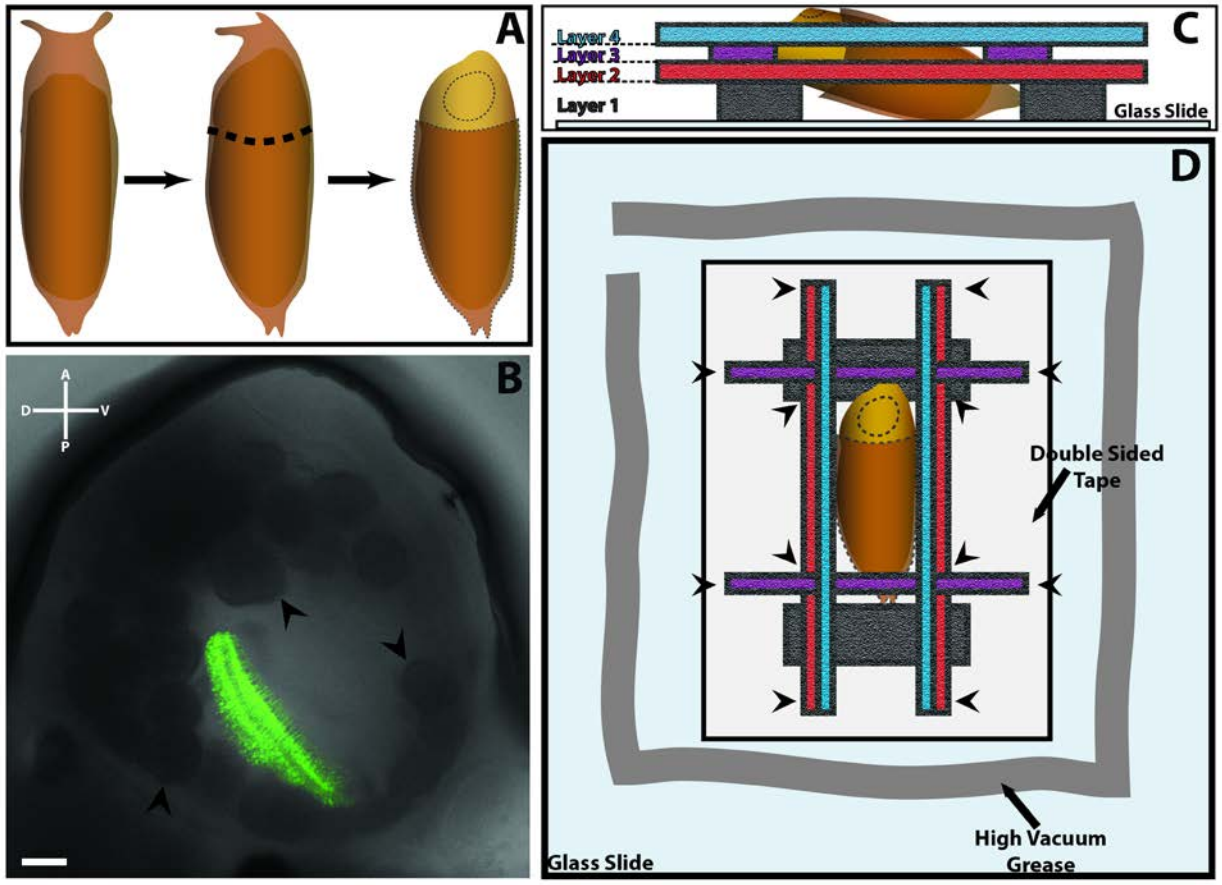

Figure 4 1. Intravital Imaging Chamber

(A) Pupa is aligned such that the right eye is imaged after the cuticle around the head is dissected. (B) Transmitted light image of the right eye of a pupa. Lamina neurons are genetically labelled with GFP, revealing the position of the lamina layer of the optic lobe. Arrowheads mark the lipid bodies. (C) Side view of the imaging chamber. Four layers of filter paper are shown in different colors for clarity. Pupa is kept in position as the whole body axis makes an angle with the plane of the glass slide. (D) Top view of the imaging chamber. Layers are shown in the same colors as in C. Arrowheads show the positions where 4% agarose is applied.

CHAPTER FIVE

Concluding Remarks and Future Directions

The results that are presented in this work support the idea that simple pattern formation rules can wire a seemingly complicated neural circuit without needing matchmaking codes between synaptic partners. But where do we go from here? What do we do with these rules?

Once the underlying simple rules for development of any neural circuit is set, the next challenge is to find how these rules are implemented, in other words what molecular mechanisms execute these rules. Developmental rules can give us a conceptual framework which will greatly facilitate our understanding of the functions of molecules. For example, in the example of *Drosophila* visual map formation, two cell adhesion molecules, *flamingo* and *CadN* were found to be required for correct wiring establishment (Chen and Clandinin, 2008; Prakash et al., 2005; Schwabe et al., 2013). *Flamingo* was suggested to be regulating extension angles of photoreceptors and *CadN* was suggested to be an attractive cue between photoreceptors and L-cells. Schwabe et.al. (2013) further showed that CadN is mostly localized at the filopodial tips and flamingo is at the base of the growth cone. The developmental rules that I presented in this work perfectly align with the proposed functions of these proteins and suggest further functions to be inquired. For example, by localizing at the heels of growth cones, flamingo not only can regulate the extension angles but also maintain the stability of the scaffold which, based on the data I presented in this work, seems to be a prerequisite for correct wiring establishment.

Similarly, CadN that is localized at the growth cone fronts can be the molecule that photoreceptors use to sense other photoreceptors to implement the stop rule in our developmental algorithm. In this way we can place the function of molecules like pieces of puzzle on a board whose borders are determined by developmental rules. To understand how the rules are implemented by different molecules, one would need to observe the live dynamics of these molecules because the expression dynamics of these molecules would provide us with constraints on when and where they function. For example if CadN is not expressed at the growth cone fronts around the time sorting ends, it probably cannot function as the signal that photoreceptors use to sense other growth cone fronts. Then one of the next challenges is to capture the dynamics of endogenous proteins that might execute any of the underlying developmental rules of a biological process.

L-cells as organizers of the target field

The data in Chapter 3 suggest that L-cells do not act as target cues for photoreceptors but they organize the target field such that they ensure correct wiring. This is a surprising finding because since the development of L-cells depends on signals coming from photoreceptors that are innervating the lamina, it was thought that photoreceptors organize the target filed. This result is in accordance with a previous study where it has been found that if lamina precursor cells are prevented to mature and form lamina columns, photoreceptors cannot associate with

them and the lamina organization seemed to be disrupted at larval stages (Umetsu et al., 2006). But how can L-cells organize the lamina such that photoreceptor bundles would arrive the lamina plexus in a highly ordered manner? One idea is that, once the L-cells mature and extend their neurites, they might tile the lamina plexus. For this they can use two simple mechanisms: first they can avoid themselves which would cause the neurites to spread and second they can be repulsed by their neighboring neurites. By this way they would be confined to a specific area in an orderly manner. Conceptually this would be similar to many magnets repulsing each other on a plane; eventually they will come to rest once all the repulsive forces are balanced which would suggest an orderly organization.

While passing through L-cell bodies, photoreceptor bundles seemed to be getting organized as they approach the lamina plexus. In addition, every single bundle makes a precise 180° rotation. Whether L-cells play any role in these organizational changes is unclear. With cell ablation experiments, one might gain some insight into these processes and delineate the underlying developmental rules. With the constraints that are put forward by these rules, search for molecules that realize these processes can become easier. Finally, one can ask what the functional relevance of these organizational alterations is, i.e. whether 180° rotation of bundles has any function in the vision of the flies. This question would require behavioral experiments on top of the cellular perturbation experiments.

Another question that is to be answered is that what the contribution of each L-cell for the determination of scaffold is. It is unclear in what order L-cells differentiate or extend their

neurites to lamina plexus. Single cell ablation experiments and live imaging of early pupae development would provide answers to these open questions.

BIBLIOGRAPHY

Agi, E., Langen, M., Altschuler, S.J., Wu, L.F., Zimmermann, T., and Hiesinger, P.R. (2014). The evolution and development of neural superposition. J Neurogenet *28*, 216-232.

Akin, O., and Zipursky, S.L. (2016). Frazzled promotes growth cone attachment at the source of a Netrin gradient in the Drosophila visual system. Elife *5*.

Baker, N.E. (2007). Patterning signals and proliferation in Drosophila imaginal discs. Curr Opin Genet Dev *17*, 287-293.

Bazigou, E., Apitz, H., Johansson, J., Loren, C.E., Hirst, E.M., Chen, P.L., Palmer, R.H., and Salecker, I. (2007). Anterograde Jelly belly and Alk receptor tyrosine kinase signaling mediates retinal axon targeting in Drosophila. Cell *128*, 961-975.

Braitenberg, V. (1967). Patterns of projection in the visual system of the fly. I. Retina-lamina projections. Exp Brain Res *3*, 271-298.

Cajal, S. (1909). Nota sobre la estructura de la retina de la mosca (M. vomitoria L.). Trab Lab Invest Biol Univ Madrid *7*, 217-257.

Cajal, S.R., and Sánchez, D.S. (1915). Contribución al conocimiento de los centros nerviosos de los insectos.

Carthew, R.W. (2007). Pattern formation in the Drosophila eye. Curr Opin Genet Dev *17*, 309-313.

Caudy, M., and Bentley, D. (1986). Pioneer growth cone steering along a series of neuronal and non-neuronal cues of different affinities. J Neurosci *6*, 1781-1795.

Chan, C.C., Epstein, D., and Hiesinger, P.R. (2011). Intracellular trafficking in Drosophila visual system development: a basis for pattern formation through simple mechanisms. Dev Neurobiol *71*, 1227-1245.

Chen, P.L., and Clandinin, T.R. (2008). The cadherin Flamingo mediates level-dependent interactions that guide photoreceptor target choice in Drosophila. Neuron *58*, 26-33.

Clandinin, T.R., Lee, C.H., Herman, T., Lee, R.C., Yang, A.Y., Ovasapyan, S., and Zipursky, S.L. (2001). Drosophila LAR regulates R1-R6 and R7 target specificity in the visual system. Neuron *32*, 237-248.

Clandinin, T.R., and Zipursky, S.L. (2000). Afferent growth cone interactions control synaptic specificity in the Drosophila visual system. Neuron *28*, 427-436.

Clandinin, T.R., and Zipursky, S.L. (2002). Making connections in the fly visual system. Neuron *35*, 827-841.

Cordero, J.B., Larson, D.E., Craig, C.R., Hays, R., and Cagan, R. (2007). Dynamic decapentaplegic signaling regulates patterning and adhesion in the Drosophila pupal retina. Development *134*, 1861-1871.

del Valle Rodriguez, A., Didiano, D., and Desplan, C. (2011). Power tools for gene expression and clonal analysis in Drosophila. Nat Methods *9*, 47-55.

Dietrich, W. (1909). Die facettenaugen der Dipteren (Z Wiss Zool), pp. 465-539.

Duguay, D., Foty, R.A., and Steinberg, M.S. (2003). Cadherin-mediated cell adhesion and tissue segregation: qualitative and quantitative determinants. Dev Biol *253*, 309-323.

Edwards, T.N., and Meinertzhagen, I.A. (2009). Photoreceptor neurons find new synaptic targets when misdirected by overexpressing runt in Drosophila. J Neurosci *29*, 828-841.

Fischbach, K., and Dittrich, A. (1989). The optic lobe of Drosophila melanogaster. I. A Golgi analysis of wild-type structure. Cell and tissue research *258*, 441-475.

Fischbach, K.F., and Hiesinger, P.R. (2008). Optic lobe development. Adv Exp Med Biol *628*, 115-136.

Frohlich, A., and Meinertzhagen, I.A. (1987). Regulation of synaptic frequency: comparison of the effects of hypoinnervation with those of hyperinnervation in the fly's compound eye. J Neurobiol *18*, 343-357.

Gao, S., Takemura, S.Y., Ting, C.Y., Huang, S., Lu, Z., Luan, H., Rister, J., Thum, A.S., Yang, M., Hong, S.T., *et al.* (2008). The neural substrate of spectral preference in Drosophila. Neuron *60*, 328-342.

Garrity, P.A., Lee, C.H., Salecker, I., Robertson, H.C., Desai, C.J., Zinn, K., and Zipursky, S.L. (1999). Retinal axon target selection in Drosophila is regulated by a receptor protein tyrosine phosphatase. Neuron *22*, 707-717.

Gonzalez-Bellido, P.T., Wardill, T.J., Kostyleva, R., Meinertzhagen, I.A., and Juusola, M. (2009). Overexpressing temperature-sensitive dynamin decelerates phototransduction and bundles microtubules in Drosophila photoreceptors. J Neurosci *29*, 14199-14210.

Greiner, B. (2006). Adaptations for nocturnal vision in insect apposition eyes. Int Rev Cytol *250*, 1-46.

Grether, M.E., Abrams, J.M., Agapite, J., White, K., and Steller, H. (1995). The head involution defective gene of Drosophila melanogaster functions in programmed cell death. Genes Dev *9*, 1694-1708.

Grutzendler, J., Kasthuri, N., and Gan, W.B. (2002). Long-term dendritic spine stability in the adult cortex. Nature *420*, 812-816.

Hadjieconomou, D., Timofeev, K., and Salecker, I. (2011). A step-by-step guide to visual circuit assembly in Drosophila. Curr Opin Neurobiol *21*, 76-84.

Han, C., Jan, L.Y., and Jan, Y.N. (2011). Enhancer-driven membrane markers for analysis of nonautonomous mechanisms reveal neuron-glia interactions in Drosophila. Proc Natl Acad Sci U S A *108*, 9673-9678.

Hardie, R. (1985). Functional organization of the fly retina. In Progress in sensory physiology (Springer), pp. 1-79.

Hassan, B.A., and Hiesinger, P.R. (2015). Beyond Molecular Codes: Simple Rules to Wire Complex Brains. Cell *163*, 285-291.

Hennig, W. (1973). Diptera (Zweifliigler). Handb Zool, 4 (2) 2/31: 1–337 (Walter de Gruyter, Berlin New York).

Hiesinger, P.R., Zhai, R.G., Zhou, Y., Koh, T.W., Mehta, S.Q., Schulze, K.L., Cao, Y., Verstreken, P., Clandinin, T.R., Fischbach, K.F., *et al.* (2006). Activity-independent prespecification of synaptic partners in the visual map of Drosophila. Curr Biol *16*, 1835-1843.

Holtmaat, A., Bonhoeffer, T., Chow, D.K., Chuckowree, J., De Paola, V., Hofer, S.B., Hubener, M., Keck, T., Knott, G., Lee, W.C., *et al.* (2009). Long-term, high-resolution imaging in the mouse neocortex through a chronic cranial window. Nat Protoc *4*, 1128-1144.

Horridge, G.A., and Meinertzhagen, I.A. (1970). The accuracy of the patterns of connexions of the first- and second-order neurons of the visual system of Calliphora. Proc R Soc Lond B Biol Sci *175*, 69-82.

Huang, Z., and Kunes, S. (1996). Hedgehog, transmitted along retinal axons, triggers neurogenesis in the developing visual centers of the Drosophila brain. Cell *86*, 411-422.

Huang, Z., and Kunes, S. (1998). Signals transmitted along retinal axons in Drosophila: Hedgehog signal reception and the cell circuitry of lamina cartridge assembly. Development *125*, 3753-3764.

Hughes, M.E., Bortnick, R., Tsubouchi, A., Baumer, P., Kondo, M., Uemura, T., and Schmucker, D. (2007). Homophilic Dscam interactions control complex dendrite morphogenesis. Neuron *54*, 417-427.

Imai, T., Yamazaki, T., Kobayakawa, R., Kobayakawa, K., Abe, T., Suzuki, M., and Sakano, H. (2009). Pre-target axon sorting establishes the neural map topography. Science *325*, 585-590.

Kaminker, J.S., Canon, J., Salecker, I., and Banerjee, U. (2002). Control of photoreceptor axon target choice by transcriptional repression of Runt. Nat Neurosci *5*, 746-750.

Kirschfeld, K. (1967). [The projection of the optical environment on the screen of the rhabdomere in the compound eye of the Musca]. Exp Brain Res *3*, 248-270.

Kirschfeld, K., and Franceschini, N. (1968). Optical characteristics of ommatidia in the complex eye of Musca. Kybernetik *5*, 47-52.

Kole, A.J., Annis, R.P., and Deshmukh, M. (2013). Mature neurons: equipped for survival. Cell Death Dis *4*, e689.

Kolodkin, A.L., and Hiesinger, P.R. (2017). Wiring visual systems: common and divergent mechanisms and principles. Curr Opin Neurobiol *42*, 128-135.

Kolodkin, A.L., and Tessier-Lavigne, M. (2011). Mechanisms and molecules of neuronal wiring: a primer. Cold Spring Harb Perspect Biol *3*.

Krishnaswamy, A., Yamagata, M., Duan, X., Hong, Y.K., and Sanes, J.R. (2015). Sidekick 2 directs formation of a retinal circuit that detects differential motion. Nature *524*, 466-470.

Kroll, J.R., Wong, K.G., Siddiqui, F.M., and Tanouye, M.A. (2015). Disruption of Endocytosis with the Dynamin Mutant shibirets1 Suppresses Seizures in Drosophila. Genetics *201*, 1087-1102.

Land, M., and Nilsson, D. (2002). Animal Eyes: Oxford University Press. New York.

Land, M.F. (2005). The optical structures of animal eyes. Curr Biol *15*, R319-323.

Langen, M., Agi, E., Altschuler, D.J., Wu, L.F., Altschuler, S.J., and Hiesinger, P.R. (2015). The Developmental Rules of Neural Superposition in Drosophila. Cell *162*, 120-133.

Langen, M., Koch, M., Yan, J., De Geest, N., Erfurth, M.L., Pfeiffer, B.D., Schmucker, D., Moreau, Y., and Hassan, B.A. (2013). Mutual inhibition among postmitotic neurons regulates robustness of brain wiring in Drosophila. Elife *2*, e00337.

Lee, C.H., Herman, T., Clandinin, T.R., Lee, R., and Zipursky, S.L. (2001). N-cadherin regulates target specificity in the Drosophila visual system. Neuron *30*, 437-450.

Lee, R.C., Clandinin, T.R., Lee, C.H., Chen, P.L., Meinertzhagen, I.A., and Zipursky, S.L. (2003). The protocadherin Flamingo is required for axon target selection in the Drosophila visual system. Nat Neurosci *6*, 557-563.

Lee, T., and Luo, L. (1999). Mosaic analysis with a repressible cell marker for studies of gene function in neuronal morphogenesis. Neuron *22*, 451-461.

Luo, L., Callaway, E.M., and Svoboda, K. (2008). Genetic dissection of neural circuits. Neuron *57*, 634-660.

Martin, K.A., Poeck, B., Roth, H., Ebens, A.J., Ballard, L.C., and Zipursky, S.L. (1995). Mutations disrupting neuronal connectivity in the Drosophila visual system. Neuron *14*, 229-240.

Mason, C., and Erskine, L. (2000). Growth cone form, behavior, and interactions in vivo: retinal axon pathfinding as a model. J Neurobiol *44*, 260-270.

Mast, J.D., Prakash, S., Chen, P.L., and Clandinin, T.R. (2006). The mechanisms and molecules that connect photoreceptor axons to their targets in Drosophila. Semin Cell Dev Biol *17*, 42-49.

Matsuoka, R.L., Nguyen-Ba-Charvet, K.T., Parray, A., Badea, T.C., Chedotal, A., and Kolodkin, A.L. (2011). Transmembrane semaphorin signalling controls laminar stratification in the mammalian retina. Nature *470*, 259-263.

Matthews, B.J., Kim, M.E., Flanagan, J.J., Hattori, D., Clemens, J.C., Zipursky, S.L., and Grueber, W.B. (2007). Dendrite self-avoidance is controlled by Dscam. Cell *129*, 593-604.

Maurel-Zaffran, C., Suzuki, T., Gahmon, G., Treisman, J.E., and Dickson, B.J. (2001). Cell-autonomous and -nonautonomous functions of LAR in R7 photoreceptor axon targeting. Neuron *32*, 225-235.

Meinertzhagen, I., and Hanson, T. (1993). The development of the optic lobe. The development of Drosophila melanogaster *2*, 1363-1491.

Meinertzhagen, I.A. (1972). Erroneous projection of retinula axons beneath a dislocation in the retinal equator of Calliphora. Brain Res *41*, 39-49.

Meinertzhagen, I.A. (1976). The organization of perpendicular fibre pathways in the insect optic lobe. Philos Trans R Soc Lond B Biol Sci *274*, 555-594.

Meinertzhagen, I.A., and Hu, X. (1996). Evidence for site selection during synaptogenesis: the surface distribution of synaptic sites in photoreceptor terminals of the files Musca and Drosophila. Cell Mol Neurobiol *16*, 677-698.

Meinertzhagen, I.A., and O'Neil, S.D. (1991). Synaptic organization of columnar elements in the lamina of the wild type in Drosophila melanogaster. J Comp Neurol *305*, 232-263.

Meinertzhagen, I.A., Piper, S.T., Sun, X.J., and Frohlich, A. (2000). Neurite morphogenesis of identified visual interneurons and its relationship to photoreceptor synaptogenesis in the flies, Musca domestica and Drosophila melanogaster. Eur J Neurosci *12*, 1342-1356.

Meinertzhagen, I.A., and Sorra, K.E. (2001). Synaptic organization in the fly's optic lamina: few cells, many synapses and divergent microcircuits. Prog Brain Res *131*, 53-69.

Meyer, R.L. (1998). Roger Sperry and his chemoaffinity hypothesis. Neuropsychologia *36*, 957-980.

Millard, S.S., Flanagan, J.J., Pappu, K.S., Wu, W., and Zipursky, S.L. (2007). Dscam2 mediates axonal tiling in the Drosophila visual system. Nature *447*, 720-724.

Millard, S.S., Lu, Z., Zipursky, S.L., and Meinertzhagen, I.A. (2010). Drosophila dscam proteins regulate postsynaptic specificity at multiple-contact synapses. Neuron *67*, 761-768.

Miura, S.K., Martins, A., Zhang, K.X., Graveley, B.R., and Zipursky, S.L. (2013). Probabilistic splicing of Dscam1 establishes identity at the level of single neurons. Cell *155*, 1166-1177.

Morante, J., and Desplan, C. (2004). Building a projection map for photoreceptor neurons in the Drosophila optic lobes. Semin Cell Dev Biol *15*, 137-143.

Moses, K. (2006). Evolutionary biology: fly eyes get the whole picture. Nature *443*, 638-639.

Nilsson, D.-E. (1989). Optics and evolution of the compound eye. In Facets of vision (Springer), pp. 30-73.

Ninov, N., Chiarelli, D.A., and Martin-Blanco, E. (2007). Extrinsic and intrinsic mechanisms directing epithelial cell sheet replacement during Drosophila metamorphosis. Development *134*, 367-379.

Ninov, N., and Martin-Blanco, E. (2007). Live imaging of epidermal morphogenesis during the development of the adult abdominal epidermis of Drosophila. Nature protocols *2*, 3074-3080.

Osorio, D. (2007). Spam and the evolution of the fly's eye. Bioessays *29*, 111-115.

Ozel, M.N., Langen, M., Hassan, B.A., and Hiesinger, P.R. (2015). Filopodial dynamics and growth cone stabilization in Drosophila visual circuit development. Elife *4*.

Pecot, M.Y., Chen, Y., Akin, O., Chen, Z., Tsui, C.Y., and Zipursky, S.L. (2014). Sequential axon-derived signals couple target survival and layer specificity in the Drosophila visual system. Neuron *82*, 320-333.

Penn, A.A., and Shatz, C.J. (1999). Brain waves and brain wiring: the role of endogenous and sensory-driven neural activity in development. Pediatr Res *45*, 447-458.

Petrovic, M., and Schmucker, D. (2015). Axonal wiring in neural development: Target-independent mechanisms help to establish precision and complexity. Bioessays *37*, 996-1004.

Picaud, S., Wunderer, H., and Franceschini, N. (1990). Dye-induced photopermeabilization and photodegeneration: a lesion technique useful for neuronal tracing. J Neurosci Methods *33*, 101-112.

Pittet, M.J., and Weissleder, R. (2011). Intravital imaging. Cell *147*, 983-991.

Poeck, B., Fischer, S., Gunning, D., Zipursky, S.L., and Salecker, I. (2001). Glial cells mediate target layer selection of retinal axons in the developing visual system of Drosophila. Neuron *29*, 99-113.

Prakash, S., Caldwell, J.C., Eberl, D.F., and Clandinin, T.R. (2005). Drosophila N-cadherin mediates an attractive interaction between photoreceptor axons and their targets. Nat Neurosci *8*, 443-450.

Prakash, S., McLendon, H.M., Dubreuil, C.I., Ghose, A., Hwa, J., Dennehy, K.A., Tomalty, K.M., Clark, K.L., Van Vactor, D., and Clandinin, T.R. (2009). Complex interactions amongst N-cadherin, DLAR, and Liprin-alpha regulate Drosophila photoreceptor axon targeting. Dev Biol *336*, 10-19.

Rao, Y., Pang, P., Ruan, W., Gunning, D., and Zipursky, S.L. (2000). brakeless is required for photoreceptor growth-cone targeting in Drosophila. Proc Natl Acad Sci U S A *97*, 5966-5971.

Ready, D.F., Hanson, T.E., and Benzer, S. (1976). Development of the Drosophila retina, a neurocrystalline lattice. Dev Biol *53*, 217-240.

Rintelen, F., Stocker, H., Thomas, G., and Hafen, E. (2001). PDK1 regulates growth through Akt and S6K in Drosophila. Proc Natl Acad Sci U S A *98*, 15020-15025.

Rivera-Alba, M., Vitaladevuni, S.N., Mishchenko, Y., Lu, Z., Takemura, S.Y., Scheffer, L., Meinertzhagen, I.A., Chklovskii, D.B., and de Polavieja, G.G. (2011). Wiring economy and volume exclusion determine neuronal placement in the Drosophila brain. Curr Biol *21*, 2000-2005.

Roignant, J.Y., and Treisman, J.E. (2009). Pattern formation in the Drosophila eye disc. Int J Dev Biol *53*, 795-804.

Rybak, J., and Meinertzhagen, I.A. (1997). The effects of light reversals on photoreceptor synaptogenesis in the fly Musca domestica. Eur J Neurosci *9*, 319-333.

Schmucker, D., Clemens, J.C., Shu, H., Worby, C.A., Xiao, J., Muda, M., Dixon, J.E., and Zipursky, S.L. (2000). Drosophila Dscam is an axon guidance receptor exhibiting extraordinary molecular diversity. Cell *101*, 671-684.

Schwabe, T., Borycz, J.A., Meinertzhagen, I.A., and Clandinin, T.R. (2014). Differential adhesion determines the organization of synaptic fascicles in the Drosophila visual system. Curr Biol *24*, 1304-1313.

Schwabe, T., Neuert, H., and Clandinin, T.R. (2013). A network of cadherin-mediated interactions polarizes growth cones to determine targeting specificity. Cell *154*, 351-364.

Seelig, J.D., Chiappe, M.E., Lott, G.K., Dutta, A., Osborne, J.E., Reiser, M.B., and Jayaraman, V. (2010). Two-photon calcium imaging from head-fixed Drosophila during optomotor walking behavior. Nat Methods *7*, 535-540.

Selleck, S.B., Gonzalez, C., Glover, D.M., and White, K. (1992). Regulation of the G1-S transition in postembryonic neuronal precursors by axon ingrowth. Nature *355*, 253-255.

Selleck, S.B., and Steller, H. (1991). The influence of retinal innervation on neurogenesis in the first optic ganglion of Drosophila. Neuron *6*, 83-99.

Senti, K., Keleman, K., Eisenhaber, F., and Dickson, B.J. (2000). brakeless is required for lamina targeting of R1-R6 axons in the Drosophila visual system. Development *127*, 2291-2301.

Senti, K.A., Usui, T., Boucke, K., Greber, U., Uemura, T., and Dickson, B.J. (2003). Flamingo regulates R8 axon-axon and axon-target interactions in the Drosophila visual system. Curr Biol *13*, 828-832.

Shatz, C.J. (1996). Emergence of order in visual system development. Proc Natl Acad Sci U S A *93*, 602-608.

Shaw, S.R. (1969). Optics of arthropod compound eye. Science *165*, 88-90.

Soba, P., Zhu, S., Emoto, K., Younger, S., Yang, S.J., Yu, H.H., Lee, T., Jan, L.Y., and Jan, Y.N. (2007). Drosophila sensory neurons require Dscam for dendritic self-avoidance and proper dendritic field organization. Neuron *54*, 403-416.

Sperry, R.W. (1963). Chemoaffinity in the Orderly Growth of Nerve Fiber Patterns and Connections. Proc Natl Acad Sci U S A *50*, 703-710.

Steller, H., Fischbach, K.F., and Rubin, G.M. (1987). Disconnected: a locus required for neuronal pathway formation in the visual system of Drosophila. Cell *50*, 1139-1153.

Sugie, A., Umetsu, D., Yasugi, T., Fischbach, K.F., and Tabata, T. (2010). Recognition of pre- and postsynaptic neurons via nephrin/NEPH1 homologs is a basis for the formation of the Drosophila retinotopic map. Development *137*, 3303-3313.

Svoboda, K., and Yasuda, R. (2006). Principles of two-photon excitation microscopy and its applications to neuroscience. Neuron *50*, 823-839.

Tayler, T.D., and Garrity, P.A. (2003). Axon targeting in the Drosophila visual system. Curr Opin Neurobiol *13*, 90-95.

Ting, C.Y., and Lee, C.H. (2007). Visual circuit development in Drosophila. Curr Opin Neurobiol *17*, 65-72.

Ting, C.Y., Yonekura, S., Chung, P., Hsu, S.N., Robertson, H.M., Chiba, A., and Lee, C.H. (2005). Drosophila N-cadherin functions in the first stage of the two-stage layer-selection process of R7 photoreceptor afferents. Development *132*, 953-963.

Tomlinson, A., and Ready, D.F. (1987). Neuronal differentiation in Drosophila ommatidium. Dev Biol *120*, 366-376.

Trujillo-Cenóz, O. (1965). Some aspects of the structural organization of the intermediate retina of dipterans. Journal of ultrastructure research *13*, 1-33.

Trujillo-Cenoz, O., and Melamed, J. (1966). Compound eye of dipterans: anatomical basis for integration--an electron microscope study. J Ultrastruct Res *16*, 395-398.

Trujillo-Cenoz, O., and Melamed, J. (1973). The development of the retina-lamina complex in muscoid flies. J Ultrastruct Res *42*, 554-581.

Tsachaki, M., and Sprecher, S.G. (2012). Genetic and developmental mechanisms underlying the formation of the Drosophila compound eye. Dev Dyn *241*, 40-56.

Tuurala, O. (1963). Bau und photomechanische Erscheinungen im Auge einiger Chironomiden (Dipt.). Ann Entomol Fenn *29*, 209-217.

Umetsu, D., Murakami, S., Sato, M., and Tabata, T. (2006). The highly ordered assembly of retinal axons and their synaptic partners is regulated by Hedgehog/Single-minded in the Drosophila visual system. Development *133*, 791-800.

Vigier, P. (1907a). Sur la reception de l'exitant lumineux dans le yeux composes des Insectes, en prticulier chez les Muscides. CR Acad Sci(Paris) *145*, 633-636.

Vigier, P. (1907b). Sur les terminations photoreceptrices dans les yeux composes des Muscides. CR Acad Sci(Paris) *145*, 532-536.

Vigier, P. (1908). Sur l'existence reele et le role des appendices piriformes des neurons. Le neurons perioptique des Dipteres. CR Soc Biol (Paris) *64*, 959-961.

Vigier, P. (1909). Mécanisme de la synthese des impressions lumineuses recueilles par les yeux composés des Dipteres. CR Acad Sci *148*, 1221-1223.

Wardill, T.J., List, O., Li, X., Dongre, S., McCulloch, M., Ting, C.Y., O'Kane, C.J., Tang, S., Lee, C.H., Hardie, R.C., *et al.* (2012). Multiple spectral inputs improve motion discrimination in the Drosophila visual system. Science *336*, 925-931.

Warrant, E.J. (1999). Seeing better at night: life style, eye design and the optimum strategy of spatial and temporal summation. Vision Res *39*, 1611-1630.

Weigert, R., Porat-Shliom, N., and Amornphimoltham, P. (2013). Imaging cell biology in live animals: ready for prime time. The Journal of cell biology *201*, 969-979.

White, K., and Kankel, D.R. (1978). Patterns of cell division and cell movement in the formation of the imaginal nervous system in Drosophila melanogaster. Dev Biol *65*, 296-321.

Williamson, W.R., Yang, T., Terman, J.R., and Hiesinger, P.R. (2010). Guidance receptor degradation is required for neuronal connectivity in the Drosophila nervous system. PLoS Biol *8*, e1000553.

Wing, J.P., Zhou, L., Schwartz, L.M., and Nambu, J.R. (1998). Distinct cell killing properties of the Drosophila reaper, head involution defective, and grim genes. Cell Death Differ *5*, 930-939.

Wojtowicz, W.M., Flanagan, J.J., Millard, S.S., Zipursky, S.L., and Clemens, J.C. (2004). Alternative splicing of Drosophila Dscam generates axon guidance receptors that exhibit isoform-specific homophilic binding. Cell *118*, 619-633.

Wojtowicz, W.M., Wu, W., Andre, I., Qian, B., Baker, D., and Zipursky, S.L. (2007). A vast repertoire of Dscam binding specificities arises from modular interactions of variable Ig domains. Cell *130*, 1134-1145.

Wolff, T., and Ready, D. (1993). Pattern formation in the Drosophila retina. The development of Drosophila melanogaster (Cold Spring Harbor Laboratory Press) *2*, 1277-1325.

Wolff, T., and Ready, D.F. (1991). The beginning of pattern formation in the Drosophila compound eye: the morphogenetic furrow and the second mitotic wave. Development *113*, 841-850.

Yagi, T., and Takeichi, M. (2000). Cadherin superfamily genes: functions, genomic organization, and neurologic diversity. Genes Dev *14*, 1169-1180.

Yamaguchi, S., Wolf, R., Desplan, C., and Heisenberg, M. (2008). Motion vision is independent of color in Drosophila. Proc Natl Acad Sci U S A *105*, 4910-4915.

Yogev, S., and Shen, K. (2014). Cellular and molecular mechanisms of synaptic specificity. Annu Rev Cell Dev Biol *30*, 417-437.

Zipursky, S.L., and Sanes, J.R. (2010). Chemoaffinity revisited: dscams, protocadherins, and neural circuit assembly. Cell *143*, 343-353.